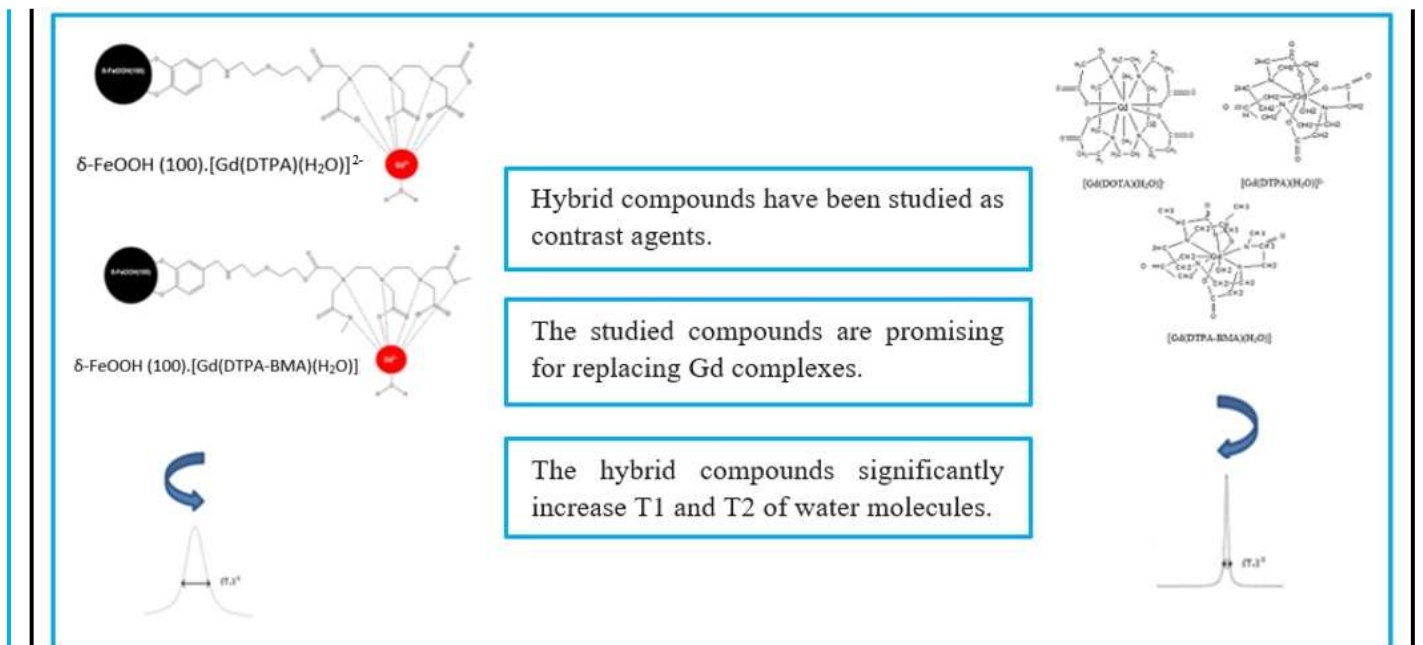


Eclética Química Journal

Volume 45 • number 4 • year 2020



Relaxation parameters of water molecules coordinated with Gd(III) complexes and hybrid materials based on $\delta\text{-FeOOH (100)}$ nanoparticles: A theoretical study of hyperfine interactions for CAs in MRI

Evaluation of the phenyl-bonded silica-based sorbent for pre-concentration of the booster antifouling biocides Zinc Pyrethrin, Zineb and Ziram using solid-phase extraction technique and Inductively Coupled Plasma Mass Spectrometry

Synthesis, characterization, and thermal behavior of amidosulfonates of transition metals in air and nitrogen atmosphere

Approximate solutions of the Schrödinger equation with energy-dependent screened Coulomb potential in D – dimensions

Electrochemical noise analysis to obtain the R_{sn} value via FFT using Excel



UNIVERSIDADE ESTADUAL PAULISTA

Reitor

Sandro Roberto Valentini

Vice-Reitor

Sergio Roberto Nobre

Pró-Reitor de Planejamento Estratégico e Gestão

Leonardo Theodoro Büll

Pró-Reitora de Graduação

Gladis Massini-Cagliari

Pró-Reitora de Pós-Graduação

Telma Teresinha Berchielli

Pró-Reitora de Extensão Universitária

Cleopatra da Silva Planeta

Pró-Reitor de Pesquisa

Carlos Frederico de Oliveira Graeff



INSTITUTO DE QUÍMICA

Diretor

Eduardo Maffud Cilli

Vice-Diretora

Dulce Helena Siqueira Silva

Editorial Team

Editors

- Prof. Assis Vicente Benedetti**, Institute of Chemistry Unesp Araraquara, Brazil (Editor-in-Chief)
Prof. Arnaldo Alves Cardoso, Institute of Chemistry Unesp Araraquara, Brazil
Prof. Antonio Eduardo Mauro, Institute of Chemistry Unesp Araraquara, Brazil
Prof. Horacio Heinzen, Faculty of Chemistry UdelaR, Montevideo, Uruguay
Prof. Maysa Furlan, Institute of Chemistry Unesp Araraquara, Brazil
Prof. Maria Célia Bertolini, Institute of Chemistry Unesp Araraquara, Brazil
Prof. Paulo Clairmont Feitosa de Lima Gomes, Institute of Chemistry, Unesp Araraquara, Brazil

Editorial Board

- Prof. Jairton Dupont**, Instituto de Química, Universidade Federal do Rio Grande do Sul, UFRGS, RS, Brazil
Prof. Enric Brillas, Facultat de Química, Universitat de Barcelona, Spain
Prof. Verónica Cortés de Zea Bermudez, Escola de Ciências da Vida e do Ambiente, Universidade de Trás-os-Montes e Alto Douro, Vila Real, Portugal
Prof. Lauro Kubota, Instituto de Química, Universidade Estadual de Campinas, Unicamp, SP, Brazil
Prof. Ivano Gerardt Rolf Gutz, Instituto de Química, Universidade de São Paulo, USP, SP, Brazil
Prof. Massuo Jorge Kato, Instituto de Química, Universidade de São Paulo, USP, SP, Brazil
Prof. Francisco de Assis Leone, Faculdade de Filosofia, Ciências e Letras, Universidade de São Paulo, Ribeirão Preto, USP-RP, SP, Brazil
Prof. Roberto Santana da Silva, Faculdade de Ciências Farmacêuticas, Universidade de São Paulo, Ribeirão Preto, USP-RP, SP, Brazil
Prof. José Antônio Maia Rodrigues, Faculdade de Ciências, Universidade do Porto, Portugal
Prof. Bayardo Baptista Torres, Instituto de Química, Universidade de São Paulo, USP, SP, Brazil

Technical Staff

Gustavo Marcelino de Souza
Letícia Amanda Miguel

Editorial

The period of uncertainty is not over, but it demonstrates our enormous capacity of adapting to new situations and to overcome obstacles. These includes the intense contribution of authors and reviewers to the Eclética Química Journal, allowing the publication of all issues predicted (thought) to 2020. Opening this issue, two new hybrids paramagnetic compounds δ -FeOOH(100).[Gd(DTPA)(H₂O)]²⁻ and δ -FeOOH (100).[Gd(DTPA-BMA)(H₂O)] are described, which are proposed as contrast agents. It is well known that magnetic resonance imaging is an effective technique for detecting cancer (especially breast cancer), however, for a better visualization of the tissues it is necessary to use the contrast agents, which increase the longitudinal and transverse relaxation times (T₁ and T₂) of water molecules. Subsequently, it is described a robust method of solid-phase extraction using the phenyl-bonded silica-based sorbent (Si-PH sorbent) for pre-concentration of three booster antifouling biocides. Zinc pyrithione, Zineb and Ziram biocides were evaluated in fortified ultrapure water and estuarine water samples for zinc determination. The metals removal procedure revealed efficient, eliminating the possibility of overestimation of the values during the determination of zinc and avoiding the (trans-) metallization of the biocides with other metals present in the Si-PH sorbent. Afterwards, the preparation and characterization of amidosulfonates of different transition metals are described. The analysis of the compounds by X-ray diffraction showed no evidence of isomorphism and their stoichiometry was established from thermal behavior investigation. Stable anhydrous compounds were obtained by dehydration, sulfates constitute intermediates and metallic oxides are formed in the last step of thermal decomposition. Following, an approximate solution of the Schrödinger equation with the energy-dependent screened Coulomb potential in higher dimensions is presented within the framework of the conventional Nikiforov-Uvarov method and a new form of Greene-Aldrich approximation scheme. The major finding of this research is the effect of the energy slope parameter on the energy spectra, which is seen in the existence of two simultaneous energy values for a particular quantum state. A Technical Note developing a methodology to treat electrochemical noise data and to obtain the spectral electrochemical noise resistance closes this issue. A routine was created to obtain the low frequency noise impedance values via Fast Fourier transform using Microsoft Excel and applied to the chalcopyrite dissolution under one specific condition. The results obtained after drift removal showed good agreement with those obtained with Origin[®] software for the same experimental condition.

The Editor and his team are grateful to all the authors for their relevant contributions, and the reviewers for their effort and dedication in evaluating the manuscripts, wishing everyone a better year in 2021. As optimism is a strategy for making a better future, we believe in the successful development of safe vaccines for covid-19 in the coming months.

Assis Vicente Benedetti
Editor-in-Chief of EQJ

Citation databases: Eclética Quim. J. is indexed



*Click on the images to follow the links.

EBSCO has no link available. The address is for subscribers only.

Instructions for Authors Preparation of manuscripts

- **Only manuscripts in English will be accepted.** British or American usage is acceptable, but they should not be mixed.
- **The corresponding author should submit the manuscript online at** <http://revista.iq.unesp.br/ojs/index.php/ecletica/author>
- **Manuscripts must be sent in editable files as *.doc, *.docx or *.odt.** The text must be typed using font style Times New Roman and size 11. Space between lines should be 1.5 mm and paper size A4.
- **Supplementary information:** all the manuscripts accept Supplementary information (SI) that aims at complementing the main text with material that, for any reason, cannot be included in the article.
- **The manuscript should be organized in sections as follows:** Introduction, Experimental, Results and Discussion, Conclusions, and References. Sections titles must be written in bold and sequentially numbered; only the first letter should be in uppercase letter. Subsections should be written in normal and italic lowercase letters. For example: **1. Introduction**; *1.1 History*; **2. Experimental**; *2.1 Surface characterization*; *2.1.1 Morphological analysis*.
- **The cover letter should include:** the authors' full names, e-mail addresses, ORCID code and affiliations, and remarks about the novelty and relevance of the work. The cover letter should also contain a declaration of the corresponding author, on behalf of the other authors, that the article being submitted is original and its content has not been published previously and is not under consideration for publication elsewhere, that no conflict of interest exists and if accepted, the article will not be published elsewhere in the same form, in any language, without the written consent of the publisher. Finally, the cover letter should also contain the suggestion of 3 (three) suitable reviewers (please, provide full name, affiliation, and e-mail).
- **Credit Authors statement*** to be add to the **COVER LETTER**. Information about the individual author contribution to the article (Ex.: Author 1 Conceptualization, Writing – original draft, Methodology, Validation, Writing review and editing; Author 2: Visualization; Author 3: Validation, Writing -review and editing; Author 4: Supervision, Visualization, Writing - review and editing; Author 5: Supervision, Visualization, Writing - review and editing).

*For coming issues.

- **The first page of the manuscript** should contain the title, abstract and keywords. **Please, do not give authors names and affiliation, and acknowledgements since a double-blind review system is used. Acknowledgements should be added to the proof only.**
- **All contributions should include** an Abstract (200 words maximum), three to five Keywords and a Graphical Abstract (8 cm wide × 4 cm high) with an explicative text (2 lines maximum).
- **Citations** should be sequentially numbered and presented in superscript arabica numbers* throughout the text, (“...third generation biofuels products from algae feedstock¹.”), and references should be compiled in square brackets at the end of the manuscript as follows:

*For coming issues.

Journal:

[1] Adorno, A. T. V., Benedetti, A. V., Silva, R. A. G. da, Blanco, M., Influence of the Al content on the phase

transformations in Cu-Al-Ag Alloys, *Eclet. Quim.* 28 (1) (2003) 33-38. <https://doi.org/10.1590/S0100-46702003000100004>.

Book:

[2] Wendlandt, W. W., *Thermal Analysis*, Wiley-Interscience, New York, 3rd ed., 1986, ch1.

Chapter in a book:

[3] Ferreira, A. A. P., Uliana, C. V., Souza Castilho, M. de, Canaverolo Pesquero, N., Foguel, N. V., Pilon dos Santos, G., Fugivara, C. S., Benedetti, A. V., Yamanaka, H., *Amperometric Biosensor for Diagnosis of Disease*, In: *State of the Art in Biosensors - Environmental and Medical Applications*, Rincken, T., ed., InTech: Rijeka, Croatia, 2013, Ch. 12.

Material in process of publication:

[4] Valente Jr., M. A. G., Teixeira, D. A., Lima Azevedo, D., Feliciano, G. T., Benedetti, A. V., Fugivara, C. S., *Caprylate Salts Based on Amines as Volatile Corrosion Inhibitors for Metallic Zinc: Theoretical and Experimental Studies*, *Frontiers in Chemistry*. <https://doi.org/10.3389/fchem.2017.00032>.

- Figures, Schemes, and Tables should be numbered sequentially and presented at the end of the manuscript.
- Nomenclature, abbreviations, and symbols should follow IUPAC recommendations.
- Figures, schemes, and photographs already published by the same or different authors in other publications may be reproduced in manuscripts of **Eclet. Quim. J.** only with permission from the editor house that holds the copyright.
- **Graphical Abstract (GA)** should be a high-resolution figure (900 dpi) summarizing the manuscript in an interesting way to catch the attention of the readers and accompanied by a short explicative text (two lines maximum). GA must be submitted as *.jpg, *.jpeg or *.tif.
- **Communications** should cover relevant scientific results and are limited to 1,500 words or three pages of the Journal, not including the title, authors' names, figures, tables and references. However, Communications suggesting fragmentation of complete contributions are strongly discouraged by Editors.
- **Review articles** should be original and present state-of-the-art overviews in a coherent and concise form covering the most relevant aspects of the topic that is being revised and indicate the likely future directions of the field. Therefore, before beginning the preparation of a Review manuscript, send a letter (one page maximum) to the Editor with the subject of interest and the main topics that would be covered in the Review manuscript. The Editor will communicate his decision in two weeks. Receiving this type of manuscript does not imply acceptance to be published in **Eclet. Quím. J.** It will be peer-reviewed.
- **Short reviews** should present an overview of the state-of-the-art in a specific topic within the scope of the Journal and limited to 5,000 words. Consider a table or image as corresponding to 100 words. Before beginning the preparation of a Short Review manuscript, send a letter (one page maximum) to the Editor with the subject of interest and the main topics that would be covered in the Short Review manuscript.
- **Technical Notes:** descriptions of methods, techniques, equipment or accessories developed in the authors' laboratory, as long as they present chemical content of interest. They should follow the usual form of presentation, according to the peculiarities of each work. They should have a maximum of 25 pages, including figures, tables, diagrams, etc.
- **Articles in Education in Chemistry and chemistry-correlated areas:** research manuscript related to undergraduate teaching in Chemistry and innovative experiences in undergraduate and graduate education. They should have a maximum of 25 pages, including figures, tables, diagrams, and other elements.
- **Special issues** with complete articles dedicated to Symposia and Congresses **and to special themes or in honor of scientists with relevant contributions in Chemistry and correlate areas*** can be published by

Eclét. Quím. J. under the condition that a previous agreement with Editors is established. All the guides of the journal must be followed by the authors.

♦For coming issues.

Supplementary information: the text is constituted of the first page of the main manuscript (removed the **Abstract** and **Keywords**) and information not included in the main text but able to complement experimental data or favors the comprehension of the manuscript such as: other experimental data not added to the main text, figures, tables, deduction of equations, texts specifying parts of the article, files with raw data, videos, etc.

Supplementary information should be referred in the main text using sequential numbering preceded of S to tables and figures numbers, that will find in the Supplementary information (*SI*). Videos and raw data file will be indicated with the name of the file.

Examples: Indication in the main text: (**Fig. S1, SI**); (**Table S1, SI**), (**Video: self-healing, SI**); (**Raw data: electrochemical noise data.xls, SI**).

Supplementary information will be located following the article with a different DOI number from that of the article, but easily related to it. **SI** material should be submitted as supplementary files (It can be uploaded the necessary number of files).

At the end of the main text the authors should inform: This article has **Supplementary information** (tables, figures, text, deduction of equations, videos, raw data, etc.).

Eclét. Quím. J. Ethical Guides and Publication Copyright:

Before beginning the submission process, please be sure that all ethical aspects mentioned below were followed. Violation of these ethical aspects may prevent authors from submitting and/or publishing articles in **Eclét. Quím. J.**

- The corresponding author is responsible for listing as coauthors only researchers who have really taken part in the work, for informing them about the entire manuscript content and for obtaining their permission to submit and publish it.
- Authors are responsible for carefully searching for all the scientific work relevant to their reasoning irrespective of whether they agree or not with the presented information.
- Authors are responsible for correctly citing and crediting all data used from works of researchers other than the ones who are authors of the manuscript that is being submitted to **Eclét. Quím. J.**
- Citations of Master's Degree Dissertations and PhD Theses are not accepted; instead, the publications resulting from them must be cited.
- Explicit permission of a nonauthor who has collaborated with personal communication or discussion to the manuscript being submitted to **Eclét. Quím. J.** must be obtained before being cited.
- Simultaneous submission of the same manuscript to more than one journal is considered an ethical deviation and is conflicted to the declaration has been done below by the authors.
- Plagiarism, self-plagiarism, and the suggestion of novelty when the material was already published are unaccepted by **Eclét. Quím. J.**
- The word-for-word reproduction of data or sentences as long as placed between quotation marks and correctly cited is not considered ethical deviation when indispensable for the discussion of a specific set of data or a hypothesis.
- Before reviewing a manuscript, the *Turnitin* antiplagiarism software will be used to detect any ethical deviation.

- The corresponding author transfers the copyright of the submitted manuscript and all its versions to **Eclét. Quim. J.**, after having the consent of all authors, which ceases if the manuscript is rejected or withdrawn during the review process.
- Before submitting manuscripts involving human beings, materials from human or animals, the authors need to confirm that the procedures established, respectively, by the institutional committee on human experimentation and Helsinki's declaration, and the recommendations of the animal care institutional committee were followed. Editors may request complementary information on ethical aspects.
- When a published manuscript in EQJ is also published in other Journal, it will be immediately withdrawn from EQJ and the authors informed of the Editor decision.
- **Manuscript Submissions**

For the first evaluation: the manuscripts should be submitted in three files: the cover letter as mentioned above, the graphical abstract and the entire manuscript.

The entire manuscript should be submitted as *.doc, *.docx or *.odt files.

The Graphical Abstract (GA) 900 dpi resolution is mandatory for this Journal and should be submitted as *.jpg, *.jpeg or *.tif files as supplementary file.

The cover letter should contain the title of the manuscript, the authors' names and affiliations, and the relevant aspects of the manuscript (no more than 5 lines), and the suggestion of 3 (three) names of experts in the subject: complete name, affiliation, and e-mail).

When appropriate, important data to complement and a better comprehension of the article can be submitted as Supplementary File, which will be published online and will be made available as links in the original article. This might include additional figures, tables, text, equations, videos or other materials that are necessary to fully document the research contained in the paper or to facilitate the readers' ability to understand the work. Supplementary Materials should be presented in appropriate .docx file for text, tables, figures and graphics. The full title of the paper, authors' names and affiliations, and corresponding author should be included in the header. All supplementary figures, tables and videos should be referred in the manuscript body as "Table S1, S2...", "Fig. S1, S2..." and "Video S1, S2 ...".

- **Reviewing**

The time elapsed between the submission and the first response of the reviewers is around 3 months. The average time elapsed between submission and publication is seven months.

- **Resubmission** (manuscripts "rejected in the present form" or subjected to "revision"): **A LETTER WITH THE RESPONSES TO THE COMMENTS/CRITICISM AND SUGGESTIONS OF REVIEWERS/EDITORS SHOULD ACCOMPANY THE REVISED MANUSCRIPT. ALL MODIFICATIONS MADE TO THE ORIGINAL MANUSCRIPT MUST BE HIGHLIGHTED.**

- **Editor's requirements**

Authors who have a manuscript accepted in **Eclética Química Journal** may be invited to act as reviewers.

Only the authors are responsible for the correctness of all information, data and content of the manuscript submitted to **Eclética Química Journal**. Thus, the Editors and the Editorial Board cannot accept responsibility for the correctness of the material published in **Eclética Química Journal**.

- **Proofs**

After accepting the manuscript, **Eclét. Quim. J.** technical assistants will contact you regarding your manuscript

page proofs to correct printing errors only, i.e., other corrections or content improvement are not permitted. The proofs shall be returned in 3 working days (72 h) via e-mail.

- **Authors Declaration**

The corresponding author declares, on behalf of the other authors, that the article being submitted is original and has been written by the stated authors who are all aware of its content and approve its submission. Declaration should also state that the article has not been published previously and is not under consideration for publication elsewhere, that no conflict of interest exists and if accepted, the article will not be published elsewhere in the same form, in any language, without the written consent of the publisher.

- **Appeal**

Authors may only appeal once about the decision regarding a manuscript. To appeal against the Editorial decision on your manuscript, the corresponding author can send a rebuttal letter to the editor, including a detailed response to any comments made by the reviewers/editor. The editor will consider the rebuttal letter, and if deemed appropriate, the manuscript will be sent to a new reviewer. The Editor decision is final.

- **Contact**

Letícia Amanda Miguel
(eletica@journal.iq.unesp.br)

Submission Preparation Checklist

As part of the submission process, authors are required to check off their submission's compliance with all of the following items, and submissions may be returned to authors that do not adhere to these guidelines.

- In **Step 1**, select the appropriate section for this submission.
- Be sure that Authors' names, affiliations and acknowledgements were removed from the manuscript. The manuscript must be in *.doc, *.docx or *.odt format before uploading in **Step 2**.
- In **Step 3**, add the full name of each author including the ORCID IDs in its full URL ONLY WITH HTTP, NOT HTTPS (ex. <http://orcid.org/0000-0002-1825-0097>).
- Add the authors in the same order as they appear in the manuscript in **step 3**.
- Be sure to have the COVER LETTER and GRAPHICAL ABSTRACT (according to the Author Guidelines) to upload them in **Step 4**.
- Check if you've followed all the previous steps before continuing the submission of your manuscript.

Copyright Notice

The corresponding author transfers the copyright of the submitted manuscript and all its versions to **Eclet. Quim. J.**, after having the consent of all authors, which ceases if the manuscript is rejected or withdrawn during the review process.

Self-archive to institutional, thematic repositories or personal web page is permitted just after publication. The articles published by **Ecletica Química Journal** are licensed under the Creative Commons Attribution 4.0 International License.

SUMMARY

EDITORIAL BOARD.....	3
EDITORIAL.....	4
DATABASE.....	5
INSTRUCTIONS FOR AUTHORS	6

ORIGINAL ARTICLES

Relaxation parameters of water molecules coordinated with Gd(III) complexes and hybrid materials based on δ -FeOOH (100) nanoparticles: A theoretical study of hyperfine interactions for CAs in MRI 12
Mateus Aquino Gonçalves, Teodorico Castro Ramalho

Evaluation of the phenyl-bonded silica-based sorbent for pre-concentration of the booster antifouling biocides Zinc Pyrethrin, Zineb and Ziram using solid-phase extraction technique and Inductively Coupled Plasma Mass Spectrometry 21
Ana Marta Cavinato Marchini Rolisola, Amauri Antônio Menegário, Lauren Nozomi Marques Yabuki, Luciana Polese, Chang Hung Kiang

Synthesis, characterization, and thermal behavior of amidosulfonates of transition metals in air and nitrogen atmosphere 32
Jose Marques Luiz, Ronaldo Spezia Nunes

Approximate solutions of the Schrödinger equation with energy-dependent screened Coulomb potential in D - dimensions 40
Uduakobong Sunday Okorie, Akpan Ndem Ikot, Precious Ogbonda Amadi, Alalibo Thompson Ngiangia, Etebong E. Ibekwe

TECHNICAL NOTE

Electrochemical noise analysis to obtain the R_{sn} value via FFT using Excel 57
Sidineia Barrozo, Riberto Nunes Peres, Marcus José Witzler, Assis Vicente Benedetti, Cecílio Sadao Fugivara

Relaxation parameters of water molecules coordinated with Gd(III) complexes and hybrid materials based on δ -FeOOH (100) nanoparticles: A theoretical study of hyperfine interactions for CAs in MRI

Mateus Aquino Gonçalves¹⁺, Teodorico Castro Ramalho¹

1. Department of Chemistry, Federal University of Lavras, Lavras, Minas Gerais, Brazil

*Corresponding author: Mateus Aquino Gonçalves, Phone: +55 35 992310551, Email address: mateusufla@gmail.com

ARTICLE INFO

Article history:

Received: November 29, 2019

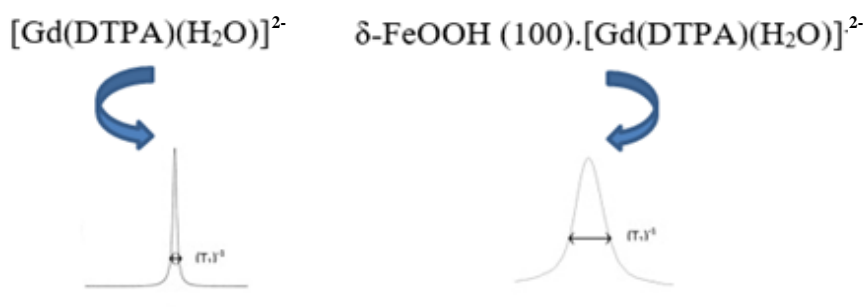
Accepted: March 23, 2020

Published: October 01, 2020

Keywords:

1. gadolinium
2. dynamics
3. interactions hyperfine
4. contrast agents
5. MRI

ABSTRACT: Cancer is a serious disease that afflicts and worries much of the population, which significantly affects all ages and socio-economic groups and one reason is the great difficulty of the initial diagnostic phase. Thus, magnetic resonance imaging (MRI) is an effective technique for detecting cancer (especially breast cancer), however, for a better visualization of the tissues it is necessary to use the Contrast Agents (CAs), which are paramagnetic compounds capable of increasing the longitudinal and transverse relaxation times (T_1 and T_2) of water molecules. The CAs are important to increase the rate of relaxation of water protons, the most commonly used CAs are Gd^{3+} complexes. Thus, in this work we propose two new hybridizing contrast agent, δ -FeOOH(100). $[Gd(DTPA)(H_2O)]^{2-}$ and δ -FeOOH (100). $[Gd(DTPA-BMA)(H_2O)]$, both compounds are capable of increasing both relaxation times T_1 and T_2 . Theoretical results show that the hybrid compound considerably increases the hyperfine coupling constants 1H and ^{17}O of water molecules. In this way, our results show that both hybrid compounds can be used as new contrast agents, thus replacing Gd^{3+} complexes.



1. Introduction

The Magnetic Resonance Imaging (MRI) is considered to be an effective technique for diagnosing lesions and cancer. Currently, this technique is widely used in radiology to obtain detailed tissue images^{1,2}. Currently, there are many techniques used in the diagnosis of cancer. Among the most used diagnostic techniques for cancer, we can highlight Tomography, Ultrasonic Endoscopy, and Magnetic Resonance Imaging (RMI). RMI is one of the most successful techniques, it is a noninvasive technique based on the magnetic properties of 1H and ^{17}O atoms, which are the most

abundant elements in the human body. However, only with the natural relaxation (T_1 and T_2) of these atoms it is not possible to obtain clear images of the tissues, so the Contrast Agents (CAs) are used³. CAs are paramagnetic compounds and their use is of utmost importance for a better visualization of the images in the MRI exams. Currently, the most commonly used CAs are Gd^{3+} complexes with different ligands, such as DOTA, DTPA, EDTA, etc.

The most commonly used CAs are Gd^{3+} complexes, gadolinium is an internal transition metal belonging to the lanthanide family. Since the initial reports Gd has become the most used metal center for the production of CAs. The seven unpaired

electrons of Gd combined with a relatively long relaxation time, makes this lanthanide an effective CAs. Gd has been used as CA since the late 1980s, these CAs alter both T_1 and T_2 relaxation times, however studies show that they are more effective in T_1 ³⁻⁵. The Gd^{3+} complexes with poly (aminocarboxylate) ligands are the contrast agents most commonly used commercially, these compounds have nitrogen and oxygen atoms that are able to coordinate with the Gd^{3+} ion. It is worth stressing that Gd complexes increase both relaxation rates ($r_1=1/T_1$ and $r_2=1/T_2$), however, a higher longitudinal relaxation rate is observed^{6,7}. In contrast, iron oxides have properties that significantly shorten the T_2 and T_2^* values of tissue water molecules, this characteristic is due to the difference in susceptibility between the iron oxide nucleus and the surroundings water^{8,9}. Thus, the two compounds together can have very important properties, especially in the reduction of both

relaxation times and these materials are known as hybrid compounds and have been widely studied¹⁰. Studies show that such hybrid compounds applied in MRI have been shown to be about 8 times larger in imaging effects than Magnevist (widely used CAs)¹¹. With that in mind, the purpose of this paper is to investigate the water molecules coordinated with the complexes $([Gd(DOTA)(H_2O)]^-)$, $[Gd(DTPA)(H_2O)]^{2-}$, $[Gd(DTPA-BMA)(H_2O)]$ and the hybrids $\delta\text{-FeOOH}(100).[Gd(DTPA)(H_2O)]^{2-}$ and $\delta\text{-FeOOH}(100).[Gd(DTPA-BMA)(H_2O)]$, where DOTA = 1,4,7,10-Tetraazacyclododecane-1,4,7,10-tetraacetic acid; DTPA= 2-[Bis[2-[bis(carboxymethyl)amino]ethyl]amino]acetic acid and BMA = bis-methylamide, in order to assess the hyperfine interactions of the 1H and ^{17}O , studying its applicability as potential contrast agents for tracking of cancer cells. Fig. 1 show the hybrid compounds used in this work.

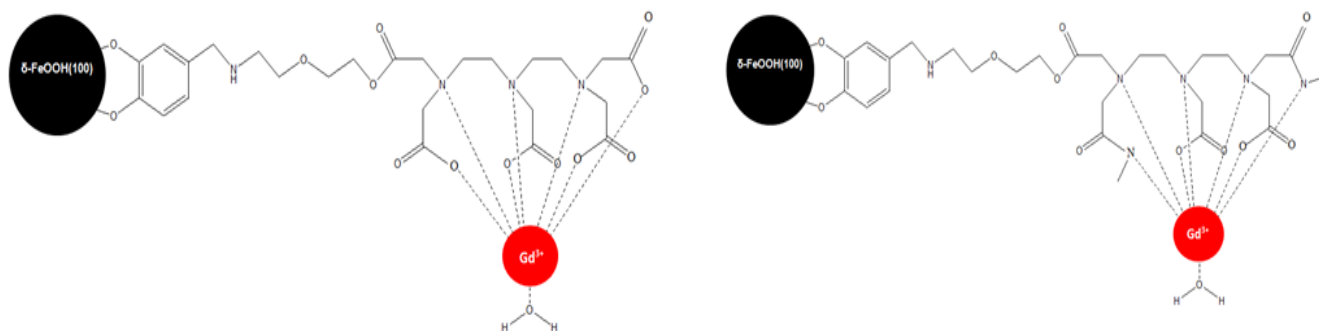


Figure 1. Structure of the hybrid a) $\delta\text{-FeOOH}(100).[Gd(DTPA)(H_2O)]^{2-}$ and b) $\delta\text{-FeOOH}(100).[Gd(DTPA-BMA)(H_2O)]$.

2. Computational methods

2.1 Optimization of structures and Molecular Dynamics Simulations calculations

Initially optimize the complexes $([Gd(DOTA)(H_2O)]^-)$, $[Gd(DTPA)(H_2O)]^{2-}$ and $[Gd(DTPA-BMA)(H_2O)]$ ^{12,13} and the hybrids $\delta\text{-FeOOH}(100).[Gd(DTPA)(H_2O)]^{2-}$ and $\delta\text{-FeOOH}(100).[Gd(DTPA-BMA)(H_2O)]$, in the gaussian 09 program¹⁴, using the semi-empirical Parameterization Method 6 (PM6)^{15,16}.

After optimization, we made the molecular dynamics simulations (MD) for the complexes of Gd(III) using the program developed by van Duin and col. (REAX-FF)¹⁷, which is part of ADF-BAND program package. For the simulations was used the force field NiCH. For the MD simulation

the box size was fixed at 8000 \AA^3 and was held at a temperature 310.65 K (physiologic temperature) throughout the simulation. Studies have shown that this temperature is adequate to simulate this type of model. For these simulations a 500 ps thermalization face (for system stabilization) and an additional 2.0 ns period are required, the box was built by the density of liquid water ($\rho=0.996 \text{ g cm}^{-3}$)¹⁸.

2.2 Statistical inefficiency, surface, and hyperfine coupling constant (HFCC) Calculations

After the MD simulation it is necessary to try to reduce the number of conformations for the later quantum calculations (decrease the computational cost). For this, we selected the uncorrelated configurations of the Gd(III) complexes, Scilab

2.7¹⁹ program was used. The method was developed and applied for the first time by the Canuto's group²⁰. This method uses the statistical interval obtained from the energy autocorrelation, the interval between uncorrelated configurations, or the correlation step s , is calculated by integration from zero to infinity of $C(n)$, Eq. 1. The interval between uncorrelated configurations, or the correlation step τ (the molecular rotational correlation time in Eq. 2) is calculated by integration from zero to infinity of $C(n)$. The theory shows that separate the settings by 2τ , or larger intervals, are considered uncorrelated.

$$C(n) = \sum_{i=1}^N C_i e^{-n/\tau_i} \quad (1)$$

$$\tau = \int_0^{\infty} C(t) dt \quad (2)$$

With uncorrelated structures we did the constant calculations of hyperfine coupling (A_{iso}) for the complexes with water molecules.

The hyperfine coupling constant (A_{iso}) calculations were carried out in the program Gaussian 09, with uncorrelated structures from MD simulation of Gd^{3+} complexes and with the lowest energy structure of the hybrid. For the Gd^{3+} complexes, the simulation was performed using the functional PBE1PBE²¹ and basis set EPR-III for the H and O atoms, 6-31G for the C and N atoms, MWB53 for the Gd atom. For the hybrid compounds was also used the above-mentioned base function and we added the lan12dz for the Fe atom.

3. Results

3.1 Method validation

The geometry of the complex was fully optimized using the method PM6, the geometry according mounted as shown in Fig. 2 and the bond distances from the metal coordination environment are listed in Tab. 1⁷.

From the results of Tab. 1, it is possible to observe that our calculations were able to reproduce reasonably well the distances between the Gd^{III} and the ligand, observed with the experimental results performed by x-ray.

We observed for the complex that $[\text{Gd}(\text{DOTA})(\text{H}_2\text{O})]$, the inner sphere water molecule has a bond distance around 2.45 Å, what satisfies our theoretical value 2.56 Å. For the complexes $[\text{Gd}(\text{DPTA})(\text{H}_2\text{O})]^-$ and $[\text{Gd}(\text{DTPA-BMA})(\text{H}_2\text{O})]$ water molecules in the inner sphere have a connection distance between 2.49 Å, and 2.44 Å, which satisfies the theoretical values 2.52 Å and 2.46 Å, respectively. This can be attributed, at least in part, to the fact that the implicit solvation model (which uses the dielectric constant of the medium) cannot explain some specific interactions between the complex and the solvent, for example, the hydrogen bonds. Indeed, it has been shown that continuous dielectric solvent models are often inadequate to investigate solutes that concentrate on the charge density with strong local solute-solvent interactions⁷. Thus, to try to overcome this deficiency, we performed calculations of geometry optimization using only one coordinated water molecule with Gd. Table 1 shows the distances of the complex bonds compared with the experimental values.

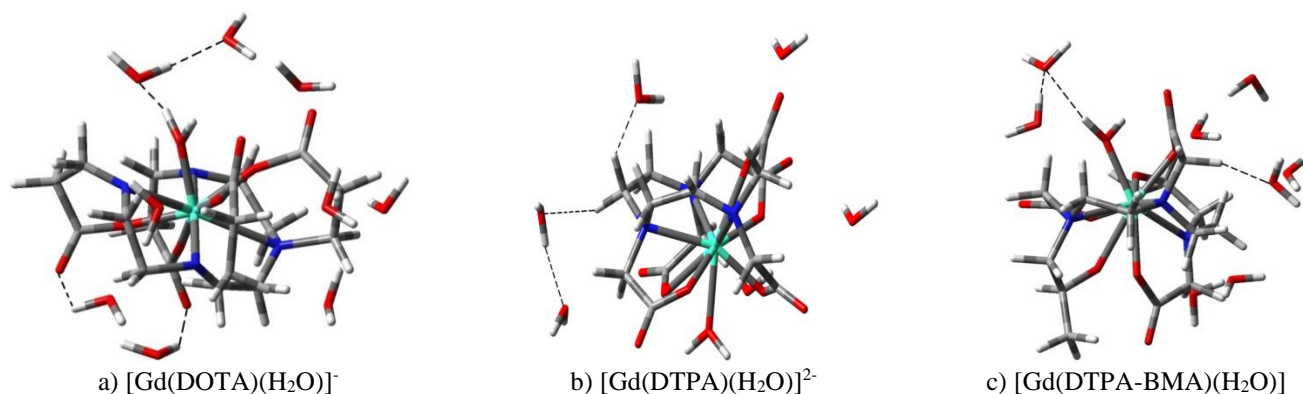


Figure 2. Structure of Gd(III) complexes.

Table 1. Distance values of experimental and theoretical bond for the complex.

Bonds	[Gd(DOTA)(H ₂ O)] ⁻¹²		[Gd(DTPA)(H ₂ O)] ²⁻¹⁵		[Gd(DTPA-BMA)(H ₂ O)] ¹⁶	
	Distances / Å	Exp. / Å	Distances / Å	Exp. / Å	Distances / Å	Exp. / Å
Gd-O _w	2.56	2.45	2.52	2.49	2.46	2.44
Gd-N	2.68	2.65	2.51	2.64	2.50	2.67
Gd-O _c ¹	2.10	2.36	2.45	2.40	2.30	2.37
Gd-O _A ²	-	-	-	-	2.35	2.44

¹Coordinated oxygen atoms of acetate groups.

²Oxygen atoms of amide groups.

3.2 Time correlation

MD calculations provide thousands of conformations, so it is possible to perform quantum calculations of all these conformations. Thus, methods to select the main structures of MD have been studied. Currently, one method that has been highly effective is statistical inefficiency¹⁸⁻²¹. With this in mind, in the present work we use statistically different structures for quantum mechanics calculations, the method uses the energy correlation function of MD simulations^{22,23}. It is important to mention that this method was developed and studied deeply by the Coutinho and Canuto group²³. The Canuto and Coutinho group showed that the statistical interval, $C(n)$, is particularly important for a Markovian process, where $C(n)$ follows an exponential deterioration²². In this way, uncorrelated configurations, τ , is calculated by integrating zero to infinity of $C(n)$.

Configurations separated by 2τ , or larger intervals, are considered uncorrelated²³⁻²⁵. Figure 3 shows exponential decay.

From the simulation MD, as can be seen in Fig. 3, the correlation time of the complex coordinated with water molecules ([Gd(DOTA)(H₂O)]⁻, [Gd(DTPA)(H₂O)]²⁻ and [Gd(DTPA-BMA)(H₂O)] were 4.09, 6.01 and 6.53 ps, respectively. According to the calculations of statistical inefficiency for the complex [Gd(DOTA)(H₂O)]⁻ 244 structures were uncorrelated, for the [Gd(DTPA)(H₂O)]²⁻ 164 structures were uncorrelated and for the complex [Gd(DTPA-BMA)(H₂O)] 153 structures were uncorrelated. We observed that the complex [Gd(DTPA-BMA)(H₂O)] has a larger correlation time relative to other complexes, thus has a smaller number of uncorrelated structures.

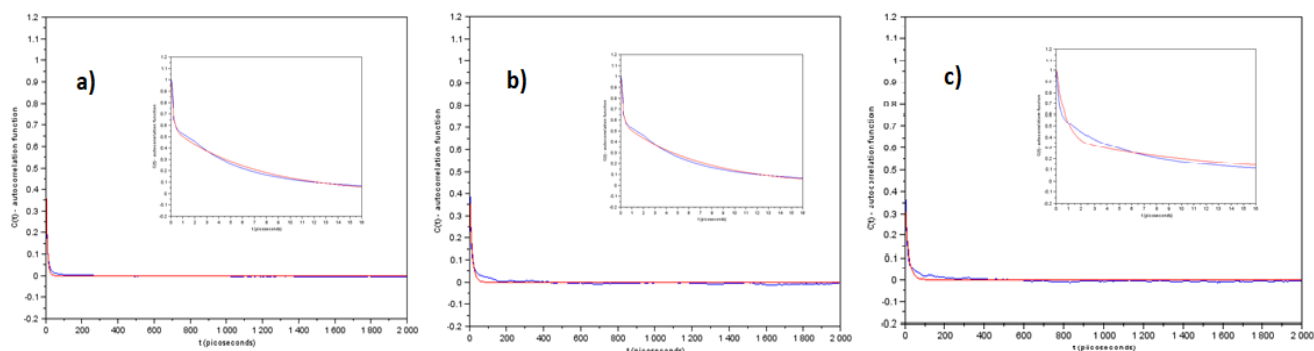


Figure 3. Graphic of the auto-correlation function for the time in picoseconds. a) ([Gd(DOTA)(H₂O)]⁻), b) [Gd(DTPA)(H₂O)]²⁻, c) [Gd(DTPA-BMA)(H₂O)]. The blue curve is the correction and the red curve the adjustment done.

3.3 Electronic and Geometric Effects on the Hyperfine Coupling Constant

In recent decades, the MRI has emerged as a powerful diagnostic tool that uses longitudinal relaxation times (T_1) and transverse (T_2) of the atoms ¹H and ¹⁷O of water molecules to obtain

tissue images. The value T_1 is related to the return time magnetization to the longitudinal axis and it is influenced by the interaction of spins with the network (environment). The value of T_2 refers to the reduction of magnetization in the transverse plane and it is influenced by the spin-spin (dipole-dipole) interaction. The dipolar magnetic

interactions between protons of water with other local interactions, are able to gradually restore the original orientation of the magnetization vector along the main magnetic field²⁶, that way, to

$$R_1 = \frac{1}{T_1} \cong \frac{1}{15} \frac{S(S+1)g_e^2\beta^2g_N^2\beta_N^2}{\hbar^2r^6} + \left(\frac{A}{\hbar}\right)^2 \frac{S(S+1)}{3} \left[\frac{2\tau_e}{1+(\omega_I\tau_e)^2} \right] \quad (3)$$

$$R_2 = \frac{1}{T_2} \cong \frac{1}{15} \frac{S(S+1)g_e^2\beta^2g_N^2\beta_N^2}{\hbar^2r^6} + \left(\frac{A}{\hbar}\right)^2 \frac{S(S+1)}{3} \left[\tau_C + \frac{\tau_C}{1+(\omega_S\tau_e)^2} \right] \quad (4)$$

Observing Eqs. 1 and 2, we have that the longitudinal relaxation time (T_1) depends on several parameters, such as: the electron spin (S), the electronic (g_e) and proton g factors (g_N), the Bohr magneton (β), the nuclear magneton (β_N), the hyperfine coupling constant (A), the ion-nucleus distance (r), and the Larmor frequencies for the proton (ω_I) and electron spins (ω_S), τ_e is the correlation time that characterizes the time of internal rotational correlation of molecules. In the Eq. 2, besides the constants already mentioned we also have τ_C , which is the correlation time characterized by the rate of change of the ion interactions between metal and neighboring hydrogens. In these equations it is important to highlight the hyperfine coupling constant, which is the most sensitive parameter and what our calculations were performed²¹.

We evaluate the constant values of hyperfine coupling to ^1H e ^{17}O , and was chosen the A_{iso} parameters to evaluate the effects of structures, because the A_{iso} values are more sensitive to geometric parameters of structures, thereby facilitating the observation of a variation of the

evaluate the influence of contrast agents on T_1 and T_2 times it is necessary that the compound be paramagnetic. Thus, the Eqs. 3 and 4 represent the relaxation time T_1 and T_2 , respectively.

parameters²⁷. Initially we will start to analyze the A_{iso} coupling constant of the complex $[\text{Gd}(\text{DOTA})(\text{H}_2\text{O})]^-$ water molecules coordinated with. According to Tab. 2, we note that for the structure in equilibrium $A_{\text{iso}}^{\text{eq}}(\text{PBE1PBE}(\text{H}_2\text{O})//\text{PBE1PBE}(\text{H}_2\text{O}))$ obtained A_{iso} values equal to 0.53 MHz for the ^1H and 0.87 MHz for the ^{17}O . It was also made calculations with the implicit solvent and explicit $A_{\text{iso}}^{\text{eq}}(\text{PBE1PBE}(\text{H}_2\text{O})/\text{PCM}/\text{PBE1PBE}(\text{H}_2\text{O}))$. The values were 0.33 MHz and 0.82 MHz for the ^1H and ^{17}O , respectively, the result indicate that the implicit solvent does not influence significantly our system and it shows that the amount of water molecules are allowed sufficient to realistically simulate our system. Thus, analyzing the calculations now uncorrelated with the values of MD $A_{\text{iso}}^{300\text{K}}(\text{MD}(\text{H}_2\text{O})//\text{MD}(\text{H}_2\text{O}))$ we have 0.92 MHz for the ^1H and 0.72 MHz for the ^{17}O . By analyzing these results, it is observed that the thermal effects influence the system, making the A_{iso} values closer to the experimental. This increase in A_{iso} values is to be expected since thermal effects are important in the system.

Table 2. Values of A_{iso} of the Water in the presence of $[\text{Gd}(\text{DOTA})(\text{H}_2\text{O})]^-$.

Water in the presence of $[\text{Gd}(\text{DOTA})(\text{H}_2\text{O})]^-$	A_{iso}	
	$^1\text{H}(\text{MHz})$	$^{17}\text{O}(\text{MHz})$
$A_{\text{iso}}^{\text{eq}}(\text{PBE1PBE}(\text{H}_2\text{O})//\text{PBE1PBE}(\text{H}_2\text{O}))^{\text{a}}$	0.53	0.87
$A_{\text{iso}}^{\text{eq}}(\text{PBE1PBE}(\text{H}_2\text{O})/\text{PCM}/\text{PBE1PBE}(\text{H}_2\text{O}))$	0.33	0.82
$A_{\text{iso}}^{300\text{K}}(\text{MD}(\text{H}_2\text{O})//\text{MD}(\text{H}_2\text{O}))$	0.92	0.72
Experimental	-	0.59

Analysing now the complex $[\text{Gd}(\text{DTPA})(\text{H}_2\text{O})]^{2-}$, in Tab. 3, the A_{iso} values of equilibrium structure, $A_{\text{iso}}^{\text{eq}}$ (PBE1PBE(H_2O)/PBE1PBE(H_2O)), was of 0.38 MHz for the ^1H and 0.85 MHz for the ^{17}O . The calculations with the implicit solvent and explicit $A_{\text{iso}}^{\text{eq}}$ (PBE1PBE (H_2O)/PCM// PBE1PBE (H_2O)), the values obtained were of 0.47 MHz for the ^1H and 0.80 MHz for the ^{17}O , it was observed that the values of the explicit and implicit solvent next are the values only with explicit solvent, in other

words, the water molecules placed as solvent were able to realistically represent our system. The calculations with uncorrelated structures of the MD, $A_{\text{iso}}^{300\text{K}}$ (MD(H_2O)/MD(H_2O)), we have the values of 0.65 MHz for the ^1H and 0.75 for the ^{17}O . Thus, the thermal effects were also shown to be important. In fact, the molecular dynamics calculations are important to simulate a more real system, thus, it is expected that the results are closer to the experimental ones.

Table 3. Values of A_{iso} of the Water in the presence of $[\text{Gd}(\text{DTPA})(\text{H}_2\text{O})]^{2-}$.

Water in the presence of $[\text{Gd}(\text{DTPA})(\text{H}_2\text{O})]^{2-}$		
	A_{iso}	
	^1H / MHz	^{17}O / MHz
$A_{\text{iso}}^{\text{eq}}$ (PBE1PBE(H_2O)/PBE1PBE(H_2O))	0.38	0.85
$A_{\text{iso}}^{\text{eq}}$ (PBE1PBE (H_2O)/PCM// PBE1PBE (H_2O))	0.47	0.80
$A_{\text{iso}}^{300\text{K}}$ (MD(H_2O)/MD(H_2O))	0.65	0.75
Experimental	-	0.61

Analyzing the last complex of work (Tab. 4), $[\text{Gd}(\text{DTPA-BMA})(\text{H}_2\text{O})]$, the equilibrium structure, $A_{\text{iso}}^{\text{eq}}$ (PBE1PBE(H_2O)/PBE1PBE(H_2O)), the values obtained were 0.33 MHz for the ^1H and 0.89 MHz for the ^{17}O , and calculations with the implicit solvent and explicit $A_{\text{iso}}^{\text{eq}}$ (PBE1PBE (H_2O)/PCM// PBE1PBE (H_2O)), the values obtained were of 0.55 MHz for the ^1H and 0.75 MHz for the ^{17}O . Calculations with uncorrelated structures of the MD, $A_{\text{iso}}^{300\text{K}}$ (MD(H_2O)/MD(H_2O)), the values obtained were 0.95 MHz for the ^1H and 0.72 MHz for the ^{17}O . The thermal effects were important, the A_{iso} values were closer to the experimental. In

Fig. 2 are shown the structures of Gd(III) complexes with different ligands.

As noted, in both cases ($[\text{Gd}(\text{DOTA})(\text{H}_2\text{O})]^-$ and $[\text{Gd}(\text{DTPA})(\text{H}_2\text{O})]^{2-}$) in both cases ($[\text{Gd}(\text{DOTA})(\text{H}_2\text{O})]^-$ and $[\text{Gd}(\text{DTPA})(\text{H}_2\text{O})]^{2-}$) the thermal effects were important. With the incessant movement of water molecules, more interactions can occur between the solvent and the solute and between solvent molecules (such as hydrogen bonds). These interactions are the main responsible for the considerable increase in A_{iso} values. The fact, thermal effects are important because they consider the movement of all solvent molecules, thus, this model is considered more realistic.

Table 4. Values of A_{iso} of the Water in the presence of $[\text{Gd}(\text{DTPA-BMA})(\text{H}_2\text{O})]$.

Water in the presence of $[\text{Gd}(\text{DTPA-BMA})(\text{H}_2\text{O})]$		
	A_{iso}	
	^1H / MHz	^{17}O / MHz
$A_{\text{iso}}^{\text{eq}}$ (PBE1PBE(H_2O)/PBE1PBE(H_2O))	0.33	0.89
$A_{\text{iso}}^{\text{eq}}$ (PBE1PBE (H_2O)/PCM// PBE1PBE (H_2O))	0.55	0.75
$A_{\text{iso}}^{300\text{K}}$ (MD(H_2O)/MD(H_2O))	0.95	0.72
Experimental	-	0.61

As already mentioned, thermal effects are important. However, for our proposal of a new contrast agent this effect was neglected, in fact despite the importance of this effect, our objective is to verify if the hybrid compound can be used as CA. In this way, to reduce the computational cost, we perform calculations only with the balance structure. Thus, it was made A_{iso} calculations only with the lowest energy conformer of hybrids (δ -FeOOH(100).[Gd(DTPA)(H₂O)]²⁻, δ -FeOOH(100).[Gd(DTPA-BMA)(H₂O)]). The values of A_{iso} for the hybrid compounds (Tab. 5) show that

both significantly increase. For the first hybrids δ -FeOOH(100).[Gd(DTPA)(H₂O)]²⁻ values of 4.25 MHz and 5.30 MHz were obtained for the ¹H e ¹⁷O atoms, respectively. For the hybrid δ -FeOOH(100).[Gd(DTPA-BMA)(H₂O)] the values of A_{iso} were found to be 4.15 MHz and 5.15 MHz, respectively. Thus, it is noted that the hybrid compounds can be promising contrast agents for MRI since they showed a significant increase in the values of A_{iso} . Figure 4 shows the structures of hybrid compounds.

Table 5. Values of A_{iso} of the water in the presence of hybrids.

Water in the presence of δ -FeOOH (100).[Gd(DTPA)(H ₂ O)] ²⁻		
	A_{iso}	
	¹ H / MHz	¹⁷ O / MHz
A_{iso} (PBE1PBE(H ₂ O)//PBE1PBE(H ₂ O))	4.25	5.30
Water in the presence of δ -FeOOH(100).[Gd(DTPA-BMA)(H ₂ O)]		
A_{iso} (PBE1PBE(H ₂ O)//PBE1PBE(H ₂ O))	4.15	5.15

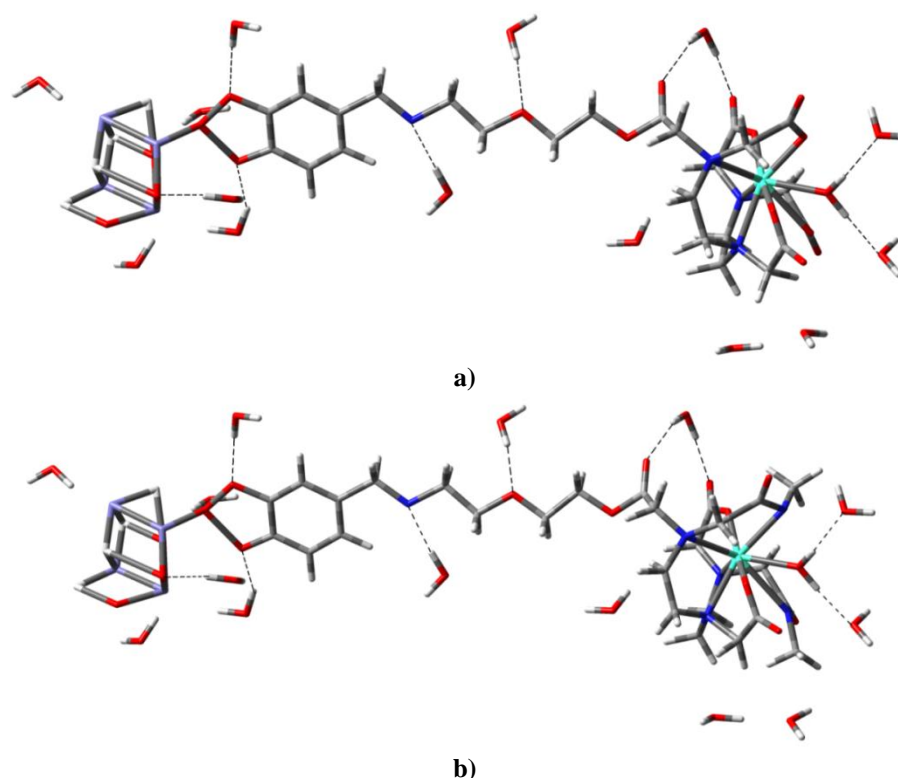


Figure 4. Structures of hybrid compounds. a) δ -FeOOH(100).[Gd(DTPA)(H₂O)]²⁻ b) δ -FeOOH(100).[Gd(DTPA-BMA)(H₂O)].

4. Conclusions

This work proposed a new hybridizing contrast agent, δ -FeOOH(100).[Gd(DTPA-BMA)(H₂O)],

capable of increasing both T_1 and T_2 relaxation times. The results allow to conclude that the hybrid compound may be an alternative to the classical contrast agents.

The interaction between solvent (water) and solute (complex) significantly influences the results, that way, this is a central concern in computational chemistry simulations. Thus, the calculations suggest that the use of implicit solvent did not influence the results, showing that the solvation sphere was adequate. Therefore, the proposed hybrid compound may be a promising contrast agent for MRI.

Acknowledgments

The authors wish to thank the financial support the Conselho Nacional de Desenvolvimento Científico e Tecnológico—Brazil (CNPq) and the Fundação de Amparo à Pesquisa do Estado de Minas Gerais—Brazil (FAPEMIG). This work was also supported by Long-term development plan UHK.

References

- [1] Merbach, A. E., Helm, L., Tóth, É., *The Chemistry of Contrast Agents in Medical Magnetic Resonance Imaging*, 2nd ed., Wiley, New York, 2013. <https://doi.org/10.1002/9781118503652>.
- [2] Sandra, S., Jativa, S. D., Kaittanis, C., Normand, G., Grim, J., Perez, J. M., Gadolinium-Encapsulating Iron Oxide Nanoprobe as Activatable NMR/MRI Contrast Agent, *ACS Nano* 6 (8) (2012) 7281-7294. <https://doi.org/10.1021/nn302393e>.
- [3] Merbach, A. E., Tóth, É., *The Chemistry of Contrast Agents in Medical Magnetic Resonance Imaging*, John Wiley & Sons, Chichester, 2001.
- [4] Platas-Iglesias, C., *The Solution Structure and Dynamics of MRI Probes Based on Lanthanide(III) DOTA as Investigated by DFT and NMR Spectroscopy*, *European Journal of Inorganic Chemistry* 2012 (12) (2012) 2023-2033. <https://doi.org/10.1002/ejic.201101164>.
- [5] Esteban-Gómez, D., de Blas, A., Rodríguez-Blas, T., Helm, L., Platas-Iglesias, C., Hyperfine Coupling Constants on Inner-Sphere Water Molecules of GdIII-Based MRI Contrast Agents, *ChemPhysChem* 13 (16) (2012) 3640-3650. <https://doi.org/10.1002/cphc.201200417>.
- [6] Caravan, P., Ellinson, J. J., McMurry, T. J., Lauffer R. B., *Gadolinium(III) Chelates as MRI Contrast Agents: Structure, Dynamics, and Applications*, *Chemical Reviews* 99 (9) (1999) 2293-2352. <https://doi.org/10.1021/cr980440x>.
- [7] Werner, E. J., Datta, A., Jocher, C. J., Raymond, K. N., *High-Relaxivity MRI Contrast Agents: Where Coordination Chemistry Meets Medical Imaging*, *Angewandte Chemie International Edition* 47 (45) (2008) 8568-8580. <https://doi.org/10.1002/anie.200800212>.
- [8] Schwarz, S., Fernandes, F., Sanroman, L., Hodenius, M., Lang C., Himmelreich, U., Schmitz-Rode, T., Schueler, D., Hoehn, M., Zenke, M., Hieronymus, T., Synthetic and biogenic magnetite nanoparticles for tracking of stem cells and dendritic cells, *Journal of Magnetism and Magnetic Materials* 321 (10) (2009) 1533-1538. <https://doi.org/10.1016/j.jmmm.2009.02.081>.
- [9] Klug, G., Kampf, T., Bloemer, S., Bremicker, J., Ziener, C. H., Heymer, A., Gbureck, U., Rommel, E., Nöth, U., Schenk, W. A., Jakob, P. M., Bauer, W. R., Intracellular and extracellular T_1 and T_2 relaxivities of magneto-optical nanoparticles at experimental high fields, *Magnetic Resonance in Medicine* 64 (6) (2010) 1607-1615. <https://doi.org/10.1002/mrm.22557>.
- [10] Li Y., Yang Z., Wang B., Liu Z., Li S., Gd-complex labeled magnetite nanoparticles as fluorescent and targeted magnetic resonance imaging contrast agent, *Materials Letters* 98 (2013) 34-37. <https://doi.org/10.1016/j.matlet.2013.01.134>.
- [11] Davenport, A., Whiting, S., Profound Pseudohypocalcemia Due to Gadolinium (Magnevist) Contrast in a Hemodialysis Patient, *American Journal of Kidney Diseases* 47 (2) (2006) 350-352. <https://doi.org/10.1053/j.ajkd.2005.10.024>.
- [12] Kartamihardja, A. A. P., Nakajima, T., Kameo, S., Koyama, H., Tsushima, Y., Impact of Impaired Renal Function on Gadolinium Retention After Administration of Gadolinium-Based Contrast Agents in a Mouse Model, *Investigative Radiology* 51 (10) (2016) 655-660. <https://doi.org/10.1097/RLI.0000000000000295>.
- [13] Bloem, J. L., Wondergem, J., Gd-DTPA as a contrast agent in CT, *Radiology* 171 (2) (1989) 578-579. <https://doi.org/10.1148/radiology.171.2.2704827>.
- [14] Frisch, M. J., Trucks, G. W., Schlegel, H. B., Scuseria, G. E., Robb, M. A., Cheeseman, J. R., Scalmani, G., Barone, V., Mennucci, B., Petersson, G. A., Nakatsuji, H., Caricato, M., Li, X., Hratchian, H. P., Izmaylov, A. F., Bloino, J., Zheng, G., Sonnenberg, J. L., Hada, M., Ehara, M., Toyota, K., Fukuda, R., Hasegawa, J., Ishida, M., Nakajima, T., Honda, Y., Kitao, O., Nakai, H., Vreven, T., Montgomery, J. A.,

- Peralta, J. E., Ogliaro, F., Bearpark, M., Heyd, J. J., Brothers, E., Kudin, K. N., Staroverov, V. N., Kobayashi, R., Normand, J., Raghavachari, K., Rendell, A., Burant, J. C., Iyengar, S. S., Tomasi, J., Cossi, M., Rega, N., Millam, J. M., Klene, M., Knox, J. E., Cross, J. B., Bakken, V., Adamo, C., Jaramillo, J., Goperts, R., Stratmann, R. E., Yazyev, O., Austin, A. J., Cammi, R., Pomelli, C., Ochterski, J. W., Martin, R. L., Morokuma, K., Zakrzewski, V. G., Voth, G. A., Salvador, P., Dannenberg, J. J., Dapprich, S., Daniels, A. D., Farkas, O., Foresman, J. B., Ortiz, J. V., Cioslowski, J., Fox, D. J., Gaussian 09, Revision B.01. Gaussian Inc., Wallingford, 2010.
- [15] Stewart, J. J. P., Optimization of parameters for semiempirical methods V: Modification of NDDO approximations and application to 70 elements, *Journal of Molecular Modeling* 13 (12) (2007) 1173-1213. <https://doi.org/10.1007/s00894-007-0233-4>.
- [16] Mancini, D. T., Souza, E. F., Caetano, M. S., Ramalho, T. C., ⁹⁹Tc NMR as a promising technique for structural investigation of biomolecules: theoretical studies on the solvent and thermal effects of phenylbenzothiazole complex, *Magnetic Resonance in Chemistry* 52 (4) (2014) 129-137. <https://doi.org/10.1002/mrc.4043>.
- [17] Adri van Duin, ReaxFF User Manual, 2002.
- [18] Helgaker, T., Jaszuński, M., Ruud, K., Ab Initio Methods for the Calculation of NMR Shielding and Indirect Spin-Spin Coupling Constants, *Chemical Reviews* 99 (1) (1999) 293-352. <https://doi.org/10.1021/cr960017t>.
- [19] Scilab 2.7 GNU Linux, Windows 9X/NT/2000/XP, Solaris 1989-2003 INRIA/ENPC. <https://www.scilab.org/>.
- [20] Coutinho, K., Canuto S., Solvent Effects from a Sequential Monte Carlo - Quantum Mechanical Approach, *Advances in Quantum Chemistry* 28 (1997) 89-105. [https://doi.org/10.1016/S0065-3276\(08\)60209-9](https://doi.org/10.1016/S0065-3276(08)60209-9).
- [21] Gonçalves, M. A., Peixoto, F. C., da Cunha, E. F., Ramalho, T. C., Dynamics, NMR parameters and hyperfine coupling constants of the Fe₃O₄(1 0 0)-water interface: Implications for MRI probes, *Chemical Physics Letters* 609 (2014) 88-92. <https://doi.org/10.1016/j.cplett.2014.06.030>.
- [22] Goncalves, A. da S., França, T. C. C., Caetano, M. S., Ramalho, T. C., Reactivation steps by 2-PAM of tabun-inhibited human acetylcholinesterase: reducing the computational cost in hybrid QM/MM methods, *Journal of Biomolecular Structure and Dynamics* 32 (2) (2014) 301-307. <https://doi.org/10.1080/07391102.2013.765361>.
- [23] Ramalho, T. C., da Cunha, E. F. F., Alencastro, R. B., Solvent effects on ¹³C and ¹⁵N shielding tensors of nitroimidazoles in the condensed phase: a sequential molecular dynamics/quantum mechanics study, *Journal of Physics: Condensed Matter* 16 (34) (2004) 6159-6170. <https://doi.org/10.1088/0953-8984/16/34/015>.
- [24] Coutinho, K., Canuto, S., Zerner, M. C., A Monte Carlo-quantum mechanics study of the solvatochromic shifts of the lowest transition of benzene, *The Journal of Chemical Physics* 112 (22) (2000) 9874. <https://doi.org/10.1063/1.481624>.
- [25] Coutinho, K., Georg, H. C., Fonseca, T. L., Ludwig, V., Canuto, S., An efficient statistically converged average configuration for solvent effects, *Chemical Physics Letters* 437 (1-3) (2007) 148-152. <https://doi.org/10.1016/j.cplett.2007.02.012>.
- [26] Lepage, M., Gore, J. C., Contrast mechanisms in magnetic resonance imaging, *Journal of Physics: Conference Series* 3 (2004) 78-86. <https://doi.org/10.1088/1742-6596/3/1/008>.
- [27] Yazyev, O. V., Helm, L., Nuclear Spin Relaxation Parameters of MRI Contrast Agents – Insight from Quantum Mechanical Calculations, *European Journal of Inorganic Chemistry* 2008 (2008) 201-211. <https://doi.org/10.1002/ejic.200701013>.

Evaluation of the phenyl-bonded silica-based sorbent for pre-concentration of the booster antifouling biocides Zinc Pyrithione, Zineb and Ziram using solid-phase extraction technique and Inductively Coupled Plasma Mass Spectrometry

Ana Marta Cavinato Marchini Rolisola^{1†}, Amauri Antônio Menegário¹, Lauren Nozomi Marques Yabuki², Luciana Polese¹, Chang Hung Kiang¹

1. São Paulo State University (Unesp), Environmental Studies Center, Rio Claro, São Paulo, Brazil

2. São Paulo State University (Unesp), Institute of Geosciences and Exact Sciences, Rio Claro, São Paulo, Brazil

†Corresponding author: Ana Marta Cavinato Marchini Rolisola, Phone: +55 19 3526-9491, Email address: anamartarolisola@hotmail.com

ARTICLE INFO

Article history:

Received: October 22, 2019

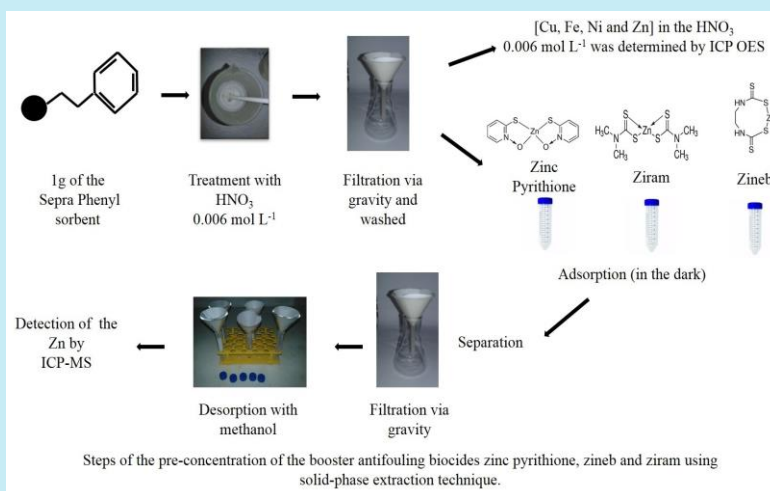
Accepted: March 30, 2020

Published: October 01, 2020

Keywords:

1. antifouling
2. zinc pyrithione
3. zineb
4. ziram
5. solid-phase extraction

ABSTRACT: A robust method of solid-phase extraction technique with use of the phenyl-bonded silica-based sorbent (Si-PH sorbent) for pre-concentration of three booster antifouling biocides: zinc pyrithione, Zineb and Ziram in ultrapure water fortified and estuarine water sample was evaluated for zinc determination by collision cell technology-inductively coupled plasma-mass spectrometry (CCT-ICP-MS). Decontamination process to remove metals and prevent (trans-) metallization of the Si-PH sorbent with 20 mL of nitric acid 0.006 mol L⁻¹ was performed. This proposed solid-phase extraction efficiency of three booster antifouling biocides by the phenyl-bonded silica-based sorbent (Si-PH sorbent) was evaluated in 40 mL of ultrapure water fortified sample (40 µg L⁻¹ of the zinc biocides). The adsorption of zinc pyrithione, Zineb and Ziram were 94.2 ± 0.1%, 85.13 ± 0.04% and 93.35 ± 0.09%, respectively. The limit of detection and limit of quantification values obtained were 0.66 µg L⁻¹ and 2.19 µg L⁻¹, respectively. Good recoveries of zinc pyrithione (85 ± 2%), Zineb (89 ± 5%) and Ziram (111 ± 2%) in the elution step for booster antifouling biocides from the fortified estuarine water were obtained.



1. Introduction

The contamination of the marine environment by metals is mainly due to impact of anthropic activities. In areas where the nautical activity is intense, such as ports, marinas and docks, risk of contamination is significant due to circulation of ships and boats. To avoid biological fouling, ships and vessels treat the hull with antifouling paint. Consequently, application of antifouling paints helps to prevent the settlement and growth of

algae, mussels, and other marine organisms in the hulls of vessels and small ship. However, antifouling particles are released into the seawater gradually from these antifouling paints that were applied on the hulls of vessels and small ship representing risk to marine organisms. In 2001, International Maritime Organization (IMO) prohibited tributyltin (TBT) in antifouling paints applied on ships¹. So, a new generation of booster antifouling biocides has been used: chlorothalonil, dichlofluanid, Irgarol 1051, TCMS pyridine,

thiocyanatomethylthio-benzothiazole (TCMTB), diuron, dichloro-octylisothiazolin (DCOIT, Sea Nine 211), zinc and copper pyrithione (zinc and copper omadine), Zineb (zinc ethylenebisdithiocarbamate) and Ziram (zinc dimethyldithiocarbamate)²⁻⁴. Recently, there is a considerable increase in the use of zinc pyrithione (Zn(PT)₂) and copper pyrithione (Cu(PT)₂), in freshwater and seawater booster antifouling biocides, because their antimicrobial and antifungal activity is highly effective⁵.

The effects and toxicity of booster antifouling biocides on different species of fish, crustaceans, invertebrates, and algae were studied⁶. Studies with sea urchin eggs and embryos demonstrated that Zn(PT)₂ (0.01 fg L⁻¹) is more toxic than Cu(PT)₂ (1,000 fg L⁻¹)⁷. The Zn(PT)₂ showed similar toxicity to TBT for ascidian *Botryllus schlosseri* cultured hemocytes in extremely low concentrations 31.7 µg L⁻¹ and 158 µg L⁻¹, respectively⁸. The sublethal exposure of mussels in the 14-day period to Zn(PT)₂ (0.2 or 2 mmol L⁻¹), along with inorganic Zn and seawater controls) was considered genotoxic for mussel haemocytes⁹. The authors showed in the acute toxicity study of Zn(PT)₂ in fish *Carassius sp.* that the concentration required to kill half the members of a tested population after a specified test duration - 96 h (Lethal Concentration 50% - LC50 96 h) of Zn(PT)₂ in *Carassius sp.* cultivated in freshwater or water with 1.5 or 3‰ salinity was 0.163, 0.126 and 0.113 mg L⁻¹, respectively¹⁰. Acute toxicity of booster antifouling biocides was determined for phytoplankton *Nitzschia pungens* and zooplankton *Artemia* larvae showed a half maximal effective concentration (EC50 96 h) for Zineb (232 µg L⁻¹), Zn(PT)₂ (5.5 µg L⁻¹), Ziram (5.4 µg L⁻¹), Cu(PT)₂ (4.9 µg L⁻¹) in phytoplankton *Nitzschia pungens*. In zooplankton *Artemia* larvae, the booster antifouling biocides present LC50 (48 h, for larval survivals) for Zineb (41 mg L⁻¹), Ziram (4.8 mg L⁻¹), Zn(PT)₂ (3.2 mg L⁻¹) and Cu(PT)₂ (0.3 mg L⁻¹)¹¹.

The development of analytical methods to determine environmental concentrations of these booster antifouling biocides (e.g. zinc pyrithione - Zn(PT)₂, Zineb and Ziram) in complex matrices (e.g. estuarine water and seawater samples) is of great relevance due to the mechanisms of the oxidation and (trans-) metallization that currently complicate chromatographic analysis and other studies¹². For the quantification of trace level analytes (µg L⁻¹ or ng L⁻¹) in complex matrices, it

is necessary to use a sample preparation step. This step aims for the pre-concentration of analytes and the removal of interferents¹³⁻¹⁵. Solid-Phase Extraction (SPE) has a great potential to provide proper pre-concentration for ultra-trace analysis of booster antifouling biocides. In addition, SPE avoids coelution of the matrix interferents along with the compounds of interest when High Performance Liquid Chromatography (HPLC) is used and an important advantage of SPE is the possibility of extracting a wide range of analytes (from non-polar to very polar analytes) from a wide variety of samples¹⁶. SPE as an aqueous sample preparation step should consider the characteristics of the sorbent, matrix solvents used in the conditioning and elution steps, analyte of interest and detector used to quantify the analyte.

Several methods have been used to pre-concentrate the booster antifouling biocides by using, pre-column cartridge^{17,18}, adsorbent column¹⁹ commercial cartridges^{20,21}, extraction disks²² and C18-functionalized paramagnetic nanoparticles²³. Different hyphenated instrumental methods have been used to determinate the booster antifouling biocides over the years, e.g. HPLC coupled with: i) Ultraviolet-Visible (UV-VIS)^{10,12,17,20,23-26}, ii) Diode-Array (DAD)¹², iii) Electrospray Ionization Mass Spectrometry (ESI-MS)¹², iv) Atmospheric Pressure Chemical Ionization Mass Spectrometry (APCI-MS)^{18,25}, v) Tandem-Mass Spectrometry (MS/MS)^{26,27}, vi) Atomic Absorption Spectrometry²⁸, vii) fluorescence²⁹.

Specifically, for Ziram and Zineb, the amount of zinc present in booster antifouling biocide was determined by Flame Atomic Absorption Spectrometry (Flame-AAS) and spectrophotometry after separation using HPLC³⁰ and for residue analysis of Zineb 68% + Hexaconazole 4% mixture was used Gas Chromatography Coupled with Triple Quadrupole Mass Spectrometry (GC-MS/MS)³¹.

The aim of this work was to evaluate the phenyl-bonded silica-based sorbent (Septra Phenyl, Phenomenex) for pre-concentration booster antifouling biocides zinc pyrithione, Zineb and Ziram from the estuarine water sample using SPE technique. For the first time this sorbent was used to pre-concentrate the zinc-based booster antifouling biocides zinc pyrithione, Zineb and Ziram from the ultrapure water fortified sample (40 µg L⁻¹) and estuarine water sample with metal removal to prevent (trans-) metallization.

2. Experimental

2.1 Materials and reagents

The booster antifouling biocides zinc pyrithione (purity $\geq 95\%$, CAS 13463-41-7), Zineb Pestanal[®] (purity 97%, CAS 12122-67-7) and Ziram Pestanal[®] (purity 97%, CAS 137-30-4) were obtained from Sigma-Aldrich (Brazil). Dimethylsulfoxide (DMSO) was supplied by LABSYNTH (Brazil); HPLC grade methanol (MeOH) was purchased from Panreac (Spain); nitric acid (HNO₃) was obtained from Merck (Germany); resin Chelex[®]-100 (Na form, 100-200 wet mesh) was supplied by Bio-Rad (Canada). The Septra Phenyl Sorbent (endcapped silica-based phenyl, 50 μm , 65 Å , ≤ 10 kDa) were obtained from Phenomenex (USA) and commonly applied to reversed phase, hydrophobic and aromatic, small molecule selectivity from aqueous samples. Quantitative filter paper C42 blue strip, diameter 12.5 cm was supplied Unifil (Germany) and 0.22 μm nylon filter (disk) Allcrom (Brazil).

Ultrapure water (18 M Ω cm resistivity) obtained with a Millipore system (Millipore,

Bedford, MA) was used exclusively. The stock solutions of 200 mg L⁻¹ each booster antifouling biocide (Zn(PT)₂, Zineb and Ziram) was prepared in DMSO monthly and stored in the refrigerator at 4 °C (in dark).

2.2 Instrumentation

The Inductively Coupled Plasma Optical Emission Spectrometer (ICP OES) model iCAP 6000 Series (Thermo Scientific, Germany) was used to determine the higher concentrations of zinc and other metals presented in solution of HNO₃ 0.006 mol L⁻¹ and 1.6 mol L⁻¹ used in decontamination processes. An Inductively Coupled Plasma Mass Spectrometry (ICP-MS) model X Series II (Thermo Scientific, Germany) was used to zinc determination in the ultrapure water fortified sample, estuarine water sample of the Santos/SP Estuary (Brazil) and methanol of the elution step. [Tab. 1](#) reports the instrumental and analytical parameters. The instrument was optimized before each reading with a 10 ng mL⁻¹ standard tune solution (Ba, Be, Bi, Ce, Co, In, Li, Ni, Pb and U).

Table 1. Instrumental and Analytical Parameters of ICP-MS.

Parameter	Configuration Used
RF power	1,350 W
Nebulizer	Mira Mist [®]
Spray chamber	Glass Conical Impact Bead
Torch	1-Piece, 1.5 mm injector diameter
Interface Cones	Ni sampler and skimmer
Sample uptake rate	1 mL min ⁻¹ , approx., pumped
Quadrupole resolution	Standard resolution mode: peak width 0.70 amu at 5 % height
Nebulizer gas	0.75 L min ⁻¹
Plasma gas	13 L min ⁻¹
Auxiliary gas	0.7 L min ⁻¹
Monitored mass	Zn m/z 64
Dwell time	10 ms
CCT gas (He 5.0 - analytical)	8.3 mL min ⁻¹
Acquisition mode	Peak jumping
Internal Standard Isotopes	⁴⁵ Sc and ⁸⁹ Y

2.3 Decontamination processes

2.3.1 Glassware and plastic materials, quantitative filter paper and 0.22 μm nylon filter

All glassware and plastic materials were submerged in HNO₃ 3.2 mol L⁻¹ for 4 h, rinsed with ultrapure water and posteriorly, dried in

laminar flow hood. The quantitative filter paper (used in the gravity filtration of Si-PH sorbent) and 0.22 μm nylon filters (used in vacuum filtration of MeOH) was decontaminated by placing in HNO₃ 1.6 mol L⁻¹ for 4 h. Then they were washed with ultrapure water until pH = 6.0 and dried in a laminar flow hood.

The decontamination process on the glass or

plastic materials, the quantitative filter paper, 0.22 μm nylon filter and the Si-PH sorbent was performed for Zn removal (possibly presented in these materials with overestimation risk of the real Zn concentration in estuarine water samples). Further Zn, the metal removal (Cr, Cu, Fe and Ni, for example) was also performed to avoid the possible (trans-) metallization of these metals with the zinc-based antifouling biocides¹². Therefore, chromium, copper, iron, nickel and zinc concentrations present in HNO_3 used for decontamination were determined by ICP OES. This determination was performed by ICP OES due to the possible presence of these metals in higher concentrations, without a requirement for the detection technique with a higher sensibility as ICP-MS.

2.3.2 Zinc removal in methanol with Chelex[®]-100 resin

The zinc amount in the treated and not treated MeOH with Chelex[®]-100 resin (200-400 mesh, sodium form) was evaluated. For the treated MeOH, 0.1 g of Chelex[®]-100 resin was added in 25 mL of MeOH. This mixture remained for 10 min under constant stirring and 10 min at rest. The zinc amount was determined by ICP-MS from 10 mL of a MeOH solution 5% (v v^{-1}) treated with the Chelex[®]-100 resin and another MeOH solution 5% (v v^{-1}) not treated with the Chelex[®]-100 resin. Posteriorly, for the Zn removal present in the MeOH (used in extraction of the booster antifouling biocides), 2.0 g of Chelex[®]-100 resin were placed in 500 mL of MeOH under constant stirring for 10 min followed by 10 min at rest. Then the MeOH was vacuum filtered using 0.22 μm nylon filter decontaminated and stored in a 500 mL glass bottle.

2.3.3 Removal of the metals present in phenyl-bonded silica based sorbent

To metal removal of the Si-PH sorbent, 1.0 g of the Si-PH sorbent in 20 mL of HNO_3 0.006 mol L^{-1} was placed under constant stirring for 20 min. The Si-PH sorbent was then filtered using the gravity filtration technique and washed with 150 mL of ultrapure water until reach $\text{pH} = 6.0$. The chromium, copper, iron, nickel and zinc present in HNO_3 0.006 mol L^{-1} solution were determined by ICP OES.

2.4 Adsorption and recovery of Zn(PT)_2 , Zineb and Ziram by the Si-PH sorbent in the ultrapure water fortified sample

In order to evaluate the adsorption and elution of Zn(PT)_2 , Zineb and Ziram by the Si-PH sorbent, tests were firstly performed with ultrapure water fortified sample. Since no data of booster antifouling biocides was available for the study area and to prevent possible analyte losses in the experiment, the accuracy of the developed method was carried out at a higher level of fortification (40 $\mu\text{g L}^{-1}$). Using three falcon tubes, 50 mL of the ultrapure water was placed in each tube and was added Zn(PT)_2 in the first tube, Zineb in the second tube and Ziram in the third tube for final concentration of 40 $\mu\text{g L}^{-1}$ of the each biocide ($\text{pH} = 6.5$ and $T = 21.5$ $^\circ\text{C}$). This procedure was performed in triplicate for each booster antifouling biocide.

A 10 mL aliquot of the solution was withdrawn before and after the experiment with Si-PH sorbent. Determination of zinc in each solution containing Zn(PT)_2 , Zineb and Ziram by ICP-MS was performed using 10 mL of each solution and acidified with HNO_3 3.2 mol L^{-1} (1.2 mL) and added ultrapure water (0.8 mL) to a final concentration of HNO_3 0.32 mol L^{-1} . This test was performed in duplicate for each booster antifouling biocide.

The conditioning and equilibration step was performed using 1 g of decontaminated Si-PH sorbent. To condition and equilibrate the Si-PH sorbent the gravity filtration technique was used and 10 mL of methanol and 10 mL of ultrapure water were added, respectively. A mass equal 1 g of Si-PH sorbent (conditioned and equilibrated) was transferred to a falcon tube containing 40 mL of Zn(PT)_2 , Zineb and Ziram solution (40 $\mu\text{g L}^{-1}$). The falcon tube containing the solution and Si-PH sorbent was kept under constant stirring for 1 h in the dark to prevent photodegradation. After stirring, the falcon tube was remained at rest for 10 min to decant the Si-PH sorbent before removing the final aliquot. Zinc determination by ICP-MS in the initial and final aliquots allowed to calculate the adsorbed zinc mass and adsorption percentage of the Zn(PT)_2 , Zineb and Ziram booster antifouling biocides in 1 g of Si-PH sorbent. The adsorbed zinc mass was calculated by the concentration obtained by ICP-MS multiplied by the dilution factor (1.2) and the volume of the solution (40). The percentage (%)

of adsorption was calculated using the values of initial concentration (C_i) and final concentration (C_f) of the solution by means of Eq. 1:

$$\% \text{ Adsorption} = (C_i - C_f/C_i) \times 100. \quad (1)$$

2.5 Adsorption and recovery of Zn(PT)₂, Zineb and Ziram by the Si-PH sorbent in the water sample of the Santos/SP Estuary (Brazil)

The estuarine water sample was collected in the Estuary of Santos/SP (Brazil) downstream at latitude S22°51'30" and longitude W46°18'29". A 6 L plastic bottle of mineral water was washed three times with ultrapure water and three times with the estuarine water. The non-filterable water sample was not acid preserved but the following experiments were performed at maximum 14 days after the sampling (as preconized EPA SW-846 recommendations)³².

To evaluate the adsorption and recovery of the booster antifouling biocides by the Si-PH sorbent using water sample of the Santos Estuary/SP, 500 mL of the estuarine water was removed from the refrigerator one day prior to the experiment, transferred to a beaker and held at room temperature to decant the sediment.

In order to determine the zinc concentrations in the estuarine water sample prior to fortification with booster antifouling biocides Zn(PT)₂, Zineb and Ziram, the analysis were performed by Collision Cell Technology (CCT)-ICP-MS. The collision cell technology (CCT) features a cell introduced before the mass analyzer which was used in ICP-MS to provide an effective elimination of spectral interferences mainly, polyatomic interferences (i.e. ³⁶Ar¹⁴N₂).

Using three falcon tubes, 50 mL of the estuarine water was placed in each tube and the sample was added Zn(PT)₂ in the first tube, Zineb in the second tube and Ziram in the third tube for final concentration of the 100 µg L⁻¹ (pH = 7.8 and T = 21.5 °C). This procedure was performed in triplicate for each booster antifouling biocide.

Before adding the Si-PH sorbent and after end experiment, a 10 mL aliquot of the fortified estuarine water sample was removed. Determination of zinc in each sample containing Zn(PT)₂, Zineb and Ziram by CCT-ICP-MS was performed using only 0.5 mL of each solution and acidified with HNO₃ 3.2 mol L⁻¹ (1 mL) and added ultrapure water (8.5 mL) to a final concentration of HNO₃ 0.32 mol L⁻¹.

A mass equal 1 g of decontaminated, conditioned and equilibrated Si-PH sorbent was transferred to each falcon tube containing 40 mL of Zn(PT)₂, Zineb and Ziram. The falcon tube containing fortified estuarine water sample and the Si-PH sorbent was under constant stirring for 1 h in the dark to prevent photodegradation.

After stirring, the falcon tube was held to decant the Si-PH sorbent before removing the final aliquot. Determination of zinc by CCT-ICP-MS in the initial and final aliquots allowed the calculation of the adsorbed zinc mass and the percentage adsorption of the Zn(PT)₂, Zineb and Ziram biocides in 1 g of Si-PH sorbent in the estuarine water sample. The adsorbed zinc mass was calculated by the concentration obtained by ICP-MS multiplied by the dilution factor (20) and the volume of the solution (40).

Then, gravity filtration of the remainder of the sample (estuarine water and Si-PH sorbent) was performed on the falcon tube. The Si-PH sorbent that remained on the filter paper was washed with 5 mL of ultrapure water and transferred to another decontaminated quantitative filter paper. The sorbent transfer to another filter paper was performed to avoid that residues of the booster antifouling biocides that were not adsorbed by the sorbent and remained on the filter paper were eluted and consequently would overestimate the recovery values.

Initially, 1 mL of 100% MeOH (v v⁻¹) to elute the Zn(PT)₂, Zineb and Ziram from the Si-PH sorbent was used. However, this volume was not enough to cover the mass of 1 g of Si-PH. So, 5 aliquots of 1 mL (total = 5 mL) of 100% MeOH (v v⁻¹) previously treated with Chelex[®]-100 were added under Si-PH sorbent using the gravity filtration technique with an elution rate of the 2 mL min⁻¹.

For the Zn determination in ICP-MS, 0.5 mL eluate (MeOH 100% (v v⁻¹)) each booster antifouling biocide was diluted with 8.5 mL ultrapure water and acidified with 1 mL HNO₃ 3.2 mol L⁻¹. The eluate dilution was 20-fold, resulting in a final concentration of 5% (v v⁻¹) for MeOH and 2% (v v⁻¹) for HNO₃. This dilution was necessary because the introduction of organic solvents in the ICP-MS can cause signal suppression, as the intensity the signal is directly related to the concentration of methanol³³.

A solution containing MeOH 5% (v v⁻¹) and HNO₃ 2% (v v⁻¹) was nebulized for 15 minutes to stabilize the plasma before analysis of calibration

curve and samples. The calibration curve of 0, 5, 10, 25, 50 and 75 $\mu\text{g L}^{-1}$ was prepared using the same MeOH and HNO_3 concentrations of the eluate and the stabilization solution.

2.6 Limit of detection and quantification

The procedure for determining the limit of detection and quantification of the proposed method was performed in the elution step (triplicate). The limit of detection and quantification of the SPE method developed was calculated by multiplying the standard deviation of zinc obtained in the eluate by 3 and by 10, respectively.

The limit of detection and quantification of this SPE method proposed was estimated according IUPAC recommendations by multiplying the standard deviation of zinc obtained in the eluate (blanks) by 3 and by 10, respectively. Subsequently, the zinc concentration obtained in the eluate (blanks) in this experimental procedure was subtracted from the eluent of the biocides in the $\text{Zn}(\text{PT})_2$, Zineb and Ziram recovery test by the Si-PH sorbent in the water sample from the Santos/SP Estuary³⁴.

3. Results and Discussion

3.1 Decontamination processes

3.1.1 Removal of zinc present in methanol with Chelex[®]-100 resin

The Zn amount present in the not treated MeOH solution decreases from $18 \pm 1 \mu\text{g L}^{-1}$ to $3 \pm 0.1 \mu\text{g L}^{-1}$ compared with the treated MeOH solution indicating a reduction of approximately

83%. Therefore, the methanol treated with Chelex[®]-100 resin was used in the SPE method development.

3.1.2 Removal of the metals present in phenyl-bonded silica based sorbent

The concentrations of the Cr, Cu, Fe, Ni, and Zn metals were determined quantitatively in a volume of 20 mL of HNO_3 0.006 mol L^{-1} used in the Si-PH sorbent decontamination process by and the results are presented in Tab. 2.

It was observed that Zn has the highest concentration ($174 \pm 1 \mu\text{g L}^{-1}$) followed by Fe ($28 \pm 1 \mu\text{g L}^{-1}$) and Ni ($15.9 \pm 0.8 \mu\text{g L}^{-1}$). The concentrations of Cu and Cr metals were below $8 \mu\text{g L}^{-1}$. Based on these results, it is demonstrated the need of carrying out the Si-PH sorbent decontamination process for subsequent use in SPE of the booster antifouling biocides. This is justified by the fact that the booster antifouling biocides have Zn in their composition and this metal showed the highest concentration in the Si-PH sorbent decontamination process. It should be noted that the decontamination process avoided the (trans-) metallization of the booster antifouling biocides with the other metals present in the Si-PH sorbent.

The choice of HNO_3 concentration 0.006 mol L^{-1} used in the Si-PH sorbent decontamination process was based on the fact that the Si-PH sorbent is the silica base and its pH working range is between 2 and 8 as recommended by the manufacturer³⁵. Silica becomes unstable and may contain residual silanols resulting in irreversible adsorption of basic compounds outside this pH working range³⁶.

Table 2. Metal concentrations quantified in the Si-PH decontamination process of by ICP OES (axial view).

Solution	[Cr]/ $\mu\text{g L}^{-1}$	[Cu]/ $\mu\text{g L}^{-1}$	[Fe]/ $\mu\text{g L}^{-1}$	[Ni]/ $\mu\text{g L}^{-1}$	[Zn]/ $\mu\text{g L}^{-1}$
1	3.9 ± 0.3	8.5 ± 0.4	< LOQ	< LOQ	202 ± 2
2	3.1 ± 0.5	9.8 ± 0.7	< LOQ	15 ± 6	< LOQ
3	3.4 ± 0.1	8.1 ± 0.1	38.5 ± 0.4	< LOQ	< LOQ
4	3.4 ± 0.1	8.7 ± 0.9	< LOQ	18.60 ± 0.09	177.0 ± 0.4
5	< LOQ	7.5 ± 0.1	< LOQ	< LOQ	149.2 ± 0.7
6	3.1 ± 0.3	10.4 ± 0.4	23.9 ± 0.4	15.1 ± 0.6	192.3 ± 1.4
7	2.9 ± 0.3	7.2 ± 0.4	33.4 ± 0.4	12.5 ± 0.4	155.8 ± 0.2
8	3.1 ± 0.1	7.0 ± 0.4	30.40 ± 0.02	18.0 ± 0.4	164 ± 2
9	2.1 ± 0.9	6.8 ± 0.8	25.7 ± 1.1	14 ± 3	164.5 ± 0.6
10	2.0 ± 0.6	5.5 ± 0.4	30.8 ± 0.3	15.0 ± 0.1	< LOQ
11	< LOQ	6.3 ± 0.9	19.6 ± 1.7	13.6 ± 0.1	152.6 ± 0.6
12	< LOQ	6.7 ± 0.3	16.5 ± 0.3	14.100 ± 0.003	164 ± 2

Continue...

13	2.4 ± 0.6	7.9 ± 0.2	30 ± 3	15.0 ± 0.3	175.9 ± 0.8
14	2 ± 1	10.9 ± 0.4	27 ± 2	15.2 ± 0.2	190.9 ± 0.9
15	3.4 ± 0.4	8.6 ± 0.5	27.6 ± 0.6	15.84 ± 0.04	180.7 ± 0.9
16	2.7 ± 0.4	8.4 ± 0.2	40.9 ± 0.8	18.8 ± 0.1	17 ± 1
17	3 ± 1	7 ± 1.4	26 ± 4	19.9 ± 0.8	176 ± 7
18	2.3 ± 0.2	7.2 ± 0.5	18 ± 1	18.3 ± 0.1	197.7 ± 0.9
Mean ± SD	2.9 ± 0.2	7.9 ± 0.5	27.7 ± 1.1	15.9 ± 0.8	174 ± 1
LOD	0.54	1.01	1.73	0.49	0.77
LOQ	1.78	3.38	2.44	1.64	2.58
λ (nm)	283.5	324.7	259.9	231.6	213.8

3.1.3 Quantitative filter paper

Table 3 reports the concentration of the metals found in the quantitative filter paper and a zinc concentration of $156 \pm 2 \mu\text{g L}^{-1}$. Based on these results, it was concluded that it would occur overestimation of levels in the elution step of

biocides. In addition, the presence of Fe and Ni metals may contribute to (trans-) metallization with the booster antifouling biocides. Therefore, the decontaminated filter paper was used in all stages of the gravity filtration technique and especially in the elution step.

Table 3. Metal concentrations quantified in the filter paper decontamination process by ICP OES (axial view) (n = 15).

Solution of HNO ₃	[Cr]/ μg L ⁻¹	[Cu]/ μg L ⁻¹	[Fe]/ μg L ⁻¹	[Ni]/ μg L ⁻¹	[Zn]/ μg L ⁻¹
Mean ± SD	< LOQ	< LOQ	194 ± 10	22 ± 3	156 ± 2
LOD	0.82	0.56	1.13	0.40	0.34
LOQ	2.74	1.86	3.76	1.32	1.12
λ (nm)	267.7	324.7	238.2	221.6	213.8

3.1.4 Adsorption and recovery of Zn(PT)₂, Zineb and Ziram by the Si-PH sorbent in the ultrapure water fortified sample

Usually, 100-200 mL of water sample is used to percolate the cartridge containing silica with a flow rate above 2 mL min⁻¹ by use of the manifold³⁷. However, the developed method used only 40 mL of sample and the direct contact and constant stirring of the Si-PH sorbent contributed to a good adsorption of the booster antifouling biocides as showed in Tab. 4. The stock solution dissolutions of the booster antifouling biocides resulted a pH value of 6.5 in the ultrapure water fortified sample which is close to that found in tropical estuarine environment water^{38,39}.

The adsorbed mass and adsorption of the booster antifouling biocides by the Si-PH sorbent

in the ultrapure water fortified solution in the SPE procedure as showed in Tab. 4.

The results evidenced that Zn(PT)₂ demonstrated good adsorption, indicating the occurrence of π-π interactions between the phenyl group present in both Si-PH sorbent and Zn(PT)₂⁴⁰. This feature is advantageous because it allows its application in the reverse phase SPE for extraction of Zn(PT)₂ from the estuarine water.

It is suggested that hydrophobic interactions could occur between the Si-PH sorbent and the Zineb and Ziram, once both have nonpolar groups at their endings and were eluted with methanol, which is used for the extraction of nonpolar analyte and moderately nonpolar analyte by use of reverse phase SPE technique.

Table 4. Adsorption of Zn(PT)₂, Zineb and Ziram by the Si-PH sorbent in SPE in ultrapure water fortified with - booster antifouling biocides (n=3).

Analyte	[Zn] In. Sol. / μg L ⁻¹	[Zn] Final Sol. / μg L ⁻¹	Adsorbed Mass / μg (% RSD)	Adsorption / %
Zn(PT) ₂	36.6 ± 0.5	2.11 ± 0.05	1.3 ± 0.1 (9.07)	94.2 ± 0.1
Zineb	43.3 ± 0.3	6.40 ± 0.07	1.47 ± 0.02 (1.36)	85.13 ± 0.04
Ziram	49.1 ± 0.4	3.2 ± 0.1	1.83 ± 0.01 (0.73)	93.35 ± 0.09

3.1.5 Adsorption and recovery of Zn(PT)₂, Zineb and Ziram by the Si-PH sorbent in the water sample of the Santos/SP Estuary (Brazil)

The adsorbed and eluted mass and the % recovery of Zn(PT)₂, Zineb and Ziram by the Si-PH sorbent in the sample (Santos/SP estuary water) fortified with the booster antifouling biocides in the SPE procedure are presented in Tab. 5.

The type and volume of conditioning and elution solvent (methanol) used in SPE of booster antifouling biocides from estuarine water demonstrated good extraction efficiency (recoveries between ~85% and 111%) due to the fact that methanol is more polar than Si-PH sorbent and used for the extraction of nonpolar analyte and moderately nonpolar analyte⁴¹. In addition, the extraction efficiency was favored by dividing the volume of 5 mL of methanol used in the elution into 5 times of 1 mL.

The concentration factor obtained by the ratio of the initial sample volume (40 mL) to the final volume of the concentrated solution (5 mL) was 8. This concentration factor was sufficient to

quantify the zinc by ICP-MS in the eluate after the 20-fold dilution.

The recovery of Zn(PT)₂ in estuarine water (85 ± 2%) in the developed method is very close to that obtained by Grunnet and Dahllöf²⁰, where they obtained 85% recovery for Zn(PT)₂ when using cartridge Strata X in the SPE technique to pre-concentrate Zn(PT)₂ from seawater. This fact demonstrates that the use of the gravity filtration technique used in this research did not negatively influence the results obtained in the elution step.

Good recoveries for zinc pyrithione (85 ± 2%), Zineb (89 ± 5%) and Ziram (111 ± 2%) in the elution step for booster antifouling biocides from the fortified estuarine water were obtained. These results are in accordance with the recommendation of the US Environmental Protection Agency (EPA), because they accept to validate extraction methods with recovery in the range of 70% to 130%³⁷. In addition, it is emphasized that the Si-PH sorbent (phenyl-bonded) was first evaluated to adsorb the dithiocarbamates Zineb and Ziram from estuarine water.

Table 5. Zinc recovery in the Santos/SP Estuary water sample fortified with Zn(PT)₂, Zineb and Ziram (n=3).

Analyte	Adsorbed Mass / µg ± SD (% RSD)	Eluted Mass / µg ± SD (% RSD)	Recovery / %
Zn(PT) ₂	1.85 ± 0.08 (4.59)	1.5 ± 0.1 (6.27)	85 ± 2
Zineb	2.43 ± 0.08 (3.49)	2.1 ± 0.1 (7.78)	89 ± 5
Ziram	2.20 ± 0.08 (3.86)	2.45 ± 0.06 (2.60)	111 ± 2

3.1.6 Limit of detection and quantification

Based on the experimental procedure for the determination of the limit of detection and quantification of the SPE method developed, the concentration of zinc obtained in the eluate (triplicate) of this procedure was 0.9 ± 0.2 µg L⁻¹.

Therefore, the limit of detection (LOD) of the SPE analytical method using the fortified sample of estuarine water was calculated by multiplying of the standard deviation (0.2) by 3 and the limit of quantification (LOQ) by multiplying of the standard deviation (0.22) by 10. So, the LOD and LOQ values obtained for SPE were 0.66 µg L⁻¹ and 2.19 µg L⁻¹, respectively.

4. Conclusions

The metals removal procedure of the phenyl-bonded silica-based sorbent was efficient, once it

eliminated the possibility of overestimation of the values during the determination of zinc by ICP-MS and avoided the (trans-) metallization of the biocides with others metals Cr, Cu, Fe, Ni present in the Si-PH sorbent.

The results obtained in this research allow to conclude that the proposed analytical method is efficient, considering the LOD obtained of 0.66 µg L⁻¹.

Good recoveries were obtained between ~85% and 111% in the elution step of the Zn(PT)₂, Zineb and Ziram biocides in the SPE by zinc determination via ICP-MS from the fortified estuarine water without altering the pH, filtering or diluting the sample in ultrapure water.

Additionally, the proposed approach it may be useful in the sample preparation step for speciation studies of the booster antifouling biocides Zn(PT)₂, Zineb and Ziram in estuarine water, such as, in the HPLC-ICP-MS coupling

because the proposed approach pre-concentrated the sample and it eliminates the (trans-) metallization that could occur with the metals present in the evaluated sorbent.

Acknowledgments

The authors thank São Paulo Research Foundation (FAPESP grant #2015/03397-4), Brazilian National Council for Scientific and Technological Development (CNPq grant #164326/20154) and Coordination for the Improvement of Higher Education Personnel (CAPES) for financial support.

References

- [1] Yebra, D. M., Kiil, S., Dam-Johansen, K., Antifouling technology—past, present, and future steps towards efficient and environmentally friendly antifouling coatings, *Progress in Organic Coatings* 50 (2) (2004) 75-104. <https://doi.org/10.1016/j.porgcoat.2003.06.001>.
- [2] Voulvoulis, N., Scrimshaw, M. D., Lester, J. N., Analytical methods for the determination of 9 antifouling paint booster biocides in estuarine water samples, *Chemosphere* 38 (15) (1999) 3503-3516. [https://doi.org/10.1016/S0045-6535\(98\)00580-3](https://doi.org/10.1016/S0045-6535(98)00580-3).
- [3] Boxall, A. B. A., Comber, S. D., Conrad, A. U., Howcroft, J., Zaman, N., Inputs, Monitoring and Fate Modelling of Antifouling Biocides in UK Estuaries, *Marine Pollution Bulletin* 40 (11) (2000) 898-905. [https://doi.org/10.1016/S0025-326X\(00\)00021-7](https://doi.org/10.1016/S0025-326X(00)00021-7).
- [4] Thomas, K. V., The environmental fate and behaviour of antifouling paint booster biocides: A review, *Biofouling* 17 (1) (2001) 73-86. <https://doi.org/10.1080/08927010109378466>.
- [5] Almond, K. M., Trombetta, L. D., The effects of copper pyrithione, an antifouling agent, on developing zebrafish embryos, *Ecotoxicology* 25 (2) (2016) 389-398. <https://doi.org/10.1007/s10646-015-1597-3>.
- [6] Amara, I., Miled, W., Slama, R. B., Ladhari, N., Antifouling processes and toxicity effects of antifouling paints on marine environment. A review, *Environmental Toxicology and Pharmacology* 57 (2018) 115-130. <https://doi.org/10.1016/j.etap.2017.12.001>.
- [7] Kobayashi, N., Okamura, H., Effects of new antifouling compounds on the development of sea urchin, *Marine Pollution Bulletin* 44 (8) (2002) 748-751. [https://doi.org/10.1016/S0025-326X\(02\)00052-8](https://doi.org/10.1016/S0025-326X(02)00052-8).
- [8] Cima, F., Ballarin, L., Immunotoxicity in ascidians: Antifouling compounds alternative to organotin—IV. The case of zinc pyrithione, *Comparative Biochemistry and Physiology Part C: Toxicology & Pharmacology* 169 (2015) 16-24. <https://doi.org/10.1016/j.cbpc.2014.12.007>.
- [9] Dallas, L. J., Turner, A., Bean, T. P., Lyons, B. P., Jha, A. N., An integrated approach to assess the impacts of zinc pyrithione at different levels of biological organization in marine mussels, *Chemosphere* 196 (2018) 531-539. <https://doi.org/10.1016/j.chemosphere.2017.12.144>.
- [10] Ren, T., Fu, G.-H., Liu, T.-F., Hu, K.; Li, H.-R., Fang, W.-H., Yang, X.-L., Toxicity and accumulation of zinc pyrithione in the liver and kidneys of *Carassius auratus gibelio*: association with P-glycoprotein expression, *Fish Physiology and Biochemistry* 43 (1) (2017) 1-9. <https://doi.org/10.1007/s10695-016-0262-y>.
- [11] Jung, S. M., Bae, J. S., Kang, S. G., Son, J. S., Jeon, J. H., Lee, H. J., Jeon, J. Y., Sidharthan, M., Ryu, S. H., Shin, H. W., Acute toxicity of organic antifouling biocides to phytoplankton *Nitzschia pungens* and zooplankton *Artemia larvae*, *Marine Pollution Bulletin* 124 (2) (2017) 811-818. <https://doi.org/10.1016/j.marpolbul.2016.11.047>.
- [12] Doose, C. A., Szaleniec, M., Behrend, P., Müller, A., Jastorff, B., Chromatographic behavior of pyrithiones, *Journal of Chromatography A* 1052 (1-2) (2004) 103-110. <https://doi.org/10.1016/j.chroma.2004.08.028>.
- [13] Hercegová, A., Dömötörövá, M., Matisová, E., Sample preparation methods in the analysis of pesticide residues in baby food with subsequent chromatographic determination, *Journal of Chromatography A* 1153 (1-2) (2007) 54-73. <https://doi.org/10.1016/j.chroma.2007.01.008>.
- [14] Chen, Y., Guo, Z., Wang, X., Qiu, C., Sample preparation, *Journal of Chromatography A* 1184 (1-2) (2008) 191-219. <https://doi.org/10.1016/j.chroma.2007.10.026>.
- [15] Andrade-Eiroa, A., Canle, M., Leroy-Cancellieri, V., Cerdà, V., Solid-phase extraction of organic compounds: A critical review (Part I), *TrAC Trends in Analytical Chemistry* 80 (2016) 641-654. <https://doi.org/10.1016/j.trac.2015.08.015>.

- [16] Andrade-Eiroa, A., Canle, M., Leroy-Cancellieri, V., Cerdà, V., Solid-phase extraction of organic compounds: A critical review. part ii, *TrAC Trends in Analytical Chemistry* 80 (2016) 655-667. <https://doi.org/10.1016/j.trac.2015.08.014>.
- [17] Weissmahr, K. W., Houghton, C. L., Sedlak, D. L., Analysis of the Dithiocarbamate Fungicides Ziram, Maneb, and Zineb and the Flotation Agent Ethylxanthogenate by Ion-Pair Reversed-Phase HPLC, *Analytical Chemistry* 70 (22) (1998) 4800-4804. <https://doi.org/10.1021/ac980626w>.
- [18] Bones, J., Thomas, K. V., Paull, B., Improved method for the determination of zinc pyrithione in environmental water samples incorporating on-line extraction and preconcentration coupled with liquid chromatography atmospheric pressure chemical ionisation mass spectrometry, *Journal of Chromatography A* 1132 (1-2) (2006) 157-164. <https://doi.org/10.1016/j.chroma.2006.07.068>.
- [19] Malik, A. K., Sharma, V., Sharma, V. K., Rao, A. L. J., Column Preconcentration and Spectrophotometric Determination of Ziram and Zineb in Commercial Samples and Foodstuffs Using (1,2'-Pyridylazo)-2-naphthol (PAN)-Naphthalene as Adsorbate, *Journal of Agricultural and Food Chemistry* 52 (26) (2004) 7763-7767. <https://doi.org/10.1021/jf040326h>.
- [20] Grunnet, K. S., Dahllof, I., Environmental fate of the antifouling compound zinc pyrithione in seawater, *Environmental Toxicology and Chemistry* 24 (12) (2005) 3001-3006. <https://doi.org/10.1897/04-627R.1>.
- [21] Bajia, S., Ojha, K. G., Synthesis, separation and determination of metal dithiocarbamates complexes by HPLC-ICP-MS, *Eurasian Journal of Analytical Chemistry* 8 (3) (2013) 107-111. <http://www.eurasianjournals.com/Synthesis-Separation-and-Determination-of-Metal-Dithiocarbamates-Complexes-by-HPLC,79714,0,2.html>.
- [22] Sakkas, V. A., Shibata, K., Yamaguchi, Y., Sugawara, S., Albanis, T., Aqueous phototransformation of zinc pyrithione: Degradation kinetics and byproduct identification by liquid chromatography-atmospheric pressure chemical ionisation mass spectrometry, *Journal of Chromatography A* 1144 (2) (2007) 175-182. <https://doi.org/10.1016/j.chroma.2007.01.049>.
- [23] Ahmadi, F., Rajabi, M., Faizi, F., Rahimi-Nasrabadi, M., Maddah, B., Magnetic solid-phase extraction of Zineb by C18-functionalised paramagnetic nanoparticles and determination by first-derivative spectrophotometry, *International Journal of Environmental Analytical Chemistry* 94 (11) (2014) 1123-1138. <https://doi.org/10.1080/03067319.2014.940339>.
- [24] Hashemi, F., Rastegarzadeh, S., Pourreza, N., A combination of dispersive liquid-liquid microextraction and surface plasmon resonance sensing of gold nanoparticles for the determination of ziram pesticide, *Journal of Separation Science* 41 (5) (2018) 1156-1163. <https://doi.org/10.1002/jssc.201700992>.
- [25] Thomas, K. V., Determination of the antifouling agent zinc pyrithione in water samples by copper chelate formation and high-performance liquid chromatography-atmospheric pressure chemical ionisation mass spectrometry, *Journal of Chromatography A* 833 (1) (1999) 105-109. [https://doi.org/10.1016/S0021-9673\(98\)01009-7](https://doi.org/10.1016/S0021-9673(98)01009-7).
- [26] Harino, H., Midorikawa, S., Arai, T., Ohji, M., Cu, N. D., Miyazaki, N., Concentrations of booster biocides in sediment and clams from Vietnam, *Journal of the Marine Biological Association of the United Kingdom* 86 (5) (2006) 1163-1170. <https://doi.org/10.1017/S0025315406014147>.
- [27] Kim, T. H., Jung, G. H., Lee, E. H., Park, H. R., Lee, J. K., Kim, H. G., Development and validation of liquid chromatography-tandem mass spectrometry method for simultaneous determination of zinc pyrithione and pyriproxyfen in shampoos, *Acta Chromatographica* 30 (3) (2018) 200-205. <https://doi.org/10.1556/1326.2017.00294>.
- [28] Lo, C.-C., Ho, M.-H., Hung, M.-D., Use of High-Performance Liquid Chromatographic and Atomic Absorption Methods To Distinguish Propineb, Zineb, Maneb, and Mancozeb Fungicides, *Journal of Agricultural and Food Chemistry* 44 (9) (1996) 2720-2723. <https://doi.org/10.1021/jf960008l>.
- [29] Kondoh, Y., Takano, S., Determination of zinc pyrithione in cosmetic products by high-performance liquid chromatography with pre-labelling, *Journal of Chromatography A* 408 (1987) 255-262. [https://doi.org/10.1016/S0021-9673\(01\)81808-2](https://doi.org/10.1016/S0021-9673(01)81808-2).
- [30] Agarwal, S., Aggarwal, S. G., Singh, P., Quantification of ziram and zineb residues in fog-water samples, *Talanta* 65 (1) (2005) 104-110. <https://doi.org/10.1016/j.talanta.2004.05.041>.
- [31] Kumar, P., Ahlawat, S., Chauhan, R., Kumar, A., Singh, R., Kumar, A., *In vitro* and field efficacy of fungicides against sheath blight of rice and post-harvest fungicide residue in soil, husk, and brown rice using gas chromatography-tandem mass spectrometry,

Environmental Monitoring and Assessment 190 (9) (2018) 503. <https://doi.org/10.1007/s10661-018-6897-7>.

[32] U.S. EPA, Method 6020B (SW-846): Inductively Coupled Plasma-Mass Spectrometry, Revision 2. Washington, 2014. <https://www.epa.gov/esam/epa-method-6020b-sw-846-inductively-coupled-plasma-mass-spectrometry>.

[33] Hu, Z., Hu, S., Gao, S., Liu, Y., Lin, S., Volatile organic solvent-induced signal enhancements in inductively coupled plasma-mass spectrometry: a case study of methanol and acetone, *Spectrochimica Acta Part B: Atomic Spectroscopy* 59 (9) (2004) 1463-1470. <https://doi.org/10.1016/j.sab.2004.07.007>.

[34] Currie, L. A., Nomenclature in evaluation of analytical methods including detection and quantification capabilities, *Pure and Applied Chemistry* 67 (10) (1995) 1699-1723. <https://doi.org/10.1351/pac199567101699>.

[35] Phenomenex, Sample preparation – made simple – selection and users guide, Phenomenex: Torrance, 2015. http://phx.phenomenex.com/lib/BR27941114_W.pdf.

[36] Nováková, L., Vlčková, H., A review of current trends and advances in modern bio-analytical methods: Chromatography and sample preparation, *Analytica Chimica Acta* 656 (1-2) (2009) 8-35. <https://doi.org/10.1016/j.aca.2009.10.004>.

[37] Hennion, M.-C., Solid-phase extraction: method development, sorbents, and coupling with liquid chromatography, *Journal of Chromatography A* 856 (1-2) (1999) 3-54. [https://doi.org/10.1016/S0021-9673\(99\)00832-8](https://doi.org/10.1016/S0021-9673(99)00832-8).

[38] Araújo, D., Machado, W., Weiss, D., Mulholland, D. S., Boaventura, G. R., Viers, J., Garnier, J., Dantas, E. L., Babinski, M., A critical examination of the possible application of zinc stable isotope ratios in bivalve mollusks and suspended particulate matter to trace zinc pollution in a tropical estuary, *Environmental Pollution* 226 (2017) 41-47. <https://doi.org/10.1016/j.envpol.2017.04.011>.

[39] Milazzo, A. D. D., Silva, A. C. M., Oliveira, D. A. F., Cruz, M. J. M., The influence of seasonality (dry and rainy) on the bioavailability and bioconcentration of metals in an estuarine zone, *Estuarine, Coastal and Shelf Science* 149 (2014) 143-150. <https://doi.org/10.1016/j.ecss.2014.08.013>.

[40] Vallet-Regí, M., Izquierdo-Barba, I., Colilla, M., Structure and functionalization of mesoporous

bioceramics for bone tissue regeneration and local drug delivery, *Philosophical Transactions of the Royal Society A: Mathematical, Physical and Engineering Sciences* 370 (1963) (2012) 1400-1421. <https://doi.org/10.1098/rsta.2011.0258>.

[41] Sigma-Aldrich Co., Guide to Solid Phase Extraction, *Bulletin* 910, 1998. <https://www.sigmaaldrich.com/Graphics/Supelco/objects/4600/4538.pdf>.

Synthesis, characterization, and thermal behavior of amidosulfonates of transition metals in air and nitrogen atmosphere

Jose Marques Luiz^{1†}, Ronaldo Spezia Nunes¹

1. São Paulo State University (Unesp), School of Engineering, Department of Chemistry and Energy, Guaratinguetá, São Paulo, Brazil

†Corresponding author: Jose Marques Luiz, Phone: +55 12 31232170, Email address: jose-marques.l Luiz@unesp.br

ARTICLE INFO

Article history:

Received: January 29, 2020

Accepted: May 11, 2020

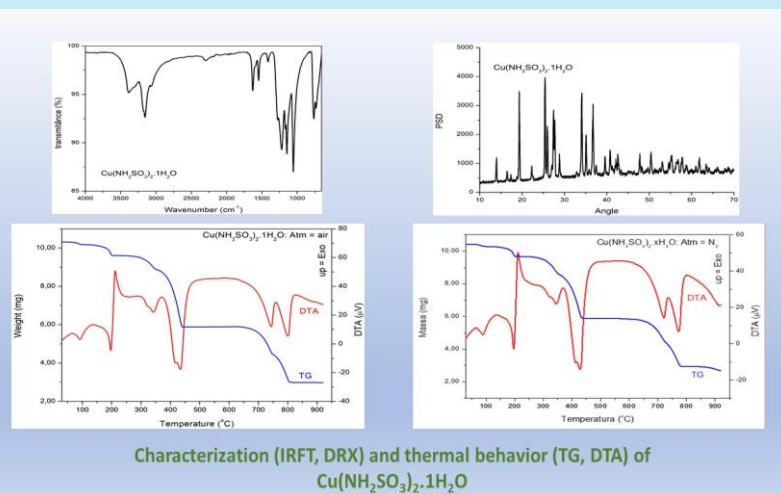
Published: October 01, 2020

Keywords:

1. sulfamic acid
2. thermal behavior
3. sulfamates
4. transition metals

ABSTRACT: The amidosulfonates of Mn^{2+} , Co^{2+} , Ni^{2+} , Cu^{2+} and Zn^{2+} were prepared by the direct reaction between the metal carbonate and the amidosulfonic acid with heating and stirring. The compounds were characterized by infrared absorption spectroscopy (IRFT), elemental analysis, thermal analysis (TG and DTA) and X-ray diffraction by the powder method. The absorptions observed in IR spectra are associated with N-H and O-H stretching, as well as symmetrical and asymmetric S-O stretching in the sulfonic group. The compounds present X-ray diffraction pattern with well-defined reflections, showing no evidence of isomorphism. The TG-DTA curves allowed to establish the stoichiometry of compounds as $M(NH_2SO_3)_2 \cdot xH_2O$, where $M = Mn^{2+}$, Co^{2+} , Ni^{2+} , Cu^{2+} and Zn^{2+} and x ranging from 1 to 4.

Dehydration leads to the formation of stable anhydrous. In all cases the respective sulfates are formed as an intermediate. After consecutive steps of decomposition, the respective oxides were obtained: Mn_3O_4 , CoO , NiO , CuO and ZnO . The TG-DTA curves are characteristic for each sample, with thermal events related to dehydration and ligand decomposition.



Characterization (IRFT, DRX) and thermal behavior (TG, DTA) of $Cu(NH_2SO_3)_2 \cdot 1H_2O$

1. Introduction

The amidosulfonic acid or sulfamic acid (NH_2SO_3H) has molar mass 97.10 g mol^{-1} . When dry it is stable, but in solution, it is easily hydrolyzed, forming ammonium bisulfate. It is relatively soluble in water, moderately soluble in alcohol, poorly soluble in acetone, insoluble in ether and very soluble in nitrogenous bases, liquid ammonia, pyridine, formamide and dimethylformamide. It is classified as a strong acid ($pH = 1.2$ in 1% aqueous solution and $25 \text{ }^\circ\text{C}$). It is used as standard in alkalimetry, in steel cleaning, in removal of nitrites and stabilization of chlorine in pool water. It is a toxic compound,

used as poison for rats. Handling requires careful care as it easily irritates the skin and mucous membrane. It forms orthorhombic crystals and has melting point near $205 \text{ }^\circ\text{C}$ ¹. In recent years sulfamic acid has been used as an efficient heterogeneous catalyst in a series of organic reactions, such as acetylation, esterification, condensation, transesterification, among others². It is a ZWITTERION, in other words, a dipolar ion having opposite charges on different atoms. In the formation of metal complexes, both amine and sulfonate groups participate in the coordination with the metal ion.

Few studies report the chemical and thermal properties of metal salts containing sulfonic acid derivatives, although the preparation of these salts

is easy to perform³⁻¹⁰. Maksin and Standritchuk³ studied the water solubility of Ni(II) and Co(II) sulfamates. Budurov *et al.*^{4,5} studied by DSC the phase transformations that occur in the heating of some amidosulfonates, determining the energy involved in the processes represented by endothermic peaks. Also, by DSC, Thege⁶ investigated the thermal behavior of (NH₄)₂SO₄, NH₄HSO₄ and NH₄NH₂SO₃. The crystalline structure and growth of Li[NH₂SO₃] monocrystals was studied by Stade, Held and Bohaty⁷, and it was possible to establish the spatial group, cell parameters and refractive index for the crystals obtained. The elastic properties of sulfamic acid and various sulfamates were studied by Haussül and Haussül and reported phase transformations⁸. Shimizau *et al.*⁹ determined the crystallographic properties of silver amidosulfonate and described a lamellar structure with potential chemical applications. Squattrito and coworkers studied the layered structures of metal salts of sulfonic acid derivatives¹⁰⁻¹². Jaishree *et al.*¹³ studied the optical and thermal properties of a monocrystal of amidosulfonic acid and reported the absorption bands in the infrared region. The main absorptions were attributed to the vibrational modes of the -SO₃⁻ and -NH₃⁺ group. Brahmaji *et al.* also identified the functional groups by FTIR and reported the changes observed in the pure crystals and doped with Tb³⁺¹⁴. Wickleder¹⁵ studied the synthesis, crystal structure, and thermal behavior of some rare earth amidosulfonates. Luiz, Nunes and Matos¹⁶ studied the thermal behavior of all the amidosulfonates of the rare earth series and observed a mass gain between 250 °C and 350 °C, attributed to an oxidative process SO₃²⁻ → SO₄²⁻, which is more evident in a lower heating rate. Brahmaji *et al.*¹⁴ also observed mass gain in this temperature range.

2. Materials and Methods

All chemicals used in this study were of analytical grade. Metallic chlorides were obtained from Sigma Aldrich, while the sodium hydrogen carbonate and silver nitrate were obtained from Merck and were used without further purification.

2.1 Metal Carbonates

Carbonates of Mn(II), Co(II), Ni(II), Cu(II) and Zn(II) were prepared by adding slowly, with

continuous stirring, a saturated sodium hydrogen carbonate solution to aqueous solutions metal chloride, until total precipitation of the metal ions. The precipitates were washed with distilled water until the elimination of chloride ions (qualitative test with AgNO₃/HNO₃ solution for chloride) and was placed in vacuum desiccator until constant mass.

2.2 Metal Amidosulfonates

The compounds were prepared by the direct reaction between the aqueous suspension of the metal carbonates (Mn, Co, Ni, Cu and Zn) and the amidosulfonic acid, with heating at 80 °C and stirring. The acid in powder form was slowly added until a small amount of the metal carbonate remained. The carbonate in excess was removed by filtration and the aqueous solution was evaporated slowly near to dryness. Subsequently, the solution was kept in vacuum desiccator until constant mass.

2.3 Characterization of samples

The infrared spectroscopy for amidosulfonic acid and its metal amidosulfonates were run on a Perkin-Elmer Spectrum 100 ATR FTIR spectrophotometer using ATR accessory with germanium crystal. The FTIR spectra were recorded with 16 scans per spectrum a resolution of 4 cm⁻¹.

The X-ray powder patterns were obtained by using a BRUKER System D8 Advance Diffractometer, employing CuK α radiation ($\lambda = 1.541 \text{ \AA}$), 25 mA, 40 kV, 10 rpm rotation, 0.02 step, 0.6 slit mm, time 0.3 s, in the range 2θ from 10 to 70 degrees. Elemental analysis for H, N and S was performed using a Leco CHNS Analyzer.

The thermal behavior was evaluated by thermogravimetry (TG) and differential thermal analysis (DTA) in the simultaneous module TG-DTA 6200 Extar 6000 from Seiko SII, with sample mass of the order of 3 to 10 mg, heating ratio $\beta = 20 \text{ }^\circ\text{C min}^{-1}$ (30 to 900 °C), alumina crucible, dynamic atmosphere of synthetic air and nitrogen, with flow of 100 mL min⁻¹. As reference for DTA, previously calcined alumina was used.

3. Results and discussion

The elemental analysis results are presented in [Tab. 1](#) and are in agreement with the proposed general formula $M(\text{NH}_2\text{SO}_3)_2 \cdot x\text{H}_2\text{O}$, where $M =$

Mn^{2+} , Co^{2+} , Ni^{2+} , Cu^{2+} and Zn^{2+} and x the number of water molecules ranging from 1 to 4, where $x = 4$ for Mn^{2+} , 3 for Co^{2+} and Zn^{2+} , 2 for Ni^{2+} and 1 for Cu^{2+} .

Table 1. Elemental analysis of the solid compounds.

Compound	% N		% H		% S	
	Calc.	EA	Calc.	EA	Calc.	EA
$\text{Mn}(\text{NH}_2\text{SO}_3)_2 \cdot 4\text{H}_2\text{O}$	8.78	8.77	3.80	3.79	20.10	20.08
$\text{Co}(\text{NH}_2\text{SO}_3)_2 \cdot 3\text{H}_2\text{O}$	9.18	9.31	3.30	3.54	20.01	21.30
$\text{Ni}(\text{NH}_2\text{SO}_3)_2 \cdot 2\text{H}_2\text{O}$	9.76	9.63	2.81	2.78	22.36	22.04
$\text{Cu}(\text{NH}_2\text{SO}_3)_2 \cdot 1\text{H}_2\text{O}$	10.24	10.20	2.21	2.21	23.43	23.35
$\text{Zn}(\text{NH}_2\text{SO}_3)_2 \cdot 3\text{H}_2\text{O}$	8.99	9.08	3.24	3.27	20.58	20.78

The main infrared absorption bands were associated with the N-H stretching, namely, a NH_3^+ broad band at $3400\text{--}3300\text{ cm}^{-1}$, the N-H stretching as a weak band at 2873 cm^{-1} and the absorptions observed at 1533 and 1433 cm^{-1} due to symmetric stretching mode of NH_3^+ while at 1567 cm^{-1} is due to asymmetric mode. The SO_3^- stretching vibration was observed in a 1065 cm^{-1} and at 685 cm^{-1} , the N-S stretching mode can be seen, all these absorptions agree with the literature⁴⁻¹⁴. The absence of that weak band of N-H stretching is an evidence that de coordination of the metal ions occurred by NH_3^+ group. Another fact is the increase observed in the wavenumber for the N-S stretching, suggesting that the N-S bond becomes strongest. The vibrational spectra in the infrared region of amidosulfonic acid and metal amidosulfonates are shown in the [Fig. 1](#).

The X-ray powder pattern of the metal amidosulfonates are shown in the [Fig. 2](#). The X-ray diffractograms indicate that the compounds were obtained with a certain crystallinity degree, showing no evidence of isomorphism. The compounds showed low relative intensity (I_0) reflections: Mn ($2\theta = 19.0$; $I_0 = 845$); Co ($2\theta = 19.3$; $I_0 = 3621$); Ni ($2\theta = 26.3$; $I_0 = 6534$); Cu ($2\theta = 25.4$; $I_0 = 4010$); Zn ($2\theta = 19.4$; $I_0 = 4146$).

By the TG/DTA curves it was possible to establish the stoichiometry of the compounds, such as: $\text{ML}_2 \cdot x\text{H}_2\text{O}$, where M represents the metallic ions $M = \text{Mn}^{2+}$, Co^{2+} , Ni^{2+} , Cu^{2+} and Zn^{2+} ; L represents the anion NH_2SO_3^- and x the number of water molecules ranging from 1 to 4, where $x = 4$ for Mn^{2+} , 3 for Co^{2+} and Zn^{2+} , 2 for Ni^{2+} and 1 for Cu^{2+} . In a synthetic air atmosphere, the events

associated with the thermal decomposition of the ligand occur at slightly lower temperatures than in a nitrogen atmosphere. [Tables 2](#) and [3](#) show the results extracted from the TG and DTA curves in the atmosphere of synthetic air and nitrogen. [Figures 3](#) and [4](#) show the TG and DTA curves in the atmosphere of synthetic air and nitrogen, respectively.

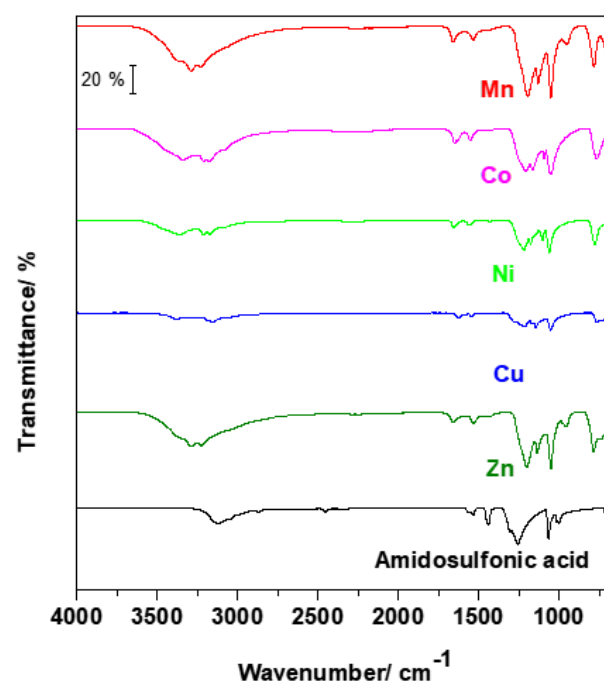


Figure 1. Vibrational spectra in the infrared region of amidosulfonic acid and metal amidosulfonates.

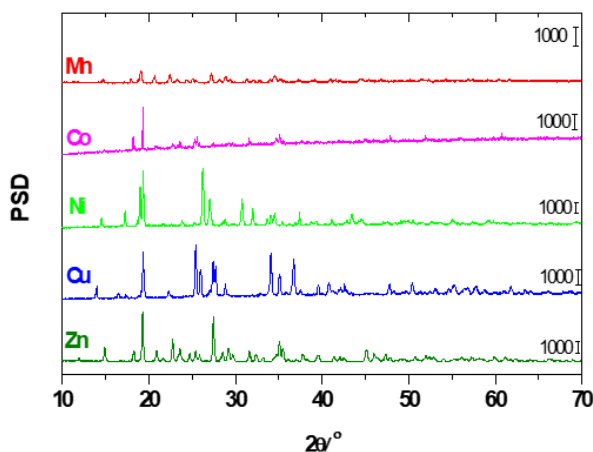


Figure 2. X-ray diffraction pattern of the metal amidosulfonates.

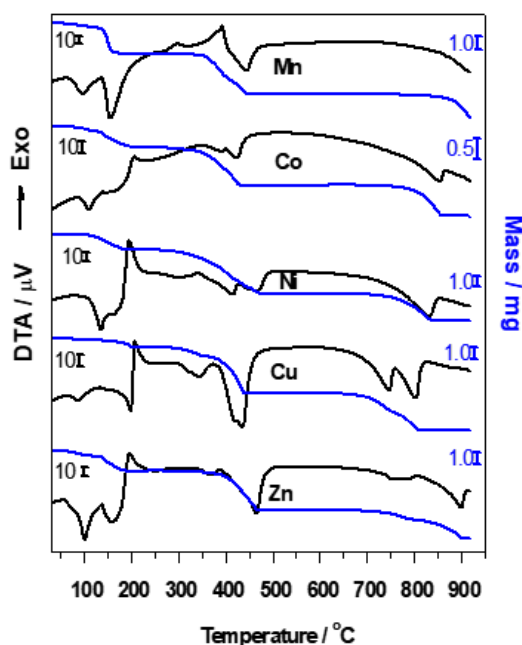


Figure 3. TG and DTA curves of the obtained compounds, in a synthetic air atmosphere. Sample mass: Mn = 9.680 mg, Co = 2.980 mg, Ni = 10.194 mg, Cu = 10.314 mg and Zn = 10.064 mg.

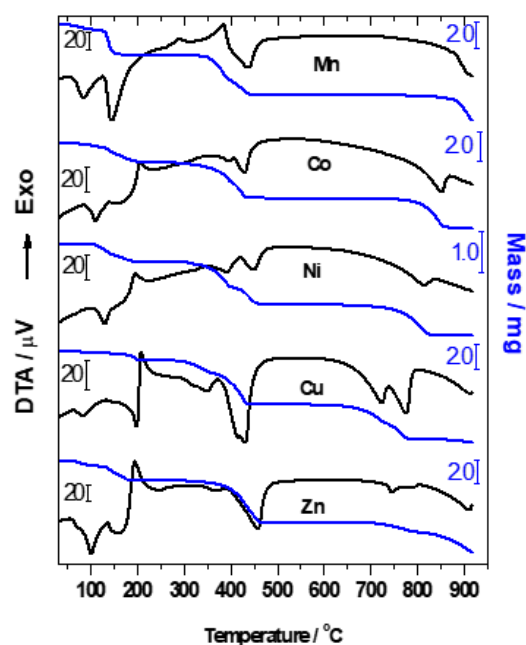


Figure 4. TG and DTA curves of the obtained compounds, in a nitrogen atmosphere. Sample mass: Mn = 10.383 mg, Co = 3,794 mg, Ni = 2,984 mg, Cu = 10.414 mg and Zn = 10.193 mg.

Table 2. Results extracted from the TG curves.

Samples	Molar mass / g mol ⁻¹		Metal / %		H ₂ O / %		Residue / %		
	Calc.	TG	Calc.	TG	Calc.	TG	Calc.	TG	Oxide
Mn(L) ₂ .4H ₂ O (air)	319.17	318.99	17.21	17.22	22.57	22.58	?	?	Mn ₃ O ₄
Mn(L) ₂ .4H ₂ O (N ₂)		319.90		17.17		22.75		?	
Co(L) ₂ .3H ₂ O (air)	305.14	301.35	19.31	19.56	17.71	16.67	24.56	24.86	CoO
Co(L) ₂ .3H ₂ O (N ₂)		300.79		19.59		16.52		24.91	
Ni(L) ₂ .2H ₂ O (air)	286.90	290.40	20.46	20.21	12.55	13.61	26.03	25.77	NiO
Ni(L) ₂ .2H ₂ O (N ₂)		291.72		20.11		14.00		25.60	
Cu(L) ₂ .1H ₂ O (air)	273.75	274.58	23.21	23.15	6.58	6.86	29.06	28.93	CuO
Cu(L) ₂ .1H ₂ O (N ₂)		274.81		23.13		6.94		28.95	
Zn(L) ₂ .3H ₂ O (air)	311.61	309.07	20.98	21.16	17.34	17.66	26.12	26.33	ZnO
Zn(L) ₂ .3H ₂ O (N ₂)		308.32		21.21		16.46		?	

Table 3. Results extracted from the DTA curves.

Samples	DTA Peak (Tp) / °C								
	<i>endo</i>	<i>endo</i>	<i>exo</i>	<i>exo</i>	<i>endo</i>	<i>endo</i>	<i>endo</i>	<i>endo</i>	<i>endo</i>
Mn(L ₂) ₂ .4H ₂ O (air)	89.59	148.4	289.0	387.2	439.4	671.3	874.0		
Mn(L ₂) ₂ .4H ₂ O (N ₂)	84.64	146.8	289.0	383.8	439.4	699.4	872.8		
Co(L ₂) ₂ .3H ₂ O (air)	112.4	156.5	210.5		392.0	426.4	854.8		
Co(L ₂) ₂ .3H ₂ O (N ₂)	110.8	164.8	209.0		400.2	432.9	853.2		
Ni(L ₂) ₂ .2H ₂ O (air)	133.9	164.2	203.0		303.4	411.3	462.0	824.1	
Ni(L ₂) ₂ .2H ₂ O (N ₂)	132.0		200.7		323.6	395.3	450.0	814.0	
Cu(L ₂) ₂ .1H ₂ O (air)	89.60	195.9	210.5		343.0	419.8	436.2	741.9	799.1
Cu(L ₂) ₂ .1H ₂ O (N ₂)	89.60	195.9	212.4		344.6	411.7	426.4	719.2	773.0
Zn(L ₂) ₂ .3H ₂ O (air)	97.10	162.1	203.0		364.2	457.4	804.2	900.0	
Zn(L ₂) ₂ .3H ₂ O (N ₂)	97.10	164.8	201.6		364.2	465.4	789.4	912.0	

3.1 Mn(NH₂SO₃)₂.4H₂O

Dehydration of the manganese (II) amidosulfonate occurs in two consecutive steps with the elimination of one and subsequently three water molecules, between 30 and 220 °C, with mass loss about 22 %. In this step two endothermic peaks are observed at 90 °C and 148 °C (synthetic air) at 85 °C and 147 °C (N₂). The anhydrous compound remains stable between 219 °C and 340 °C (synthetic air) and between 197 °C and 333 °C (N₂). Although no mass change was observed in this temperature range, there is an exothermic peak at 289 °C (synthetic air and N₂) which may be associated with a crystallization process. Brahmaji *et al.*¹⁴ also reported a gain mass in this range temperature, however this thermal event needs to be further investigated. Budurov *et al.*⁵ reported endothermic peaks attributed to phase transition at 177 °C (KNH₂SO₃) and 182 °C (NaNH₂SO₃). Haussühl and Haussühl⁸ also detected phase transformation in CsNH₂SO₃.

The thermal decomposition of the compounds occurs in two distinct steps. The first step begins with an exothermic (386 °C) process followed by another endotherm (439 °C) at both atmospheres. This stage leads to the formation of an intermediate, stable over a wide temperature range: 450 °C to 800 °C (synthetic air) and 443 °C and 820 °C (N₂). This intermediate is probably MnSO₄ (Calc. = 47.31 %, TG = 47.34 %), that begins to decompose with an endothermic event (850 °C) to produce the oxide. In the temperature range in which the experiments were performed (30 °C → 900 °C) the formation of the residual oxide could not be observed.

3.2 Co(NH₂SO₃)₂.3H₂O

The dehydration process of the cobalt (II) amidosulfonate occurs in a single step, with simultaneous elimination of three water molecules between 85 and 220 °C and loss of mass of 16.6%. In this stage two endothermic peak are observed around 112 °C and 157 °C (synthetic air) and 111 °C and 164 °C (N₂). After the anhydrous formation, an exothermic peak is observed around 210 °C, which may be associated with a crystallization process. The decomposition of the ligand occurs in two distinct stages: between 245 °C and 450 °C (synthetic air) and between 258 °C and 442 °C (N₂), both with formation of the CoSO₄ intermediate. In this step two endothermic DTA peaks are observed: 392 °C and 426 °C (synthetic air) and 400 °C and 433 °C (N₂). The CoSO₄ intermediate (Calc. = 50.80 %, TG = 51.80 %) remains stable over a wide temperature range: between 442 °C and 720 °C (synthetic air) and between 450 °C and 716 °C (N₂). The formation of the residue occurs at 861 °C, with mass loss of the order of 26 %, compatible with the formation of CoO, in both atmospheres.

3.3 Ni(NH₂SO₃)₂.2H₂O

The dehydration of the nickel (II) amidosulfonate occurs in a two overlapping steps, with elimination of two water molecules between 90 and 192 °C (synthetic air) between 100 °C and 206 °C (N₂) with mass loss of order of 13.5 %. At this stage, endothermic peaks are observed at 134 °C and 164 °C (synthetic air) and 132 °C (N₂). After the anhydrous formation, an intense exothermic peak is observed at 203 °C (synthetic

air) and 201 °C (N₂) of low intensity, which may be associated with a crystallization process. The decomposition of the ligand occurs in two distinct stages: between 251 °C and 479 °C (synthetic air) and between 294 °C and 461 °C (N₂), both with formation of the NiSO₄ intermediate. In this stage endothermic DTA peaks are observed at: 304 °C, 411 °C and 462 °C (synthetic air) and 324 °C, 395 °C and 450 °C (N₂). The NiSO₄ intermediate (Calc. = 53.94 %, TG = 53.30 %) remains stable over a wide temperature range: between 474 °C and 720 °C (synthetic air) and between 459 °C and 716 °C (N₂). The formation of the residue occurs at 831 °C (synthetic air and N₂) with loss mass in the order of 26 %, compatible with the formation of NiO, in both atmospheres.

3.4 *Cu(NH₂SO₃)₂·1H₂O*

The dehydration of the copper (II) amidosulfonate occurs in a two overlapping steps, eliminating one water molecule between 73 °C and 199 °C (synthetic air) and between 65 °C and 203 °C (N₂) with mass loss of 6.9 % in both atmospheres. At this stage, two endothermic peaks were observed at 89.6 °C and 196 °C in both atmospheres. After the anhydrous formation, an exothermic peak around 211 °C (synthetic air and N₂) of low intensity is observed, which may be associated with a crystallization process. The decomposition of the ligand occurs in two distinct stages: between 200 °C and 450 °C (synthetic air) and between 206 °C and 440 °C (N₂), both with formation of the CuSO₄ intermediate (Calc. = 58.31 %, TG = 58.13 %). In this stage endothermic DTA peaks are observed: 343 °C, 420 °C and 436 °C (synthetic air) and 345 °C, 412 °C and 426 °C (N₂). The CuSO₄ intermediate remains stable over a wide temperature range: between 444 °C and 694 °C (synthetic air) and between 440 °C and 618 °C (N₂). In this stage endothermic peaks are observed at 741 °C and 799 °C (synthetic air) and 718 °C and 773 °C (N₂). The formation of the residue supposed CuO occurs at 810 °C (synthetic air) and 780 °C (N₂). Under N₂ atmosphere a new stage of mass loss appears, which begins at 840 °C and probably ends at temperatures above 900 °C. The DTA profile of the beginning of this stage has endothermic characteristics, suggesting a Cu²⁺ → Cu⁺ reduction process.

3.5 *Zn(NH₂SO₃)₂·3H₂O*

Dehydration Zn(NH₂SO₃)₂·3H₂O occurs two overlapping steps, between 64 °C and 195 °C (synthetic air and N₂), equivalent to the consecutive release of one and two water molecules, respectively, with losses of the order of 17 %. Endothermic peaks are observed at 97 °C and 163 °C (synthetic air and N₂). After formation of the anhydrous compounds, an exothermic peak was observed around 202 °C (synthetic air and N₂). The anhydrous compound remains stable between 190 °C and 295 °C (synthetic air) and 196 °C and 322 °C (N₂). The decomposition of the ligand in synthetic air starts at 304 °C, with endothermic peaks at 364 °C and 457 °C (synthetic air) and 364 °C and 465 °C (N₂). This stage leads to the formation of intermediate ZnSO₄ (Calc. = 51.80 %, TG = 52.40 %), which remains stable over a wide temperature range of 467 °C to 688 °C (synthetic air) and 471 °C to 684 °C (N₂). In a synthetic air atmosphere, the decomposition to ZnO occurs from 690 °C and ends at 913 °C, presenting endothermic peaks at 804 °C and 900 °C. In nitrogen atmosphere, residual oxide formation is not completed until 920 °C and endothermic peaks are observed at 744 °C, 789 °C and 912 °C.

4. Conclusions

The main absorptions in the infrared: $\nu O-H$ (3600 - 2700 cm⁻¹) in the salts; $\nu N-H$ (3400-3300 cm⁻¹) in amidosulfonic acid; $\nu S-O$ (1260-1140 cm⁻¹) and $\nu as S-O$ (1040-1020 cm⁻¹) emphasize the differences between the spectra of the salts and of the amidosulfonic acid, evidence the bond to the metal suggesting that the coordination occurs by the sulphonic grouping.

The X-ray diffractograms indicate that the compounds were obtained with a certain crystallinity degree, showing no evidence of isomorphism. The compounds showed relatively low intensity reflections.

The thermoanalytical results (TG/DTA) allowed to establish the stoichiometry of the compounds as: ML₂·xH₂O, where M represents the metallic ions Mn²⁺, Co²⁺, Ni²⁺, Cu²⁺ and Zn²⁺; L represents the anion NH₂SO₃⁻; x represents the number of water molecules, where x = 4 for Mn²⁺, x = 3 for Co²⁺; and Zn²⁺, x = 2 for Ni²⁺ and x = 1 for Cu²⁺. No significant differences were observed

between the analysis carried out in synthetic air or nitrogen atmosphere, only the thermal decomposition of the ligand in synthetic air atmosphere occur at slightly lower temperatures than in a nitrogen atmosphere. For all compounds, the MSO_4 stable intermediate was observed, which later decomposes to the respective oxide, that is: Mn_3O_4 , CoO , NiO , CuO and ZnO . In some samples the residual oxide is produced at temperatures above 950°C .

Acknowledgments

This research was supported by resources supplied by the Faculdade de Engenharia de Guaratinguetá (UNESP). The authors thank Prof. Dr. Edson Cocchieri Botelho (DMT-FEG-UNESP) for TG-DTA measurements, Prof. Dr. Sergio Francisco dos Santos (DMT-FEG-UNESP) for X-ray diffractometry, Prof. Dr. Konstantin Georgiev Kostov (DFI-FEG-UNESP) for FTIR measurements.

References

- [1] Index, M., Centennial edition, Merck & Co. Inc. Rahway, 1989.
- [2] Kamal, A., Babu, K. S., Hussaini, S. M. A., Srikanth, P. S., Balakrishna, M., Alarifi, A., Sulfamic acid: an efficient and recyclable solid acid catalyst for the synthesis of 4,5-dihydropyrrolo[1,2-*a*]quinoxalines, *Tetrahedron Letters* 56 (31) (2015) 4619-4622. <https://doi.org/10.1016/j.tetlet.2015.06.006>.
- [3] Maksin, V. I., Standritchuk, O. Z., Solubility diagrams of the systems nickel sulfamate-water and cobalt sulfamate-water, *Russian Journal of Applied Chemistry* 80 (7) (2007) 1048-1054. <https://doi.org/10.1134/S1070427207070063>.
- [4] Budurov, S., Tzolova, G., Thermogravimetrische Untersuchung der thermischen Zersetzung von Amidosulfonaten einwertiger metalle, *Thermochimica Acta* 303 (1) (1997) 101-105. [https://doi.org/10.1016/S0040-6031\(97\)00256-6](https://doi.org/10.1016/S0040-6031(97)00256-6).
- [5] Budurov, S., Tzolova, G., Bohatý, L., New structural phase transitions in potassium and sodium amidosulfonates, *Thermochimica Acta* 307 (1) (1997) 91-96. [https://doi.org/10.1016/S0040-6031\(97\)00360-2](https://doi.org/10.1016/S0040-6031(97)00360-2).
- [6] Thege, I. K., DSC investigation of the thermal behaviour of $(\text{NH}_4)_2\text{SO}_4$, NH_4HSO_4 and $\text{NH}_4\text{NH}_2\text{SO}_3$, *Thermochimica Acta* 60 (2) (1983) 149-159. [https://doi.org/10.1016/0040-6031\(83\)80265-2](https://doi.org/10.1016/0040-6031(83)80265-2).
- [7] Stade, J., Held, P., Bohatý, L., Crystal Growth, Crystal Structure and Physical Properties of Lithium Sulfamate $\text{Li}[\text{NH}_2\text{SO}_3]$, *Crystal Research and Technology* 36 (4-5) (2001) 347-360. [https://doi.org/10.1002/1521-4079\(200106\)36:4/5%3C347::AID-CRAT347%3E3.0.CO;2-Q](https://doi.org/10.1002/1521-4079(200106)36:4/5%3C347::AID-CRAT347%3E3.0.CO;2-Q).
- [8] Haussühl, E., Haussühl, S., Elastic properties of sulfamic acid and sulfamates of Li, Na, K, Rb, Cs, Tl, NH_4 , $\text{C}(\text{NH}_2)_3$ and $(\text{CH}_3)_3\text{NCH}_2\text{COOH}$, *Zeitschrift Für Kristallografie* 210 (4) (1995) 269-275. <https://doi.org/10.1524/zkri.1995.210.4.269>.
- [9] Shimizau, G. K. H., Enright, G. D., Ratcliffe, C. I., Rego, G. S., Reid, J. L., Ripmeester, J. A., Silver Sulfonates: An Unexplored Class of Layered Solids, *Chemistry of Materials* 10 (11) (1998) 3282-3283. <https://doi.org/10.1021/cm980409b>.
- [10] Shubnell, A. J., Kosnic, E. J., Squattrito, P. J., Structures of layered metal sulfonate salts: trends in coordination behavior of alkali, alkaline earth and transition metals, *Inorganica Chimica Acta* 216 (1-2) (1994) 102-112. [https://doi.org/10.1016/0020-1693\(93\)03700-K](https://doi.org/10.1016/0020-1693(93)03700-K).
- [11] Gunderman, B. J., Squattrito, P. J., Synthesis and Structures of Potassium and Rubidium Arenesulfonates, *Journal Logo* 33 (13) (1994) 2924-2931. <https://doi.org/10.1021/ic00091a035>.
- [12] Kosnic, E. J., McClymont, E. L., Hodder, R. A., Squattrito, P. J., Synthesis and structures of layered metal sulfonate salts, *Inorganica Chimica Acta* 201 (2) (1992) 143-151. [https://doi.org/10.1016/S0020-1693\(00\)85325-6](https://doi.org/10.1016/S0020-1693(00)85325-6).
- [13] Jaishree, D., Kanchana, G., Kesavasamy, R., Investigations on Growth, Optical and Thermal Properties of Sulphamic Acid Single Crystals, Investigations on Growth, Optical and Thermal Properties of Sulphamic Acid Single Crystals 2014 (2014) 950467. <https://doi.org/10.1155/2014/950467>.
- [14] Brahmaji, B., Rajyalakshmi, S., Rao, T. K. V., Valluru S. R., Basha, S. K. E., Satyakamal, C., Veeraiyah, V., Rao, K. R., Tb^{3+} added sulfamic acid single crystals with optimal photoluminescence properties for opto-electric devices, *Journal of Science: Advanced Materials and Devices* 3 (1) (2018) 68-76. <https://doi.org/10.1016/j.jsamd.2017.12.002>.
- [15] Wickleder, M. S., Syntheses, crystal structures, and thermal behavior of the rare earth amidosulfates

$M(\text{NH}_2\text{SO}_3)_3 \cdot 2\text{H}_2\text{O}$ (M=Pr, Nd, Sm), *Journal of Alloys and Compounds* 303-304 (2000) 445-453. [https://doi.org/10.1016/S0925-8388\(00\)00624-1](https://doi.org/10.1016/S0925-8388(00)00624-1).

[16] Luiz, J. M., Nunes, R. S., Matos, J. R., Síntese, caracterização e comportamento térmico de amidossulfonatos de terras raras, *Química Nova* 36 (3) (2013) 426-430. <https://doi.org/10.1590/S0100-40422013000300013>.

Approximate solutions of the Schrödinger equation with energy-dependent screened Coulomb potential in D – dimensions

Uduakobong Sunday Okorie^{1,3+}, Akpan Ndem Ikot^{2,3}, Precious Ogbonda Amadi³, Alalibo Thompson Nngiangia³, Etebong Emmanuel Ibekwe^{1,3}

1. Department of Physics, Akwa Ibom State University, Ikot Akpaden P. M. B. 1167, Uyo, Nigeria

2. Department of Physics, University of South Africa, Florida 1710, Johannesburg, South Africa

3. Theoretical Physics Group, Department of Physics, University of Port Harcourt, P. M. B. 5323 Choba, Nigeria

*Corresponding author: Uduakobong Sunday Okorie, Phone: +2347081545195 Email address: uduakobongokorie@aksu.edu.ng

ARTICLE INFO

Article history:

Received: October 26, 2019

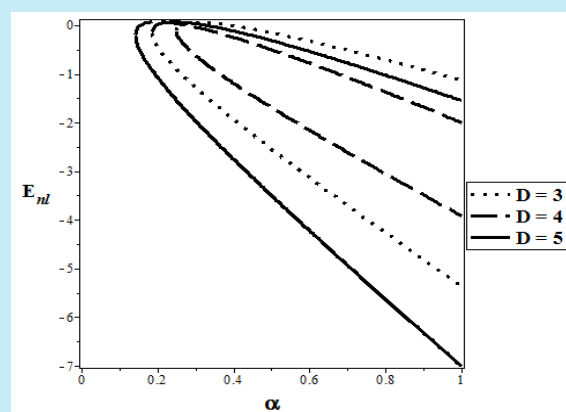
Accepted: April 07, 2020

Published: October 01, 2020

Keywords:

1. Schrödinger equation
2. energy-dependent screened Coulomb Potential
3. Nikiforov-Uvarov method
4. Greene-Aldrich approximation scheme

ABSTRACT: Within the framework of the conventional Nikiforov-Uvarov method and a new form of Greene-Aldrich approximation scheme, we solved the Schrödinger equation with the energy-dependent screened Coulomb potential. Energy eigenvalues and energy eigenfunctions were obtained both approximately and numerically at different dimensions. The energy variations with different potential parameters, quantum numbers and energy slope parameter, respectively were also discussed graphically. The major finding of this research is the effect of the energy slope parameter on the energy spectra, which is seen in the existence of two simultaneous energy values for a particular quantum state. Our special cases also agree with the results obtained from literature, when the energy slope parameter is zero.



1. Introduction

Quantum mechanics came into existence many decades ago to salvage the failure of classical mechanics, not being able to explain some of the physical phenomena such as Compton effects, specific heat capacity, blackbody radiation. From this point of view, many theoretical physicists have been investigating the exact and approximate solutions of the Schrödinger equation for some potentials of physical interests^{1,2}. The solutions of the Schrödinger equation play a vital role in many branches of modern physics and chemistry³. This is because it contains all the necessary information needed for the full description of a quantum state such as the probability density and entropy of the system⁴.

The Schrödinger equation with many physical potentials model have been investigated in recent times with different analytical methods such as Nikiforov-Uvarov (NU) method⁵⁻⁸, asymptotic iteration method (AIM)⁹⁻¹⁴, supersymmetric quantum mechanics(SUSYQM)¹⁵⁻¹⁸ among others¹⁹⁻²². One of such potential models is the screened Coulomb potential, which is given by Eq. 1²³.

$$V(r) = -\frac{Ae^{-\alpha r}}{r} \quad (1)$$

The screened Coulomb potential, also known as the Yukawa potential is greatly important, with applications cutting across nuclear Physics and Condensed-matter Physics²³. Here, its usage is involved in short-ranged interactions²⁴⁻²⁶. The screened-Coulomb potential is known to be the

potential of a charged particle in a weakly non-ideal plasma. It also describes the charged particle effects in a sea of conduction electrons in solid-state physics²⁷.

An approximate solution of the Schrödinger equation interacting with an inversely quadratic Yukawa potential has been obtained using SUSYQM¹⁵, where the screened Coulomb potential was obtained as a special case by varying the potential strength. Also, an approximate analytical solution of the radial Schrödinger equation for the screened Coulomb potential has been obtained, with energy eigenvalues and its corresponding eigenfunctions computed in closed forms²⁸.

Several researchers have also devoted great attention to investigate the quantum systems of the energy dependence of different potentials²⁹⁻³¹. Hassanabadi *et al.*^{32,33} studied the exact solutions of D-dimensional Schrödinger and Klein-Gordon equations using the Nikiforov-Uvarov method. Also, Lombard *et al.*³⁴ investigated the wave equation energy-dependent potential for confined systems. Numerous applications of the energy-dependent potential of wave equations have been seen in the spectrum of confined systems and heavy quark confinement in nuclear and molecular physics^{35,36}. Recently, Budaca³⁷ studied an energy-dependent Coulomb-like potential within the framework of Bohr Hamiltonian. The author further reported that the energy dependence on the coupling constant of the potential drastically changes the analytical properties of wave function and the corresponding eigenvalues of the system. Also, Boumali and Labidi³⁸ investigated the Shannon and Fisher information

in the Klein-Gordon equation with energy-dependent potential.

In this research, we seek to investigate the influence of the energy-dependent screened Coulomb potential defined as in Eq. 2,

$$V(r, E_{n\ell}) = -\frac{A(1+gE_{n\ell})e^{-\alpha r}}{r} \quad (2)$$

where g is the energy slope parameter, A is the depth of the potential, and α is the range of the potential. The effects of the energy dependence on the screened Coulomb potential have not been considered before in any literature, to the best of our knowledge. It can be deduced that when $g = 0$, the potential of Eq. 2 reduces to the Screened Coulomb potential. When $g = 0$ as $\alpha \rightarrow 0$, the potential of Eq. 2 reduces to the Coulomb potential. Using the conventional NU method, we will derive the ℓ -wave bound state solutions and their eigenfunctions of the Schrödinger equation for the energy-dependent screened Coulomb potential, both analytically and numerically. Special cases are also considered and our results are compared with existing literature for confirmation sake.

The organization of this work is as follows: In section 2, we determine the eigensolutions of the energy-dependent screened Coulomb potential by employing a new form of Greene-Aldrich approximation scheme and Nikiforov-Uvarov method. Section 3 is devoted to discuss the results obtained and compare to results in relevant literature. The conclusion of the work is presented in section 4.

2. Bound state solution of the energy-dependent screened Coulomb potential

The radial part of the Schrödinger equation in D-dimension³⁹ is given by Eq. 3.

$$\psi''(r) + \frac{2\mu}{\hbar^2}(E_{n\ell} - V(r))\psi(r) + \frac{1}{r^2} \left[\frac{(D-1)(D-3)}{4} + \ell(\ell + D - 2) \right] \psi(r) = 0 \quad (3)$$

where μ is the reduced mass, $E_{n\ell}$ is the non-relativistic energy eigenvalues to be determined. Substituting Eq. 2 into Eq. 3 gives Eq. 4.

$$\psi''(r) + \frac{2\mu}{\hbar^2} \left(E_{n\ell} + \frac{A(1+gE_{n\ell})e^{-\alpha r}}{r} \right) \psi(r) + \frac{1}{r^2} \left[\frac{(D-1)(D-3)}{4} + \ell(\ell + D - 2) \right] \psi(r) = 0 \quad (4)$$

In solving Eq. 4, we invoke a new form of Greene-Aldrich approximation scheme²³ to deal with the centrifugal term since $\ell \neq 0$. The approximations schemes are given by Eq. 5 and 6.

$$f_1(r) = \frac{1}{r^2} \approx \frac{4\alpha^2 e^{-2\alpha r}}{(1-e^{-2\alpha r})^2} = f_2(r) \quad (5)$$

$$\frac{1}{r^2} \approx \frac{4\alpha^2 e^{-2\alpha r}}{(1-e^{-2\alpha r})^2} + \frac{\alpha^2}{3} = f_3(r) \quad (6)$$

The plots explaining the rationality and validity of the above Eq. 5 and 6 and their expansions are given in Fig. 1(a–d). Figure 1a shows the plots of $f_1(r)$, $f_2(r)$ and $f_3(r)$ as they vary with r , when the screening parameter α is taken to be 0.5. In addition, we employ $\frac{1}{r}$ from $f_1(r)$ as given in Eq. 7.

$$f_4(r) = \frac{1}{r} \approx \frac{2\alpha e^{-\alpha r}}{1-e^{-2\alpha r}} \equiv f_5(r) \quad (7)$$

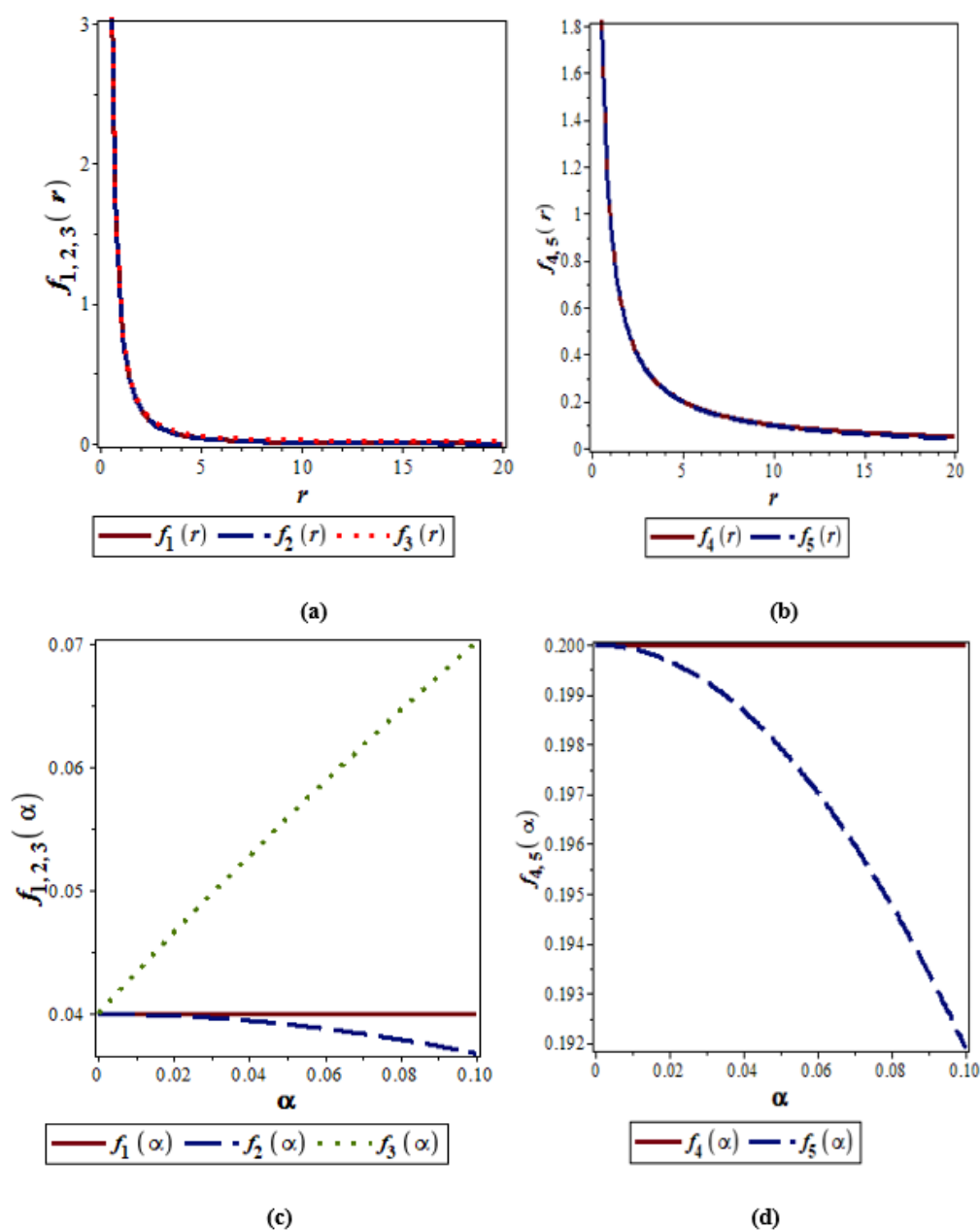


Figure 1. The plots of expressions (a) $f_1(r)$, $f_2(r)$, $f_3(r)$ as functions of r with $\alpha = 0.5$; (b) $f_4(r)$, $f_5(r)$ as functions of r with $\alpha = 0.5$; (c) $f_1(\alpha)$, $f_2(\alpha)$, $f_3(\alpha)$ as functions of α with $r = 5$; (d) $f_4(\alpha)$, $f_5(\alpha)$ as functions of α with $r = 5\text{nm}$.

Here, we have ignored the second expansion term $\frac{\alpha(1-e^{-2\alpha r})}{(12e^{-\alpha r})}$ when expanding Eq. 6. Furthermore, the rationality and validity of this expansion is given in Fig. 1b, with $\alpha = 0.5$. Considering the plots of the above expressions as functions of the screening parameter α as shown in Figs. 1c and 1d, we observe that the approximation $f_3(\alpha)$ corresponds to that of $f_1(\alpha)$ when $\alpha \leq 0.05$. As such, we see that the approximation $f_3(\alpha)$ is better than that of $f_2(\alpha)$.

With the above approximation schemes, Eq. 4 becomes Eq. 8.

$$\psi''(r) + \left[\frac{2\mu E_{nl}}{\hbar^2} + \frac{4\mu A(1+gE_{nl})e^{-2\alpha r}}{\hbar^2(1-e^{-2\alpha r})} - \frac{4\alpha^2 \gamma e^{-2\alpha r}}{\hbar^2(1-e^{-2\alpha r})^2} - \frac{\gamma\alpha^2}{3} \right] \psi(r) = 0 \quad (8)$$

where γ is given by Eq. 9.

$$\gamma = \left[\frac{(D-1)(D-3)}{4} + \ell(\ell + D - 2) \right] \quad (9)$$

By using the coordinate transformation of Eq. 10.

$$z = e^{-2\alpha r} \quad (10)$$

Eq. 8 becomes the differential equation of the form given in Eq. 11.

$$\psi''(z) + \frac{(1-z)}{z(1-z)} \psi'(z) + \frac{1}{z^2(1-z)^2} [-(\varepsilon^2 + \beta^2)z^2 + (2\varepsilon^2 + \beta^2 - \gamma)z - \varepsilon^2] \psi(z) = 0 \quad (11)$$

where ε^2 is given by Eq. 12.

$$\varepsilon^2 = -\left(\frac{\mu E_{nl}}{2\hbar^2 \alpha^2} - \frac{\gamma}{12} \right); \beta^2 = \frac{\mu A(1+gE_{nl})}{\hbar^2 \alpha} \quad (12)$$

By comparing Eq. 11 and Eq. A1 (see Appendix), we have the following parameters, Eq. 13:

$$\begin{aligned} \tilde{\tau}(z) &= 1 - z \\ \sigma(z) &= z(1 - z) \\ \tilde{\sigma}(z) &= -(\varepsilon^2 + \beta^2)z^2 + (2\varepsilon^2 + \beta^2 - \gamma)z - \varepsilon^2 \end{aligned} \quad (13)$$

Substituting Eq. 13 into Eq. A8 (see Appendix), we get $\pi(z)$, Eq. 14:

$$\pi(z) = -\frac{z}{2} \pm \sqrt{(a-k)z^2 + (k+b)z + c} \quad (14)$$

where a , b and c are given by Eq. 15.

$$\begin{aligned} a &= \frac{1}{4} + \varepsilon^2 + \beta^2 \\ b &= \gamma - 2\varepsilon^2 - \beta^2 \\ c &= \varepsilon^2 \end{aligned} \quad (15)$$

We can obtain the constant k , by expressing the discriminant under the square root of Eq. 14 to be equal to zero. As such, we have Eq. 16

$$k_{\pm} = -(\gamma - \beta^2) \pm 2\sqrt{\varepsilon^2} \sqrt{\left(\frac{1}{4} + \gamma\right)} \quad (16)$$

Substituting Eq. 16 into Eq. 14 yields Eq. 17:

$$\pi(z) = -\frac{z}{2} \pm \begin{cases} \left(\sqrt{\varepsilon^2} - \sqrt{\frac{1}{4} + \gamma}\right)z - \sqrt{\varepsilon^2}; \text{ for } k_+ = -(\gamma - \beta^2) + 2\sqrt{\varepsilon^2} \sqrt{\left(\frac{1}{4} + \gamma\right)} \\ \left(\sqrt{\varepsilon^2} - \sqrt{\frac{1}{4} + \gamma}\right)z + \sqrt{\varepsilon^2}; \text{ for } k_- = -(\gamma - \beta^2) - 2\sqrt{\varepsilon^2} \sqrt{\left(\frac{1}{4} + \gamma\right)} \end{cases} \quad (17)$$

According to NU method⁴⁰, we choose the expression $\pi(z)_-$ which the function $\tau(z)$ has a negative derivative. This is given by Eq. 18

$$\pi(z)_- = -\left(\frac{1}{2} + \sqrt{\varepsilon^2} + \sqrt{\frac{1}{4} + \gamma}\right)z - \sqrt{\varepsilon^2} \quad (18)$$

with $\tau(z)$ being obtained with Eq. 19.

$$\tau(z) = 1 - 2\sqrt{\varepsilon^2} - 2\left(1 + 2\sqrt{\varepsilon^2} + \sqrt{\frac{1}{4} + \gamma}\right)z \quad (19)$$

By recalling Eq. A9 (see Appendix), we define the constant λ (Eq. 20) as

$$\lambda = -(\gamma - \beta^2) - 2\sqrt{\varepsilon^2} \sqrt{\frac{1}{4} + \gamma} - \left(\frac{1}{2} + \sqrt{\varepsilon^2} + \sqrt{\frac{1}{4} + \gamma}\right) \quad (20)$$

Substituting Eq. 20 into Eq. A10 (see Appendix) and carrying out algebraic simplifications, where $\tau'(z)$ is given by Eq. 21

$$\tau'(z) = -2\left(1 + \sqrt{\varepsilon^2} + \sqrt{\frac{1}{4} + \gamma}\right) \quad (21)$$

and $\sigma''(z)$, Eq. 22

$$\sigma''(z) = -2 \quad (22)$$

we obtain Eq. 23

$$\varepsilon^2 = \frac{1}{4} \left[\frac{(n+\chi)^2 - \beta^2}{(n+\chi)} \right]^2 \quad (23)$$

where χ is given by Eq. 24

$$\chi = \frac{1}{2} (1 + \sqrt{1 + 4\gamma}) \quad (24)$$

Substituting Eq. 12 into Eq. 23 yields a complicated transcendental energy eigenvalue equation of the energy dependent screened Coulomb potential in D-dimensions as (Eq. 25):

$$\left[(n + \chi) - \frac{\mu A(1 + gE_{nl})}{\hbar^2 \alpha (n + \chi)} \right]^2 + \frac{2\mu E_{nl}}{\hbar^2 \alpha^2} - \frac{\gamma}{3} = 0 \quad (25)$$

Eq. 25 can also be expressed by Eq. 26.

$$E_{n\ell} = \frac{-\hbar^2\alpha^2}{2\mu} \left[\left((n + \chi) - \frac{\mu A(1+gE_{n\ell})}{\hbar^2\alpha(n+\chi)} \right)^2 - \frac{\gamma}{3} \right] \quad (26)$$

where γ and χ are given in Eqs. 9 and 24, respectively.

To obtain the special case, we first rewrite Eq. 26 to the form of Eq. 27:

$$E_{n\ell} = \frac{-\hbar^2}{2\mu} \left[\left(\alpha(n + \chi) - \frac{\mu A(1+gE_{n\ell})}{\hbar^2(n+\chi)} \right)^2 - \frac{\alpha^2\gamma}{3} \right] \quad (27)$$

As $\alpha \rightarrow 0$ and $g \rightarrow 0$, Eq. 2 reduces to the standard Coulomb potential of the form of Eq. 28.

$$V(r) = -\frac{A}{r} \quad (28)$$

Setting the parameters $D = 3$ as $\alpha \rightarrow 0$ and $g \rightarrow 0$, we obtain the energy eigenvalue equation (Eq. 29):

$$E_{n\ell} = -\frac{\mu A^2}{2\hbar^2(n+\ell+1)^2} \quad (29)$$

This result is very consistent with the result obtained in Eq. 101 of Birkdemir *et al.*⁴¹. Also, taking the natural units ($\hbar^2 = \mu = 1$) and setting $D = 3$ and $g = 0$, the energy eigenvalue expression of Eq. 26 can be reduced to Eq. 30.

$$E_{n\ell} = \frac{-\alpha^2}{2} \left[\left((n + \ell + 1) - \frac{A}{\alpha(n+\ell+1)} \right)^2 - \frac{\ell(\ell+1)}{3} \right] \quad (30)$$

The result of Eq. 30 is consistent with the result obtained in Eq. 18 of Dong *et al.*²³.

To obtain the corresponding wave functions, we substitute $\pi(z)$ and $\sigma(z)$ from Eqs. 18 and 13, respectively into Eq. A4 (see Appendix) and solve the first-order differential equation. This gives Eq. 31.

$$\Phi(z) = z^{\sqrt{\varepsilon^2}} (1-z)^{\frac{1}{2} + \sqrt{\frac{1}{4} + \gamma}} \quad (31)$$

The weight function $\rho(z)$ from Eq. A6 (see Appendix) can be obtained Eq. 32

$$\rho(z) = z^{2\sqrt{\varepsilon^2}} (1-z)^{2\sqrt{\frac{1}{4} + \gamma}} \quad (32)$$

From the Rodrigues relation of Eq. A5 (see Appendix), we obtain Eq. 33 and Eq. 34.

$$y_n(z) = B_n z^{-2\sqrt{\varepsilon^2}} (1-z)^{-2\sqrt{\frac{1}{4} + \gamma}} \frac{d^n}{dz^n} \left[z^{n+2\sqrt{\varepsilon^2}} (1-z)^{n+2\sqrt{\frac{1}{4} + \gamma}} \right] \quad (33)$$

$$y_n(z) \equiv B_n P_n^{(2\sqrt{\varepsilon^2}, 2\sqrt{\frac{1}{4} + \gamma})} (1-2z) \quad (34)$$

where $P_n^{(\theta, \vartheta)}$ is the Jacobi Polynomial.

Substituting $\Phi(z)$ and $y_n(z)$ from Eqs. 31 and 34, respectively into Eq. A2 (see Appendix), we obtain Eq. 35:

$$\psi(z) = B_n z^{\sqrt{\varepsilon^2}} (1-z)^G P_n^{(2\sqrt{\varepsilon^2}, 2G-1)}(1-2z) \quad (35)$$

where G is given by Eq. 36.

$$G = \frac{1}{2} + \sqrt{\frac{1}{4} + \gamma} \quad (36)$$

From the definition of the Jacobi Polynomials⁴² results Eq. 37.

$$P_n^{(\theta, \vartheta)}(\omega) = \frac{\Gamma(n+\theta+1)}{n!\Gamma(\theta+1)} {}_2F_1\left(-n, \theta + \vartheta + n + 1, \theta + 1; \frac{1-\omega}{2}\right) \quad (37)$$

In terms of hypergeometric Polynomials, Eq. 35 can be written as Eq. 38.

$$\psi(z) = B_n z^{\sqrt{\varepsilon^2}} (1-z)^G \frac{\Gamma(n+2\sqrt{\varepsilon^2}+1)}{n!\Gamma(2\sqrt{\varepsilon^2}+1)} {}_2F_1\left(-n, 2\sqrt{\varepsilon^2} + 2G + n, 2\sqrt{\varepsilon^2} + 1; z\right). \quad (38)$$

3. Results and Discussion

In this study, the energy eigenvalues for the energy-dependent screened Coulomb potential as they vary with the screening parameter were computed for different quantum states as shown in Tab. 1. The existence of the energy slope parameter in Eq. 26 results in two different energy spectra for a particular quantum state and a specific screening parameter. The screening parameter varies in an inverse version with the duo energy spectra. The energy eigenvalues for the energy-dependent screened Coulomb potential as a function of screening parameters in higher dimensions were also computed, as shown in Tabs. 2 and 3, respectively. By employing Eq. 30, we have also computed the energy eigenvalues in three dimensions and in the absence of the energy slope parameter, as shown in Tab. 4. For the two different potential depths considered, we obtained the bound state energy eigenvalues for different quantum states of $2p-4f$, as they vary with different screening parameters. It can be seen that the energy eigenvalues for the different potential

depths decrease as the screening parameter increases, at each quantum state. Our analytical result of Eq. 30 and its corresponding numerical results of Tab. 4 are very consistent with the results obtained by Dong *et al.*²³. We have also computed the energy eigenvalues of Eq. 26 for higher dimensions, as shown in Tabs. 5 and 6, respectively. The level of effects imposed by the potential parameters of Eq. 2 on the energy eigenvalues of Eq. 26 are shown in Figs. 2-7. For different dimensions, the energy slope parameter causes an interwoven interaction of the curves, as compared to the situation when the energy slope parameter is zero. Figs. 8 and 9 show the variation of energy eigenvalues for the energy-dependent screened Coulomb potential with the different quantum numbers, for different values energy slope parameter considered. The trend of the relationship shows that the energy eigenvalues decrease as the quantum numbers increase. In Fig. 10, we also plotted the variation of the energy eigenvalues with the energy slope parameter for different dimensions.

Table 1. Eigenvalues ($E_{n\ell}$) for the energy-dependent screened Coulomb potential as a function of the parameter α for $2p-4f$ states, with $D = 3$.

States	α	$E_{n\ell}(g = -1, A = 2)$	$E_{n\ell}(g = 1, A = 2)$
2p	0.025	-0.05000000000, -0.9484636700	-0.2469390303, -3.653060970
	0.050	-0.10000000000, -0.8934950102	-0.2261820091, -3.573817991
	0.075	-0.14999999989, -0.8344159637	-0.2056916349, -3.494308363

Continue...

3p	0.025	-0.3282430205, -2.396756978	-0.1279838429, -6.147016156
	0.050	-0.2185168124, -2.731483190	-0.1003205303, -5.949679472
	0.075	-0.1419248550, -3.033075144	-0.07486233817, -5.750137661
3d	0.025	-0.3273369696, -2.397663029	-0.1276723472, -6.147327652
	0.050	-0.2155358280, -2.734464174	-0.09903861948, -5.950961383
	0.075	-0.1360998141, -3.038900185	-0.07189047036, -5.753109529
4p	0.025	-0.1013443775, -6.298655622	-0.06696010299, -9.533039897
	0.050	-0.05236401820, -6.747635982	-0.03856747648, -9.161432524
	0.075	-0.02019553609, -7.179804460	-0.01650824116, -8.783491756
4d	0.025	-0.1008065565, -6.299193443	-0.06660798158, -9.533392018
	0.050	-0.05037315511, -6.749626845	-0.03710618138, -9.162893819
	0.075	-0.01600781253, -7.183992184	-0.01308764621, -8.786912351
4f	0.025	-0.1000000000, -6.300000000	-0.06607984858, -9.533920151
	0.050	-0.04738907715, -6.752610923	-0.03491511579, -9.165084884
	0.075	-0.009735385820, -7.190264611	-0.007961748818, -8.792038248

Table 2. Eigenvalues ($E_{n\ell}$) for the energy-dependent screened Coulomb potential as a function of the parameter α for $2p-4f$ states, with $D = 4$.

States	α	$E_{n\ell}(g = -1, A = 2)$	$E_{n\ell}(g = 1, A = 2)$
2p	0.025	-0.6406250000, -0.6619912551	-0.1771068474, -4.791643153
	0.050	-0.7187500000, -0.4363825014	-0.1516973143, -4.660802686
	0.075	-0.5523050676, -1.041444930	-0.1269955847, -4.529254413
3p	0.025	-0.1676529658, -4.263597033	-0.09251657939, -7.726233419
	0.050	-0.1017568786, -4.635743120	-0.06332496524, -7.449175033
	0.075	-0.05426252476, -4.989487474	-0.03776841503, -7.168481584
3d	0.025	-0.1668742692, -4.264375729	-0.09209870569, -7.726651293
	0.050	-0.09894423101, -4.638555767	-0.06159768496, -7.450902314
	0.075	-0.04845181230, -4.995298186	-0.03374430925, -7.172505689
4p	0.025	-0.06465429287, -8.566595705	-0.04786732380, -11.57088267
	0.050	-0.02501719398, -9.112482806	-0.02055263540, -11.09194736
	0.075	-0.002313419520, -9.641436577	-0.002103392985, -10.60414660
4d	0.025	-0.06403407537, -8.567215922	-0.04740969809, -11.57134030
	0.050	-0.02269659485, -9.114803405	-0.01864771539, -11.09385228
	0.075	0.002607849543, -9.646357846	0.002371302471, -10.60862130
4f	0.025	-0.06316592284, -8.568084075	-0.04676908315, -11.57198091
	0.050	-0.01944974474, -9.118050255	-0.01598192774, -11.09651807
	0.075	-0.009489204657, -9.653239201	-0.008629543278, -10.61487954

Table 3. Eigenvalues ($E_{n\ell}$) for the energy-dependent screened Coulomb potential as a function of the parameter α for $2p-4f$ states, with $D = 5$.

States	α	$E_{n\ell}(g = -1, A = 2)$	$E_{n\ell}(g = 1, A = 2)$
2p	0.025	-0.3273369696, -2.397663029	-0.1276723472, -6.147327652
	0.050	-0.2155358280, -2.734464174	-0.09903861948, -5.950961383
	0.075	-0.1360998141, -3.038900185	-0.07189047036, -5.753109529
3p	0.025	-0.1008065565, -6.299193443	-0.06660798158, -9.533392018
	0.050	-0.05037315511, -6.749626845	-0.03710618138, -9.162893819
	0.075	-0.01600781253, -7.183992184	-0.01308764621, -8.786912351
3d	0.025	-0.1000000000, -6.300000000	-0.06607984858, -9.533920151
	0.050	-0.04738907715, -6.752610923	-0.03491511579, -9.165084884
	0.075	-0.009735385820, -7.190264611	-0.007961748818, -8.792038248
4p	0.025	-0.4194183076, -11.08305817	-0.03358353903, -13.84141646
	0.050	-0.009315896675, -11.74068410	-0.008259866067, -13.24174013
	0.075	0.005363836706, -12.38036383	0.005257711402, -12.63025771
4d	0.025	-0.04123429366, -11.08376571	-0.03301776018, -13.84198224
	0.050	-0.006652702848, -11.74334730	-0.005898852562, -13.24410115
	0.075	0.01103813411, -12.38603813	0.01081993497, -12.63581993
4f	0.025	-0.04029105188, -11.08470895	-0.03226346048, -13.84273654
	0.050	-0.003103656681, -11.74689634	-0.002752143970, -13.24724786
	0.075	0.01859579365, -12.39359579	0.01822863105, -12.64322863

Table 4. Eigenvalues ($E_{n\ell}$) of Eq. 29 as a function of the parameter α for **2p-4f** states, with $D = 3$ and $g = 0$.

States	α	$E_{n\ell}(A = 2.0)$	$E_{n\ell}(A = 5.0)$
2p	0.025	-0.4510416666	-3.001041666
	0.050	-0.4041666666	-2.879166666
	0.075	-0.3593750004	-2.759375001
3p	0.025	-0.1748263890	-1.266493056
	0.050	-0.1326388888	-1.149305555
	0.075	-0.09565972225	-1.037326388
3d	0.025	-0.1744097223	-1.266076389
	0.050	-0.1309722221	-1.147638888
	0.075	-0.09190972225	-1.033576388
4p	0.025	-0.07979166665	-0.6610416665
	0.050	-0.04416666666	-0.5504166665
	0.075	-0.01812500002	-0.4493750000
4d	0.025	-0.07937500000	-0.6606250000
	0.050	-0.04250000000	-0.5487500000
	0.075	-0.01437500002	-0.4456250002
4f	0.025	-0.07875000000	-0.6600000000
	0.050	-0.04000000000	-0.5462500000
	0.075	-0.008750000020	-0.4400000002

Table 5. Eigenvalues ($E_{n\ell}$) of Eq. 25 as a function of the parameter α for **2p-4f** states, with $D = 4$ and $g = 0$.

States	α	$E_{n\ell}(A = 2.0)$	$E_{n\ell}(A = 5.0)$
2p	0.025	-0.2715625000	-1.876562500
	0.050	-0.2262500000	-1.756250000
	0.075	-0.1840625002	-1.639062500
3p	0.025	-0.1167028062	-0.8988456630
	0.050	-0.07701530615	-0.7841581630
	0.075	-0.04420280616	-0.6763456635
3d	0.025	-0.1161819728	-0.8983248295
	0.050	-0.07493197280	-0.7820748300
	0.075	-0.03951530614	-0.6716581635
4p	0.025	-0.05470293210	-0.4982214506
	0.050	-0.02251543210	-0.3910339505
	0.075	-0.002202932106	-0.2957214510
4d	0.025	-0.05418209880	-0.4977006172
	0.050	-0.02043209876	-0.3889506171
	0.075	0.002484567894	-0.2910339509
4f	0.025	-0.05345293210	-0.4969714506
	0.050	-0.01751543210	-0.3860339505
	0.075	0.009047067895	-0.2844714510

Table 6. Eigenvalues ($E_{n\ell}$) of Eq. 26 as a function of the parameter α for **2p-4f** states, with $D = 5$ and $g = 0$.

States	α	$E_{n\ell}(A = 2.0)$	$E_{n\ell}(A = 5.0)$
2p	0.025	-0.1744097223	-1.266076389
	0.050	-0.1309722221	-1.147638888
	0.075	-0.09190972225	-1.033576388
3p	0.025	-0.07937500000	-0.6606250000
	0.050	-0.04250000000	-0.5487500000
	0.075	-0.01437500002	-0.4456250002
3d	0.025	-0.07875000000	-0.6600000000
	0.050	-0.04000000000	-0.5462500000
	0.075	-0.008750000020	-0.4400000002
4p	0.025	-0.03718750000	-0.3821875000
	0.050	-0.008750000000	-0.2787500000
	0.075	0.005312500000	-0.1896874998
4d	0.025	-0.03656250000	-0.3815625000
	0.050	-0.006250000000	-0.2762500000
	0.075	0.01093750000	-0.1840624998

Continue...

$4f$	0.025	-0.03572916666	-0.3807291666
	0.050	-0.002916666666	-0.2729166666
	0.075	0.01843750000	-0.1765624998

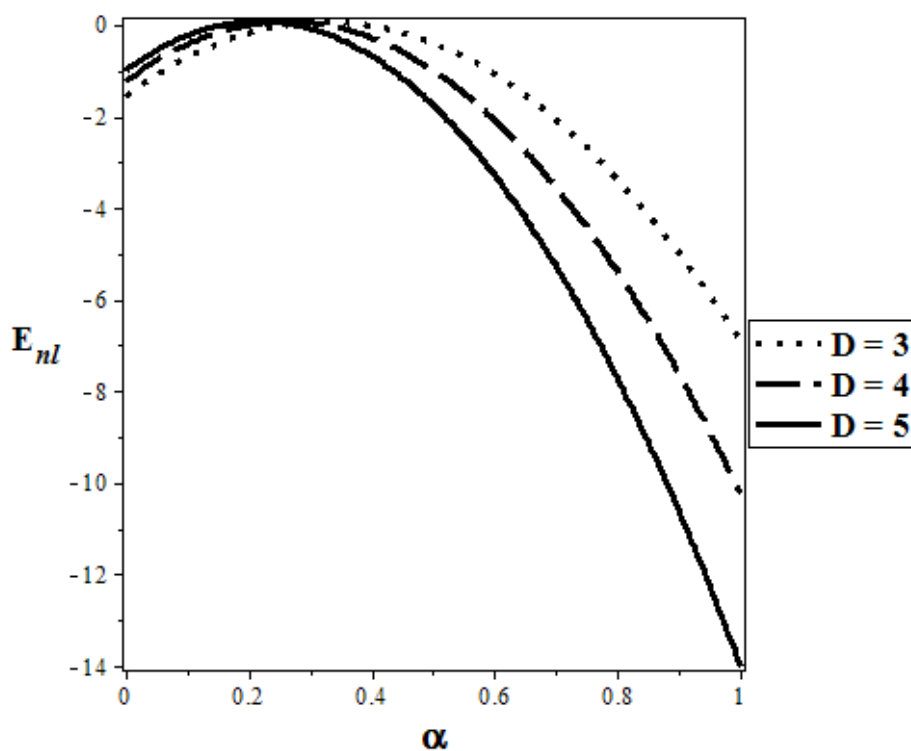


Figure 2. Energy Eigenvalue Variation with α for different dimensions with $g = 0, A = 5, n = 2, \ell = 1$.

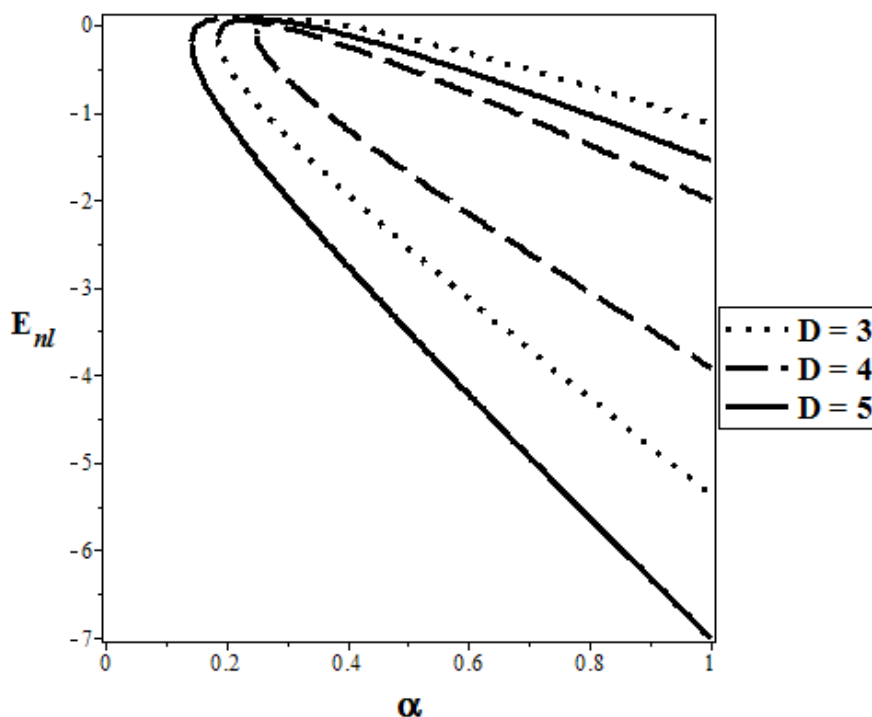


Figure 3. Energy Eigenvalue variation with α for different dimensions with $g = -1, A = 5, n = 2, \ell = 1$.

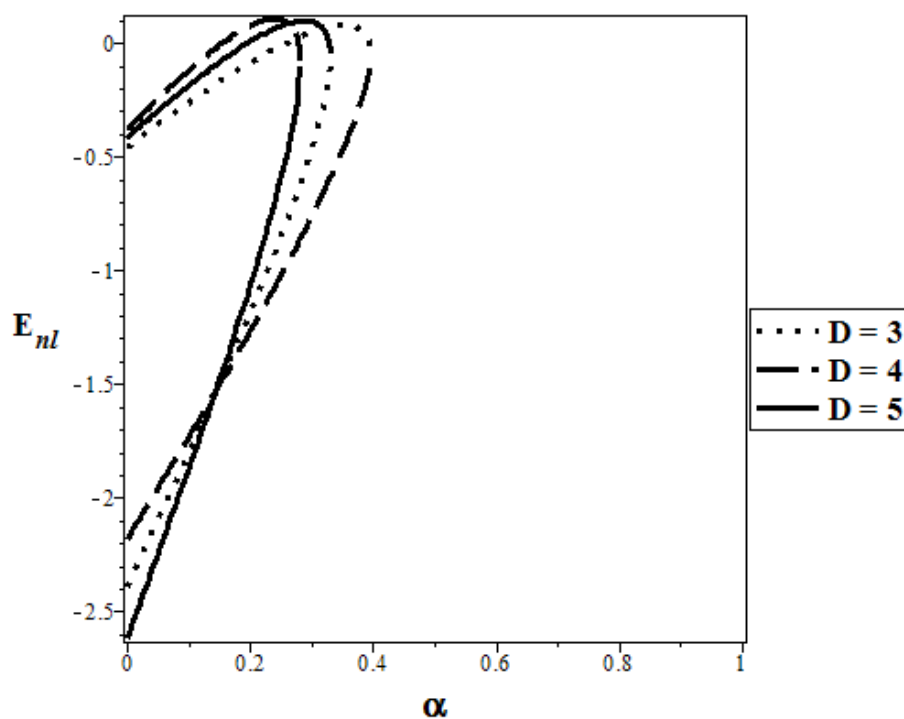


Figure 4. Energy Eigenvalue Variation with α for different dimensions with $g = 1, A = 5, n = 2, \ell = 1$.

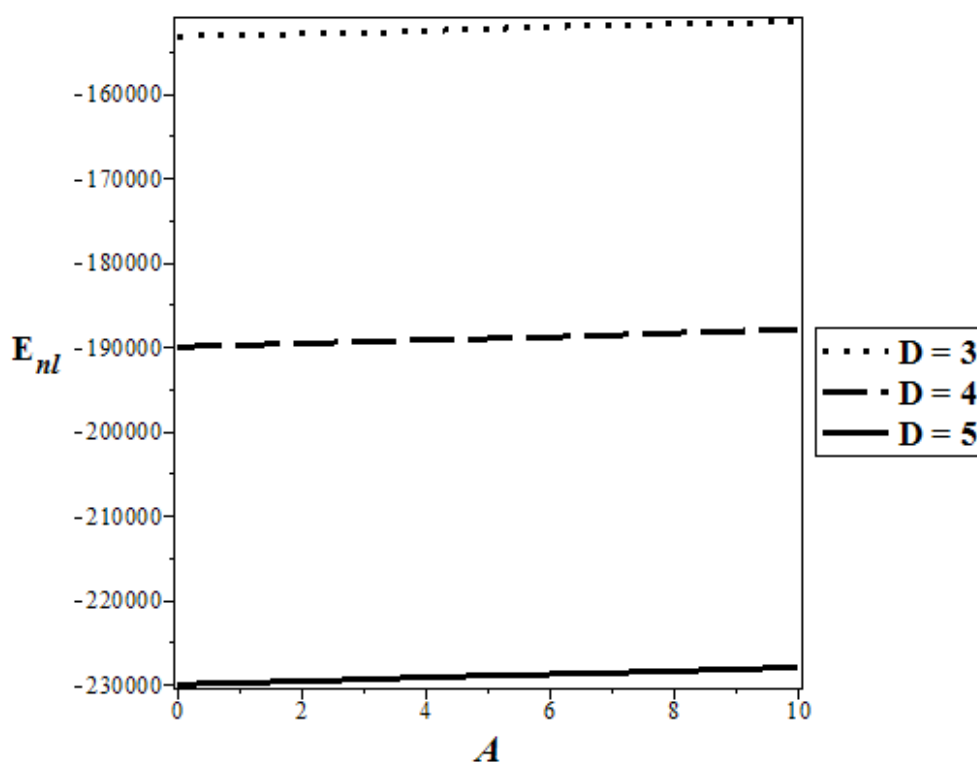


Figure 5. Energy Eigenvalue Variation with A for different dimensions with $g = 0, \alpha = 100, n = 2, \ell = 1$.

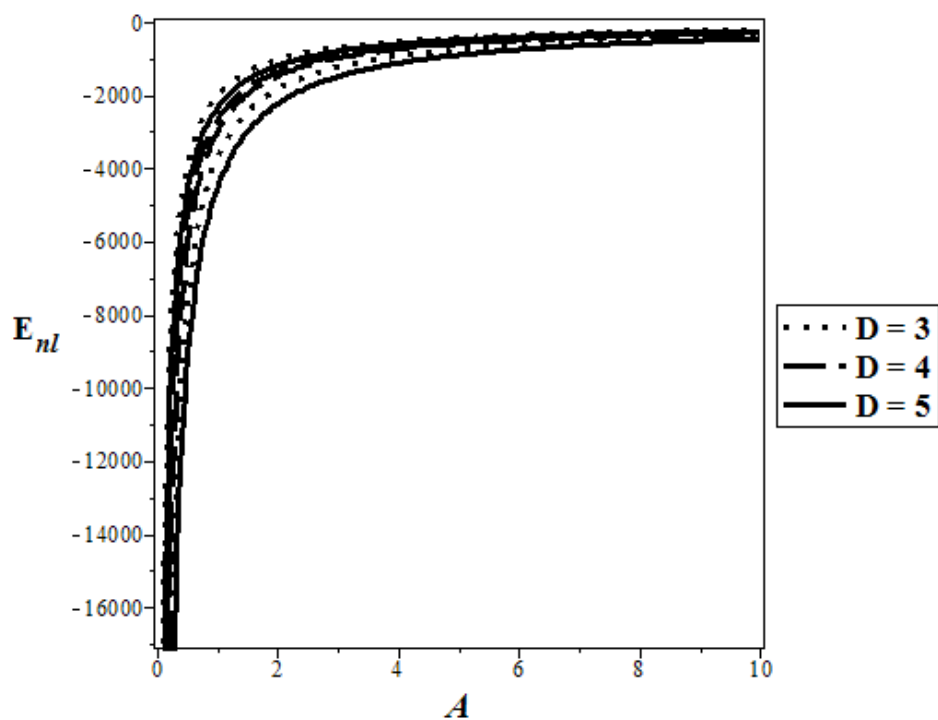


Figure 6. Energy Eigenvalue Variation with A for different dimensions with $g = -1, \alpha = 100, n = 2, \ell = 1$.

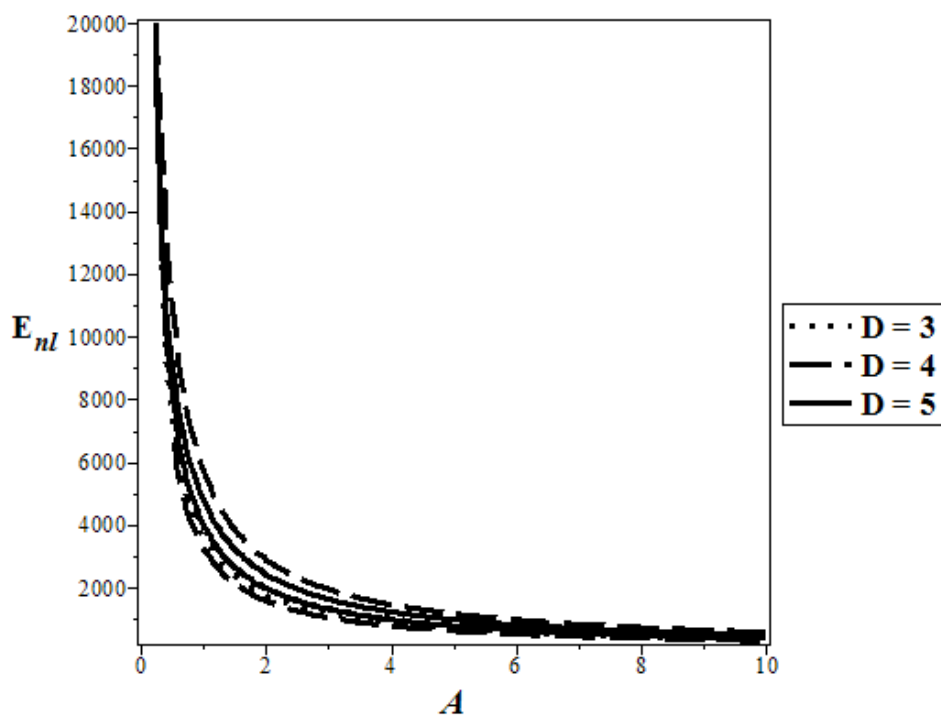


Figure 7. Energy Eigenvalue Variation with A for different dimensions with $g = 1, \alpha = 100, n = 2, \ell = 1$.

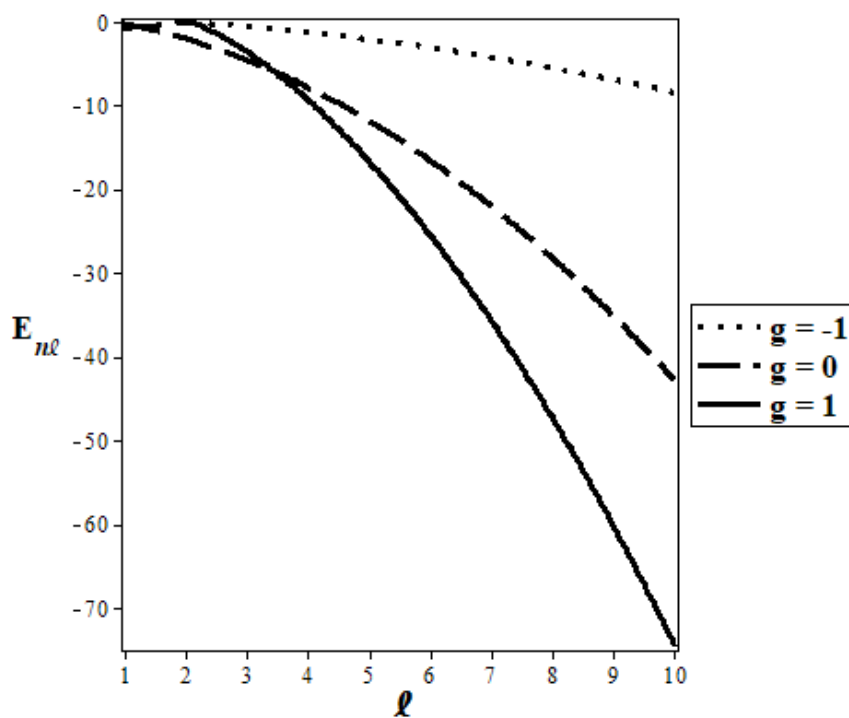


Figure 8. Energy Eigenvalue Variation with l for different values of g with $D = 3, \alpha = 1, A = 5, n = 0$.

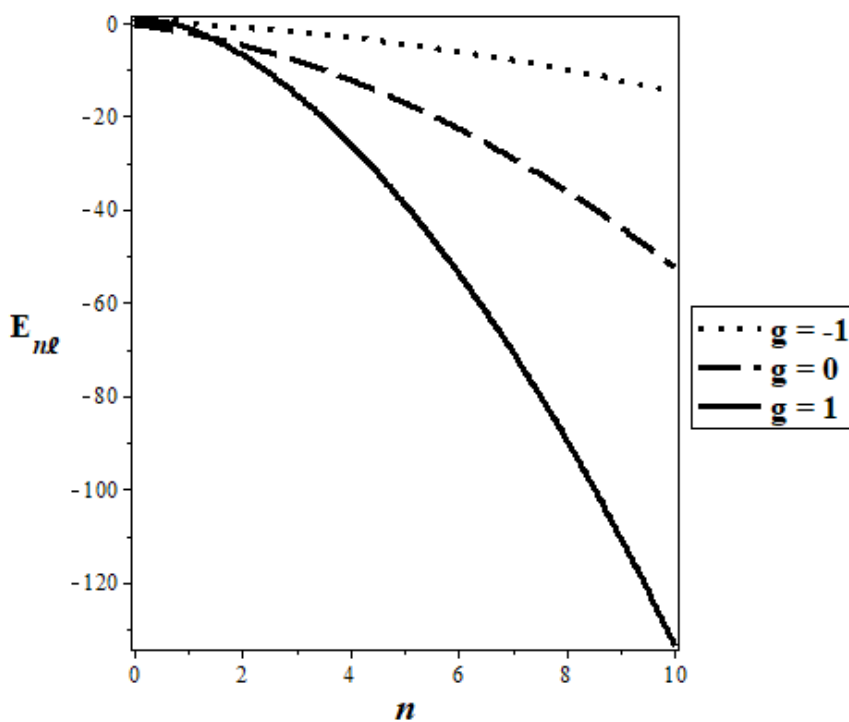


Figure 9. Energy Eigenvalue Variation with n for different values of g with $D = 3, \alpha = 1, A = 5, l = 1$.

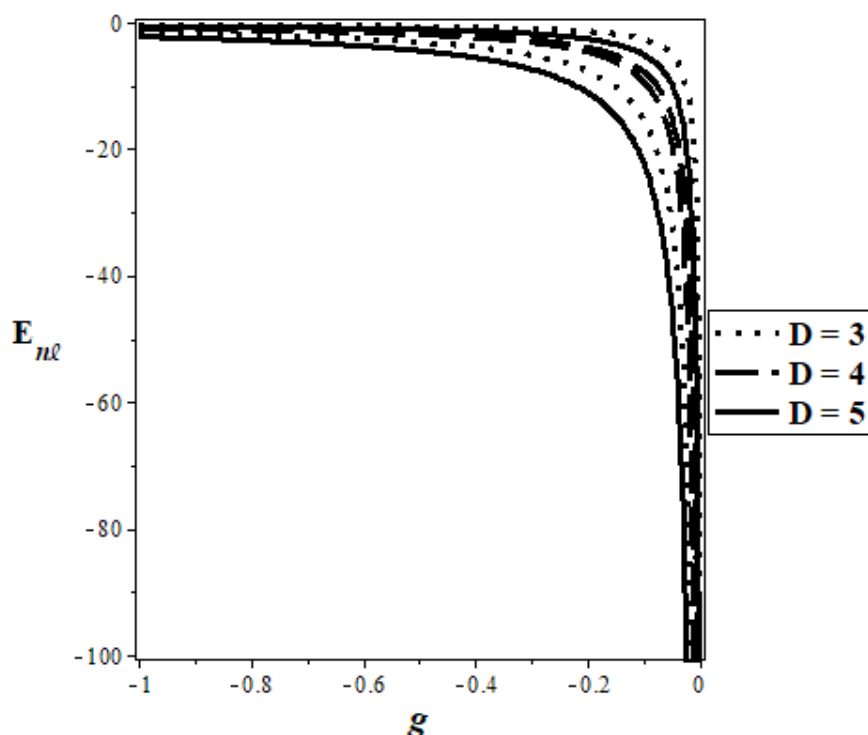


Figure 10. Energy Eigenvalue Variation with g for different dimensions, with $\alpha = 10, A = 100, n = 2, \ell = 1$

4. Conclusions

We have solved the Schrödinger equation with the energy-dependent screened Coulomb potential in higher dimensions. With the use of the conventional Nikiforov-Uvarov method and a new form of Greene-Aldrich approximation, the energy eigenvalues and its corresponding eigenfunctions were obtained approximately. Numerical values of the energy eigenvalues were also obtained with natural units, in three dimensions. We have also elucidated the variation of these energy spectra with different potential parameters and the energy slope parameter. The effect of the energy slope parameter is clearly seen in the existence of duo energy spectra, as compared to when the energy slope parameter is diminished. Special cases have been deduced, and these results agree perfectly with available literature.

Acknowledgments

The authors thank the kind reviewers for the positive comments and suggestions that lead to an improvement of our manuscript

References

- [1] Chun-Feng, H., Zhong-Xiang, Z., Yan, L., Bound states of the Klein-Gordon equation with vector and scalar Wood-Saxon potentials, *Acta Physica Sinica (Overseas Edition)* 8 (8) (1999) 561. <https://doi.org/10.1088/1004-423X/8/8/001>.
- [2] Sever, R., Tezan, C., Yeşiltaş, Ö., Bucurgat, M., Exact Solution of Effective Mass Schrödinger Equation for the Hulthen Potential, *International Journal of Theoretical Physics* 49 (9) (2008) 2243-2248. <https://doi.org/10.1007/s10773-008-9656-7>.
- [3] Yahya, W. A., Oyewumi, K. J., Thermodynamic properties and approximate solutions of the ℓ -state Pöschl-Teller-type potential, *Journal of the Association of Arab Univ. for Basic and Applied Sciences* 21 (1) (2016) 53-58. <https://doi.org/10.1016/j.jaubas.2015.04.001>.
- [4] Sun, Y., He, S., Jia, C.-S., Equivalence of the deformed modified Rosen-Morse potential energy

- model and the Tietz potential energy model, *Physica Scripta* 87 (2) (2013) 025301. <https://doi.org/10.1088/0031-8949/87/02/025301>.
- [5] Onate, C. A., Idiodi, J. O. A., Eigensolutions of the Schrödinger Equation with Some Physical Potentials, *Chinese Journal of Physics* 53 (7) (2015) 120001-1-120001-10. <https://doi.org/10.6122/CJP.20150831E>.
- [6] Antia, A. D., Ikot, A. N., Hassanabadi, H., Maghsoodi, E., Bound state solutions of Klein–Gordon equation with Mobius square plus Yukawa potentials, *Indian Journal of Physics* 87 (11) (2013) 1133-1139. <https://doi.org/10.1007/s12648-013-0336-y>.
- [7] Ikot, A. N., Awoga, O. A., Hassanabadi, H., Maghsoodi, E., Analytical Approximate Solution of Schrödinger Equation in D Dimensions with Quadratic Exponential-Type Potential for Arbitrary l -State, *Communications in Theoretical Physics* 61 (4) (2014) 457-463. <https://doi.org/10.1088/0253-6102/61/4/09>.
- [8] Falaye, B. J., Oyewumi, K. J., Abbas, M., Exact solution of Schrödinger equation with q -deformed quantum potentials using Nikiforov—Uvarov method, *Chinese Physics B* 22 (11) (2013) 110301. <https://doi.org/10.1088/1674-1056/22/11/110301>.
- [9] Ciftci, H., Hall, R. L., Saad, N., Asymptotic iteration method for eigenvalue problems, *Journal of Physics A: Mathematical and General* 36 (47) (2003) 11807-11816. <https://doi.org/10.1088/0305-4470/36/47/008>.
- [10] Falaye, B. J., Any l -state solutions of the Eckart potential via asymptotic iteration method, *Central European Journal Physics* 10 (4) (2012) 960-965. <https://doi.org/10.2478/s11534-012-0047-6>.
- [11] Setare, M. R., Karimi, E., Algebraic approach to the Kratzer potential, *Physica Scripta* 75 (1) (2007) 90-93. <https://doi.org/10.1088/0031-8949/75/1/015>.
- [12] Qiang, W. C., Dong, S. H., Proper quantization rule, *Europhysics Letters* 89 (1) (2010) 10003. <https://doi.org/10.1209/0295-5075/89/10003>.
- [13] Ikhdaïr, S. M., Sever, R., Exact quantization rule to the Kratzer-type potentials: an application to the diatomic molecules, *Journal of Mathematical Chemistry* 45 (4) (2009) 1137. <https://doi.org/10.1007/s10910-008-9438-8>.
- [14] Chen, G., The exact solutions of the Schrödinger equation with the Morse potential via Laplace transforms, *Physics Letters A* 326 (1-2) (2004) 55-57. <https://doi.org/10.1016/j.physleta.2004.04.029>.
- [15] Onate, C. A., Ojonubah, J. O., Eigensolutions of the Schrödinger equation with a class of Yukawa potentials via supersymmetric approach, *Journal of Theoretical and Applied Physics* 10 (1) (2016) 21-26. <https://doi.org/10.1007/s40094-015-0196-2>.
- [16] Ikot, A. N., Obong, H. P., Abbey, T. M., Zare, S., Ghafourian, M., Hassanabadi, H., Bound and Scattering State of Position Dependent Mass Klein–Gordon Equation with Hulthen Plus Deformed-Type Hyperbolic Potential, *Few-Body Systems* 57 (9) (2016) 807-822. <https://doi.org/10.1007/s00601-016-1111-3>.
- [17] Onate, C. A., Onyeaju, M. C., Ikot, A. N., Ojonubah, J. O., Analytical solutions of the Klein–Gordon equation with a Combined potential, *Chinese Journal of Physics* 54 (5) (2016) 820-829. <https://doi.org/10.1016/j.cjph.2016.08.007>.
- [18] Onate, C. A., Ikot, A. N., Onyeaju, M. C., Udoh M. E., Bound state solutions of D-dimensional Klein–Gordon equation with hyperbolic potential, *Karbala International Journal of Modern Science* 3 (1) (2017) 1-7. <https://doi.org/10.1016/j.kijoms.2016.12.001>.
- [19] Okorie, U. S., Ibekwe, E. E., Onyeaju, M. C., Ikot, A. N., Solutions of the Dirac and Schrödinger equations with shifted Tietz-Wei potential, *The European Physical Journal Plus* 133 (10) (2018) 433. <https://doi.org/10.1140/epjp/i2018-12307-4>.
- [20] Okorie, U. S., Ikot, A. N., Edet, C. O., Akpan, I. O., Sever, R., Rampho, G. J., Solutions of the Klein Gordon equation with generalized hyperbolic potential in D-dimensions, *Journal of Physics Communications* 3 (9) (2019) 095015. <https://doi.org/10.1088/2399-6528/ab42c6>.
- [21] Dong, S.-H., *Factorization Method in Quantum Mechanics*, Springer, Dordrecht, 2007. <https://doi.org/10.1007/978-1-4020-5796-0>.
- [22] Jia, C.-S., Jia, Y., Relativistic rotation-vibrational energies for the Cs_2 molecule, *The European Physical Journal D* 71 (1) (2017) 3. <https://doi.org/10.1140/epjd/e2016-70415-y>.
- [23] Dong, S., Sun, G.-H., Dong, S.-H., Arbitrary l -Wave Solutions of the Schrödinger Equation for the Screen Coulomb Potential, *International Journal of Modern Physics E* 22 (6) (2013) 1350036. <https://doi.org/10.1142/S0218301313500365>.
- [24] Ikhdaïr, S. M., Sever, R., A perturbative treatment for the bound states of the Hellmann potential, *Journal of Molecular Structure: THEOCHEM* 809 (1-3) (2007) 103-113. <https://doi.org/10.1016/j.theochem.2007.01.019>.

- [25] Liverts, E. Z., Drukarev, E. G., Krivec, R., Mandelzweig, V. B., Analytic presentation of a solution of the Schrödinger equation, *Few-Body Systems* 44 (1-4) (2008) 367-370. <https://doi.org/10.1007/s00601-008-0328-1>.
- [26] Maghsoodi, E., Hassanabadi, H., Aydoğdu, O., Dirac particles in the presence of the Yukawa potential plus a tensor interaction in SUSYQM framework, *Physica Scripta* 86 (1) (2012) 015005. <https://doi.org/10.1088/0031-8949/86/01/015005>.
- [27] Edwards, J. P., Gerber, U., Schubert, C., Trejo, M. A., Weber, A., The Yukawa potential: ground state energy and critical screening, *Progress of Theoretical and Experimental Physics* 2017 (8) (2017) 083A01. <https://doi.org/10.1093/ptep/ptx107>.
- [28] Hamzavi, H., Movahedi, M., Thylwe, K.-E., Rajabi, A. A., Approximate Analytical Solution of the Yukawa Potential with Arbitrary Angular Momenta, *Chinese Physics Letters* 29 (8) (2012) 080302. <https://doi.org/10.1088/0256-307X/29/8/080302>.
- [29] Garcia-Martínez, J., García-Ravelo, J., Peña, J. J., Schulze-Halberg, A., Exactly solvable energy-dependent potentials, *Physics Letters A* 373 (40) (2009) 3619-3623. <https://doi.org/10.1016/j.physleta.2009.08.012>.
- [30] Yekken, R., Lombard, R. J., Energy-dependent potentials and the problem of the equivalent local potential, *Journal of Physics A: Mathematical and Theoretical* 43 (2010) 125301. <https://doi.org/10.1088/1751-8113/43/12/125301>.
- [31] Yekken, R., Lassaut, M., Lombard, R. J., Applying supersymmetry to energy dependent potentials, *Annals of Physics* 338 (2013) 195-206. <https://doi.org/10.1016/j.aop.2013.08.005>.
- [32] Hassanabadi, H., Zarrinkamar, S., Rajabi, A. A., Exact Solutions of D -Dimensional Schrödinger Equation for an Energy-Dependent Potential by NU Method, *Communications in Theoretical Physics* 55 (2011) 541-544. <https://doi.org/10.1088/0253-6102/55/4/01>.
- [33] Hassanabadi, H., Zarrinkamar, S., Hamzavi, H., Rajabi, A. A., Exact Solutions of D -Dimensional Klein-Gordon Equation with an Energy-Dependent Potential by Using of Nikiforov-Uvarov Method, *Arabian Journal for Science and Engineering* 37 (2012) 209-215. <https://doi.org/10.1007/s13369-011-0168-z>.
- [34] Lombard, R. J., Mareš, J., Volpe, C., Wave equation with energy-dependent potentials for confined systems, *Journal of Physics G: Nuclear and Particle Physics* 34 (2007) 1879-1889. <https://doi.org/10.1088/0954-3899/34/9/002>.
- [35] Lombard, R. J., Mares, J., The many-body problem with an energy-dependent confining potential, *Physics Letters A* 373 (4) (2009) 426-429. <https://doi.org/10.1016/j.physleta.2008.12.009>.
- [36] Gupta, P., Mehrotra, I., Study of Heavy Quarkonium with Energy Dependent Potential, *Journal of Modern Physics* 3 (10) (2012) 1530-1536. <https://doi.org/10.4236/jmp.2012.310189>.
- [37] Budaca, R., Bohr Hamiltonian with an energy-dependent γ -unstable Coulomb-like potential, *The European Physical Journal A* 52 (2016) 314. <https://doi.org/10.1140/epja/i2016-16314-8>.
- [38] Boumali, A., Labidi, M., Shannon entropy and Fisher information of the one-dimensional Klein-Gordon oscillator with energy-dependent potential, *Modern Physics Letters A* 33 (6) (2018) 1850033. <https://doi.org/10.1142/S0217732318500335>.
- [39] Hassanabadi, H., Yazarloo, B. H., Zarrinkamar, S., Rahimov, H., Deng-Fan Potential for Relativistic Spinless Particles — an Ansatz Solution, *Communications in Theoretical Physics* 57 (3) (2012) 339-342. <https://doi.org/10.1088/0253-6102/57/3/02>.
- [40] Nikiforov, A. F., Uvarov, V. B., *Special Functions of Mathematical Physics*, Basel, Birkhäuser, 1998.
- [41] Birkdemir, C., Application of the Nikiforov-Uvarov Method in Quantum Mechanics, In: *Theoretical Concept of Quantum Mechanics*, Pahlavani, M. R., ed., InTech: Rijeka, Croatia, 2012, Ch. 11. <https://doi.org/10.5772/33510>.
- [42] Abramowitz, M., Stegun, I. A., *Handbook of Mathematical Functions with Formulas, Graphs and Mathematical Tables*, U.S. Government Printing Office, Washington, 1964. http://people.math.sfu.ca/~cbm/aands/abramowitz_and_stegun.pdf.

Appendix: Review of Nikiforov-Uvarov (NU) method

According to Nikiforov and Uvarov⁴⁰, the NU method transforms Schrödinger-like equations into a second order differential equation using a coordinate transformation $z = z(r)$, which is given by Eq. A1.

$$\psi \frac{\tilde{\tau}(z)'}{\sigma(z) \sigma^2(z)} \quad (\text{A1})$$

Here, $\tilde{\sigma}(z), \sigma(z)$ are polynomials of at most second degree, and $\tilde{\tau}(z)$ is a first-degree polynomial. By employing the transformation (Eq. A2),

$$\psi(z) = \Phi(z)y_n(z) \quad (\text{A2})$$

we obtain the exact solution of Eq. A1 in a form of hypergeometric-type equation given by Eq. A3.

$$\sigma(z)y_n''(z) + \tau(z)y_n'(z) + \lambda y_n(z) = 0 \quad (\text{A3})$$

Let us define the logarithm derivative function $\Phi(z)$ as⁴⁰ (Eq. A4).

$$\frac{\Phi'(z)}{\Phi(z)} = \frac{\pi(z)}{\sigma(z)} \quad (\text{A4})$$

where $\pi(z)$ is at most a first-degree polynomial. The second part of $\psi(z)$ being $y_n(z)$ in Eq. A2, is the hypergeometric function with its polynomial solution given by Rodrigues relation (Eq. A5)

$$y_n(z) = \frac{B_n}{\rho(z)} \frac{d^n}{dz^n} [\sigma^n(z)\rho(z)] \quad (\text{A5})$$

Let us mention here that B_n is the normalization constant and $\rho(z)$ is the weight function which must satisfy the condition expressed by Eq. A6.

$$\frac{d}{dz} [\sigma(z)\rho(z)] = \tau(z)\rho(z) \quad (\text{A6})$$

with Eq. A7

$$\tau(z) = \tilde{\tau}(z) + 2\pi(z) \quad (\text{A7})$$

The eigenfunctions and eigenvalues can be obtained using the definition of the following function $\pi(z)$ and parameter λ as shown (Eq. A8):

$$\pi(z) = \frac{\sigma'(z) - \tilde{\tau}(z)}{2} \pm \sqrt{\left(\frac{\sigma'(z) - \tilde{\tau}(z)}{2}\right)^2 - \tilde{\sigma}(z) + k\sigma(z)} \quad (\text{A8})$$

and (Eq. A9)

$$\lambda = k + \pi'(z) \quad (\text{A9})$$

To obtain the value of k , we set the discriminant of the square root in Eq. A8 equal to zero. As such, the new eigenvalue equation (Eq. A10) is obtained as

$$\lambda + n\tau'(z) + \frac{n(n-1)}{2} \sigma''(z) = 0, \quad (n = 0, 1, 2, \dots) \quad (\text{A10})$$

Electrochemical noise analysis to obtain the R_{sn} value via FFT using Excel

Sidinea Barrozo¹, Riberto Nunes Peres², Marcus José Witzler³, Assis Vicente Benedetti², Cecílio Sadao Fugivara²⁺

1. São Paulo State University (Unesp), Institute of Chemistry, Engineering, Physics and Mathematics Department, Araraquara, São Paulo, Brazil

2. São Paulo State University (Unesp), Institute of Chemistry, Department of Analytical Chemistry, Physical Chemistry, and Inorganic, Araraquara, São Paulo, Brazil

3. EMBRAER

*Corresponding author: Cecilio Sadao Fugivara, Phone: +55 16 33019654, Email address: sadao.fugivara@unesp.br

ARTICLE INFO

Article history:

Received: June 02, 2020

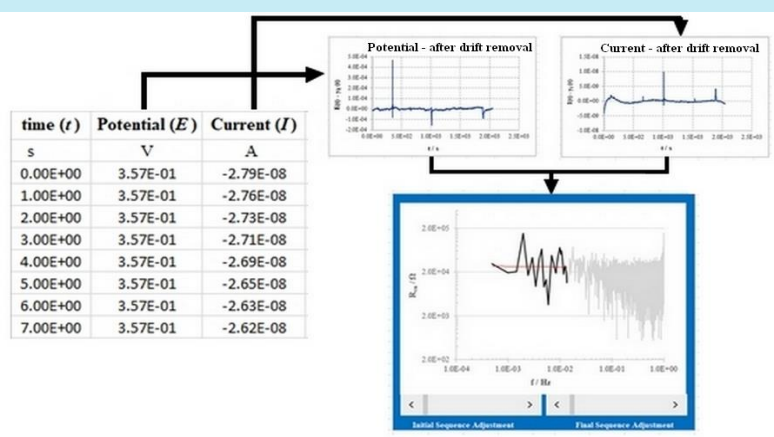
Accepted: August 06, 2020

Published: October 01, 2020

Keywords:

1. ENA
2. Excel
3. spectral electrochemical noise resistance
4. detrending
5. Hann window

ABSTRACT: Electrochemical noise (EN) measurements are based on the fluctuations of the electrochemical potential and the current that occur during, for example, a corrosion process without an external signal perturbation. EN analysis (ENA) allows assessment of the type of corrosion and rapid determination of the corrosion rate. Microsoft Excel®, an inexpensive and readily available software package, is an excellent tool for performing repetitive calculations, with automation that saves time for the users. It is a useful tool for the analysis of EN data using fast Fourier transform (FFT), a process that is often made repeatedly and, if not automated, is quite laborious. This work presents a step-by-step procedure using Excel to perform



these calculations, automating the process of obtaining the spectral electrochemical noise resistance, R_{sn}^0 . This routine was used to analyze experimental potential and current noise data recorded for chalcopyrite. The results were comparable to those obtained for the same set of experimental data using Origin® software.

1. Introduction

Electrochemical noise (EN) measurements concern the fluctuations of the electrochemical potential and the current that occur during corrosion processes, without applying an external signal perturbation. EN can be used to monitor the type of corrosion and to rapidly obtain the corrosion rate. The electrochemical potential and current noises are simultaneously measured either by coupling two nominally similar working electrodes connected by a zero-resistance ammeter (ZRA), so that the potential difference between

the working electrodes is zero, or by measuring with respect to a reference electrode¹⁻³. In EN studies, the electrochemical noise resistance (R_n), determined as the standard deviation of the potential noise divided by the standard deviation of the electrical current noise, is generally considered as an estimation of the corrosion rate¹.

Time domain analysis does not lead directly to comparative values of corrosion rates between systems being studied, hence necessitating frequency domain analysis. In the frequency domain, the power spectral density (PSD) is useful for predicting the corrosion mechanism

and, in some cases, has been used in calculating noise impedance. PSD plots are computed using algorithms such as fast Fourier transforms (FFT)², which are advantageous when repetitive signals are measured, and the data sets acquired have large numbers of sampling points. The square root of the ratio of the voltage PSD to the current PSD, as a function of frequency, enables calculation of the low frequency noise impedance, R_{sn} .

Excel software is an excellent tool for performing repetitive calculations, with automation providing considerable saving of time for users. In order to automate a repetitive task, a macro is recorded using the Macro Recorder in Excel⁴, applying the desired format, which can then be replayed whenever needed. An example of this is the possibility of its use, still little explored, for the treatment of electrochemical noise data using FFT, a process that is usually performed repeatedly and is quite laborious, if not automated. Therefore, this work presents a step-by-step procedure for performing these calculations using Excel software, automating the process of obtaining the spectral electrochemical noise resistance, R_{sn}^0 , using experimental potential and current noise data recorded for chalcopyrite in the laboratory. The R_{sn}^0 value is calculated, as proposed by Mansfeld and Lee⁵, using Eq. 1:

$$R_{sn}^0 = \lim_{f \rightarrow 0} R_{sn}(f), \quad (1)$$

with

$$R_{sn}(f) = \left| \frac{PSD_E(f)}{PSD_i(f)} \right|^{\frac{1}{2}}, \quad (2)$$

where $PSD_E(f)$ and $PSD_i(f)$ are the power spectral density of the potential, $E(t)$, and the current density, $i(t)$, respectively, in the frequency domain f .

$$X_T(f_m) = \sum_{n=0}^{N-1} x(n\Delta t) e^{-\frac{2\pi mnj}{N} \Delta t}, m = 0, 1, 2, \dots, N - 1, \quad (6)$$

where $f_m = m\Delta f$ is the frequency related to the m -th sampling point and x is the function to be transformed (in this case, the potential E and the current density i). The FFT is an algorithm that optimizes the calculations by making them faster, compared to the discrete Fourier transform, and for its use the data set should contain a number of points equal to a power of 2

In the practical process, R_{sn}^0 is determined by the linear regression of $\log(R_{sn}(f))$ vs. $\log(f)$ at the “plateau” in the low frequency region, as suggested in the literature³, covering a minimum of 10 frequency points. The straight-line equation fitted is evaluated using the lowest frequency of the recorded data, with the result being the R_{sn}^0 value.

In this work, the PSD calculation employs Eq. 3⁶:

$$PSD_x(f) = \frac{2}{T} |X_T(f)|^2, \quad (3)$$

where $X_T(f)$ is the Fourier transform of $x(t)$, given by Eq. 5, T is the experimental time ($T = N\Delta t$, where N is the number of experimental data points and Δt is the time interval between measurements), and the number 2 indicates that only positive frequencies are considered, since the Fourier transform can also apply to negative frequencies.

The Fourier transform of a function $x(t)$ is defined by Eq. 4:

$$X(f) = \int_{-\infty}^{+\infty} x(t) e^{-2\pi jft} dt, \quad (4)$$

where $j^2 = -1$ is the imaginary unit and, among other properties, converts the time domain into a frequency domain. Since the signals are considered in the time interval between 0 and T , the Fourier transform calculations are made from the integral, according to Eq. 5:

$$X_T(f) = \int_0^T x(t) e^{-2\pi jft} dt, \quad (5)$$

with the integral being numerically calculated by Eq. 6, called a discrete Fourier transform⁶:

(for example, $2048 = 2^{11}$). In Excel, this algorithm is implemented using the “Fourier Analysis” function.

Note that Eq. 2, for calculation of $R_{sn}(f)$, involves the ratio between PSD_E and PSD_i , so the factor $2/T$ of Eq. 3 will be canceled in the operation. Hence, in this work, PSD_E and PSD_i will be obtained using Eq. 7:

$$PSD_x(f) = |X_T(f)|^2 = [Re(X_T(f))]^2 + [Im(X_T(f))]^2, \quad (7)$$

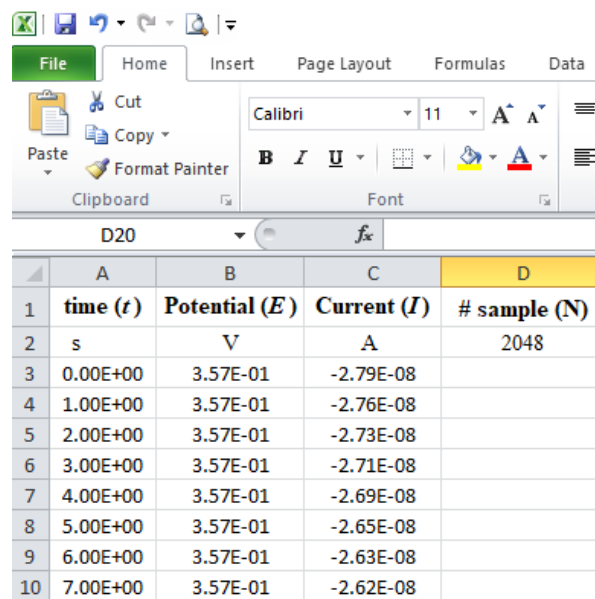
since $X_T(f)$ is a complex number, and the modulus of a complex number $z = a + bj$ is given by $|z| = \sqrt{a^2 + b^2}$, so $|z|^2 = a^2 + b^2$.

As the goal of this work is to provide a routine to obtain R_{sn}^0 using Excel software, we indicate the criterion that will be used for delimiting the frequency region, without elaborating on any particular merits of this procedure, leaving it to the ENA user to select the criterion most suitable for the study being undertaken. In addition to describing how the value of R_{sn}^0 can be calculated using Excel, the results are compared with those obtained for the same set of experimental data using Origin[®] software.

2. Methodology

The Excel commands presented in this guide follow the 2010/2013 versions of the software. If another version is used, it would be necessary to check the equivalent commands. It is recommended to use the configuration with a dot as the decimal separator, since the original data is generated in this format. To make the change from comma to dot, follow these commands: File → Options → Advanced → Editing options → Use system separators → make the change.

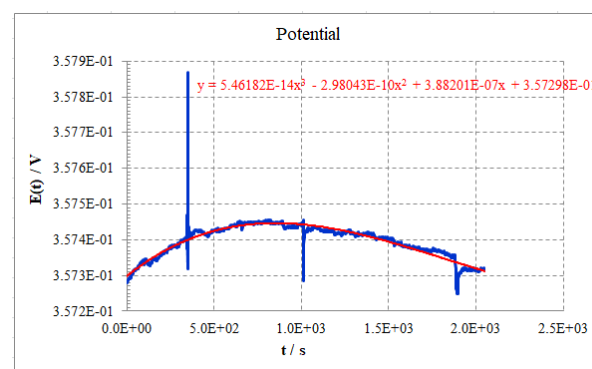
This analysis considered 2048 points of an experimental data set obtained in the low frequency region, but the routine can be applied to any other number of points, as long as the number is a power of 2. The experimental data were arranged in three columns, considering time (t) in seconds (s), potential (E) in volts (V), and current (I) in amperes (A), in a worksheet named Data. It is possible that the experimental data set could have more than 2048 points, so it is important to count the number of data points in the spreadsheet (Formulas → Insert Function → COUNT → OK → select a set of data (column) → OK), in order to leave only 2048 points, deleting the points in excess in the high frequency region. An example of an input spreadsheet is shown in Fig. 1.



	A	B	C	D
1	time (t)	Potential (E)	Current (I)	# sample (N)
2	s	V	A	2048
3	0.00E+00	3.57E-01	-2.79E-08	
4	1.00E+00	3.57E-01	-2.76E-08	
5	2.00E+00	3.57E-01	-2.73E-08	
6	3.00E+00	3.57E-01	-2.71E-08	
7	4.00E+00	3.57E-01	-2.69E-08	
8	5.00E+00	3.57E-01	-2.65E-08	
9	6.00E+00	3.57E-01	-2.63E-08	
10	7.00E+00	3.57E-01	-2.62E-08	

Figure 1. Example of data presentation used in the analysis.

Considering that it is often necessary to remove the drift before analyzing the data^{7,8}, this guide suggests a polynomial removal procedure. For this, graphs are constructed of potential or current against time, adding a trendline that provides the best fit to the data. This can be performed using the following commands: position the cursor on the graph and press the right button of the mouse → Add Trendline → Polynomial → choose the order that provides the best fit → mark Display Equation on chart → Close. Note that the polynomial orders for potential and current may be different each other. Format the graph and trendline, as desired. Fig. 2 shows examples.



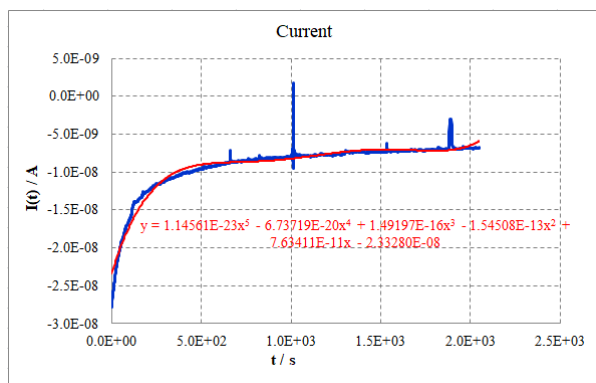


Figure 2. Examples of potential and current graphs, with trendlines.

In order to remove the drift, create new columns with the following parameters: time (t); potential value from the trendline ($y_E(t)$), using the polynomial coefficients given by the potential fit; current value from the trendline ($y_I(t)$), using the polynomial coefficients given by the current fit; and the differences between the experimental and fitted values for potential and current ($E(t) - y_E(t)$ and $I(t) - y_I(t)$, respectively), as shown in Fig. 3.

O	P	Q	R	S
t	$y_E(t)$	$y_I(t)$	$E(t) - y_E(t)$	$I(t) - y_I(t)$
0.00E+00	3.57298E-01	-2.33E-08	-1.73E-05	-4.54E-09
1.00E+00	3.57298E-01	-2.33E-08	-1.71E-05	-4.38E-09
2.00E+00	3.57299E-01	-2.32E-08	-1.52E-05	-4.16E-09
3.00E+00	3.57299E-01	-2.31E-08	-1.49E-05	-4.01E-09
4.00E+00	3.57300E-01	-2.30E-08	-1.58E-05	-3.85E-09
5.00E+00	3.57300E-01	-2.29E-08	-1.38E-05	-3.58E-09
6.00E+00	3.57300E-01	-2.29E-08	-1.65E-05	-3.46E-09
7.00E+00	3.57301E-01	-2.28E-08	-1.65E-05	-3.35E-09
8.00E+00	3.57301E-01	-2.27E-08	-1.49E-05	-3.23E-09
9.00E+00	3.57301E-01	-2.27E-08	-1.33E-05	-3.08E-09
1.00E+01	3.57302E-01	-2.26E-08	-1.32E-05	-2.98E-09

Figure 3. Example of columns for removal of the drift from the potential and current data.

It is recommended to construct graphs of potential and current after removing the drift, in order to visualize the results and confirm that the values are near $y = 0$. Figure 4 shows an example.

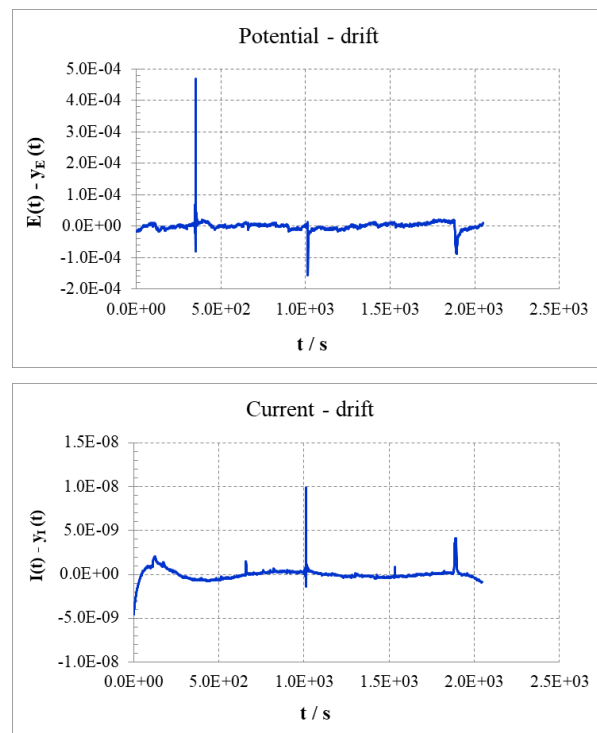


Figure 4. Examples of potential and current graphs after removing the drift.

In many cases, it is necessary to use appropriate windows to improve the quality of treatment by FFT. This guide uses the Hann window^{6,9}, which is one of the most suitable. It is defined by the function:

$$H_W(n) = \frac{1}{2} \left[1 - \cos\left(\frac{2\pi n}{N-1}\right) \right], n = 0, 1, 2, 3, \dots, N-1, \quad (8)$$

where N is the total number of points used (in this case, 2048) and n is the position of each experimental point, initiating at zero. This function must be multiplied by the values of $E(t) - y_E(t)$ and $I(t) - y_I(t)$, which are calculated as described above. Figure 5 shows the Data spreadsheet updated so far, where a column with numbers n was created (column T) to apply the Hann window (columns U and V) and the value of N (fixed, in this case given in cell D2). Note that to fix a cell, just click on it, and press the F4 key on the keyboard.

f _c =0.5*(1-COS(2*PI()*T3/(\$D\$2-1)))*R3							
O	P	Q	R	S	T	U	V
t	y _E (t)	y _I (t)	E(t) - y _E (t)	I(t) - y _I (t)	n	H _W (E(t) - y _E (t))	H _W (I(t) - y _I (t))
0.00E+00	3.57298E-01	-2.33E-08	-1.73E-05	-4.54E-09	0	0.00E+00	0.00E+00
1.00E+00	3.57298E-01	-2.33E-08	-1.71E-05	-4.38E-09	1	-4.03E-11	-1.03E-14
2.00E+00	3.57299E-01	-2.32E-08	-1.52E-05	-4.16E-09	2	-1.43E-10	-3.92E-14
3.00E+00	3.57299E-01	-2.31E-08	-1.49E-05	-4.01E-09	3	-3.15E-10	-8.50E-14
4.00E+00	3.57300E-01	-2.30E-08	-1.58E-05	-3.85E-09	4	-5.97E-10	-1.45E-13
5.00E+00	3.57300E-01	-2.29E-08	-1.38E-05	-3.58E-09	5	-8.11E-10	-2.11E-13
6.00E+00	3.57300E-01	-2.29E-08	-1.65E-05	-3.46E-09	6	-1.40E-09	-2.94E-13
7.00E+00	3.57301E-01	-2.28E-08	-1.65E-05	-3.35E-09	7	-1.90E-09	-3.87E-13
8.00E+00	3.57301E-01	-2.27E-08	-1.49E-05	-3.23E-09	8	-2.24E-09	-4.87E-13
9.00E+00	3.57301E-01	-2.27E-08	-1.33E-05	-3.08E-09	9	-2.53E-09	-5.87E-13
1.00E+01	3.57302E-01	-2.26E-08	-1.32E-05	-2.98E-09	10	-3.11E-09	-7.03E-13

Figure 5. Spreadsheet example with the Hann window applied to data of the R and S columns.

Therefore, if the Hann window is not applied, the data of columns O, R, and S should be directly used in the analysis; if the Hann window is applied, the data of columns O, U, and V should be used.

Once the input data are organized, insert a new worksheet in the spreadsheet, in this example named Analysis, to perform the calculations. The step-by-step procedures for building the Analysis worksheet are presented below.

Save the spreadsheet with extension .xslm (Excel Macro Enabled Workbook). Copy the input data (columns O, R, and S of the Data worksheet, if the Hann window is not used in the input data, or columns O, U, and V, if it is used) and paste from the 5th or 6th row of the first column (A) of the Analysis worksheet, in order to leave the starting lines for captions, comments, and new data to be inserted. We suggest, for example, that the number of data points (N) is informed at the beginning of column A, the time interval between measurements (Δt) in column B, the electrode area (cm²) in column C, and a scale factor with magnitude of 10² or 10³ in column D, as this information will be used in future calculations. We also suggest using Excel facilities to count the number of data and the value of Δt , which will minimize errors. The electrode area and the scale factor must be entered manually, as they are values known by the user.

It is important to note that Excel works internally with 14 significant digits. Therefore, since the input data values can be very small, especially for the current data, some values may be considered null and the FFT calculation may fail. A way to overcome this issue is to introduce a scale factor at the beginning of the spreadsheet (in this example, in cell D2), which is used to

multiply the current density values before calculating the FFT, increasing the values to the required order of magnitude (10², 10³, ...). After the calculations, the scale factor is removed by means of a division. However, it is not necessary to perform this calculation manually since it is included in the automation of the FFT calculations. It is necessary to insert the scale factor according to the order of magnitude of i (which in this case is 10⁻¹⁴ or 10⁻¹³, consequently requiring a correction with minimal order of 10³). Figure 6 shows this procedure.

The calculations presented here are performed using Hann window and current density (i , in A cm⁻²), so the experimental data related to current are divided by the electrode area, placing the result (=C6/\$C\$2) in column D. Note that as the electrode area is constant, it must be fixed when dividing.

In column E, list the input data ($n = 0, 1, 2, 3, \dots$) used for calculating the frequency (in Hz). The frequencies will be calculated in column F, using the formula: $f = n / (N * \Delta t)$. Although there is no zero frequency, it is necessary to start at $n = 0$ for the FFT calculation. To insert the formula, position the cursor in the desired cell (in the example, F6) and do: =E6/(\$A\$2*\$B\$2). Note that N and Δt are fixed, so it is necessary to fix these values, which in the example are in cells A2 and B2. Remember to copy a formula for all cells in the column, just positioning the cursor at the lower right corner of the cell to be copied and, when a cross appears, double-click. An example of the spreadsheet up to this step is shown in Fig. 6.

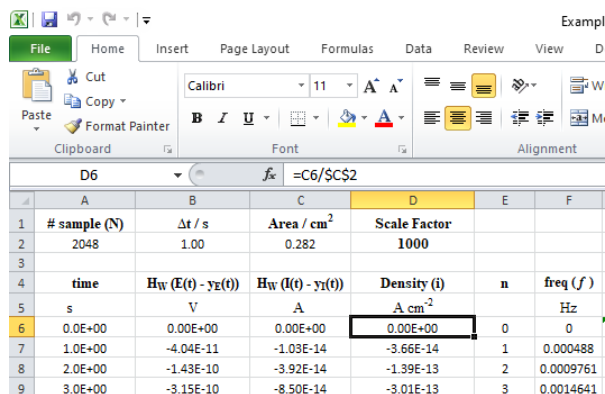


Figure 6. Example of a spreadsheet constructed to calculate R_{sn} .

To calculate the FFT_E of the potential, place the cursor in column G, aligned to the data, and follow the commands: Data → Data Analysis → Fourier Analysis → OK. A window similar to the one shown in Fig. 7 appears and, in the Input Range option, select the data from the Potential column (in the example, the data from column B). As an output option, choose “Output Range” and click on the cell where it is desired to place the FFT_E values (in the example, cell G6). Click OK and all the FFT_E values are calculated.

Note: If the Data Analysis option is not enabled in the version of Excel used, follow the commands: File → Options → Add-ins → Manage: Excel Add-ins → Go → Analysis Tools or Analysis ToolPak → OK).

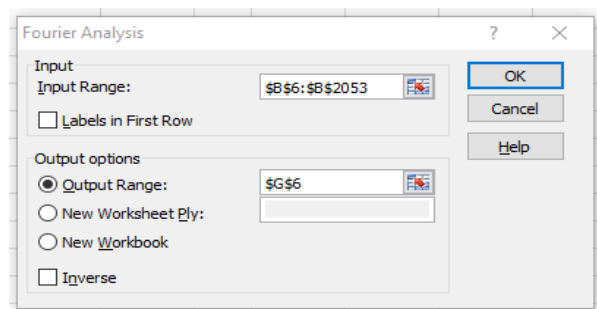


Figure 7. Fourier Analysis function window in Excel.

FFT_E	FFT_i	Real FFT_E	Im FFT_E	Real FFT_i	Im FFT_i
-6.05839046814944E-004	2.93378056156407E-005	-6.058E-04	0.000E+00	2.934E-08	0.000E+00
2.63986541670193E-003-3.81111834018308E-004i	-2.92324284934354E-004-9.25323676985686E-005i	2.640E-03	-3.811E-04	-2.923E-07	-9.253E-08
-3.79076679865553E-003+1.10001315796228E-003i	6.2331839349104E-004+3.66734930991556E-004i	-3.791E-03	1.100E-03	6.233E-07	3.667E-07
1.89796498360598E-003-1.3827831045382E-003i	-2.27822331071836E-004-3.43855342316282E-004i	1.898E-03	-1.383E-03	-2.278E-07	-3.439E-07
-1.61014786377268E-003+1.11852227920365E-003i	-4.0672458279581E-005+2.16639286709312E-005i	-1.610E-03	1.119E-03	-4.067E-08	2.166E-08
6.05939216206537E-004+3.16733838906396E-004i	-1.43290649318753E-004+3.33819134936243E-007i	6.059E-04	3.167E-04	-1.433E-07	3.338E-10
7.6000508413189E-004-1.14834203809837E-003i	1.07649822065014E-004+3.47853378744816E-005i	7.600E-04	-1.148E-03	1.076E-07	3.479E-08

Figure 9. Spreadsheet with FFT values and their real and imaginary parts discriminated.

Repeat the same procedure to generate a column with FFT_i (to calculate the FFT of the current density data), changing only the Input data to column D, and the output location to cell H6.

The result of the FFT is a complex number, so in order to perform the following calculations, it is necessary to separate the real and the imaginary parts into different columns. To do this, place the cursor on the next free column, aligned to the data (in the example, I6), and follow the commands for the real part: Formulas → Insert Function → IMREAL → click on the cell of the complex number (G6) and then on OK. The command window is shown in Fig. 8.

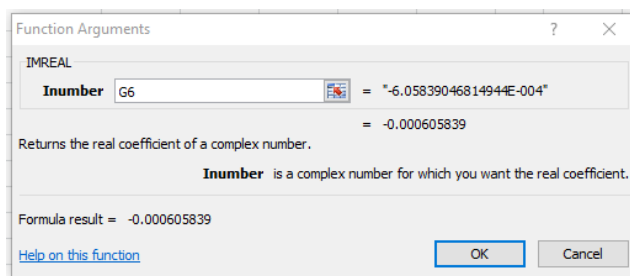


Figure 8. Function window of Excel for discrimination of the real part of a complex number.

Then, drag the formula to all the data (double-click on the little cross in the lower right corner of the cell). Do the same for the column of the imaginary part, using the function IMAGINARY. After performing the procedure for the potential and current data, a spreadsheet similar to the one shown in Fig. 9 is obtained.

The PSD_E of the potential is calculated using Eq. 7, which must be introduced in the next free column (M). In this example, it is: $=I6^2+J6^2$. Drag to all cells in the column and repeat the procedure to calculate the PSD_i of the current, which should be entered in column N.

In the next free column (O), where R_{sn} is calculated using Eq. 2, type: $=SQRT(M6/N6)$ and drag to all cells in the column.

To calculate the slope and linear coefficients of the line obtained by the linear regression of

$\log(R_{sn})$ vs. $\log(f)$, it is necessary to calculate the logarithms (base 10) for these two columns. To do this, in the next two free columns (P and Q) do: $=LOG10(F6)$ and $=LOG10(O6)$, respectively, and drag to the entire columns. Note that as the first frequency value is $f = 0$, its logarithm cannot be calculated, so the expression “#NUM!” appears in cell P6. This is not a problem, as this point can be excluded during graph construction. Figure 10 shows the example in progress.

I	J	K	L	M	N	O	P	Q
Real FFT _E	Im FFT _E	Real FFT _i	Im FFT _i	PSD _E	PSD _i	R _{sn}	log(f)	log(R _{sn})
				V	A	Ω	Hz	Ω
-6.058E-04	0.000E+00	2.934E-08	0.000E+00	3.670E-07	8.607E-16	2.065E+03	#NUM!	4.31493
2.640E-03	-3.811E-04	-2.923E-07	-9.253E-08	7.114E-06	9.402E-14	8.699E+03	-3.3115420	3.93946
-3.791E-03	1.100E-03	6.233E-07	3.667E-07	1.558E-05	5.230E-13	5.458E+03	-3.0105120	3.73702
1.898E-03	-1.383E-03	-2.278E-07	-3.439E-07	5.514E-06	1.701E-13	5.693E+03	-2.8344207	3.75534
-1.610E-03	1.119E-03	-4.067E-08	2.166E-08	3.844E-06	2.124E-15	4.254E+04	-2.7094820	4.62884

Figure 10. Spreadsheet with the calculations required to obtain R_{sn} .

This work presents a way to build the graph in Excel by adding a slider on the abscissa axis to define the region of linear regression. This selection is important for the final result of the analysis and can be performed by following the steps below. However, it is also desirable that the user should be able to see the entire graph in a background, together with the interval chosen for linear regression and using a logarithmic scale, in order to facilitate interpretation of the results, observing the results as frequency, rather than logarithm of frequency. Therefore, the graph is constructed using a logarithmic scale.

Firstly, insert two slider bars in an empty region on the worksheet, using the following commands: Developer → Insert → Scroll Bar (in Form Controls box) → choose the place where you want to put the bars, click, and drag the mouse horizontally. The bars must be placed in a position where there is space to put a graph above them (Fig. 11).

Note: If the “Developer” option is not enabled in the ribbon, follow the commands: Files → Options → Customize Ribbon → Developer (in Main Tabs box) → OK.

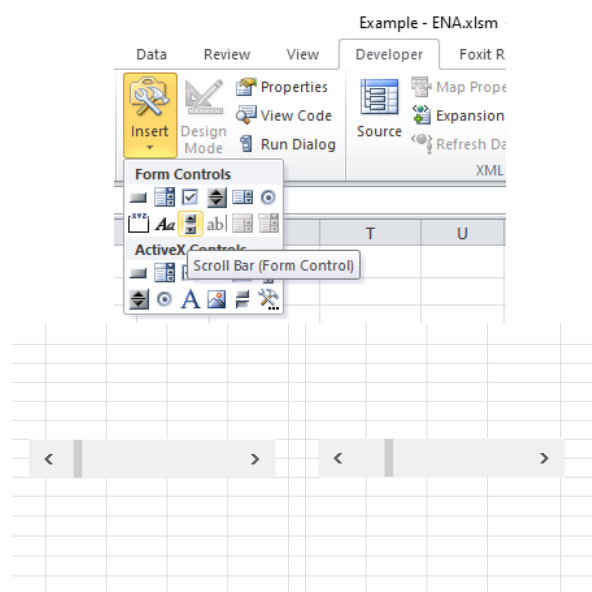


Figure 11. Illustration of commands for creating a slider bar in Excel.

Position the cursor in a cell next to the bars (in the example, T16) and type a name for the cell in the identification space (upper left corner of the worksheet), for example, “Start_Point”, as shown in Fig. 12. Repeat the procedure in the cell below, naming it “End_Point”. On the left side of these

cells, it is recommended to write the words “Initial index” and “Final index”, to indicate that the cells on the right show the positions (n) of the first and last points used in the linear fit. With this procedure, these cells have the function of variables for delimitation of the graph, using the slider.

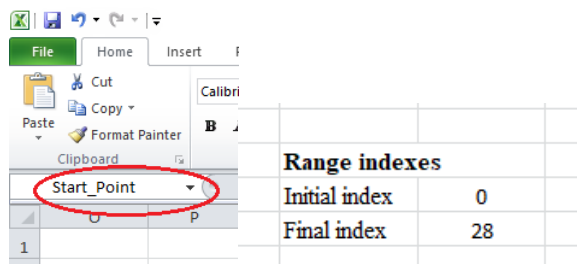


Figure 12. Cells declaring the variables.

Now position the cursor in cell P7 (the first valid value of the log (f) column) and give it a name (in the example, Ref_X_Plot), as shown in Fig. 13. These names are now used as variables in the following formulas and commands.

	R _{5a}	log(f)	log(R _{5a})
5	Ω	Hz	Ω
6	2.065E+04	#NUM!	4.31493
7	8.699E+03	-3.3115420	3.93946
8	5.458E+03	-3.0105120	3.73702
9	5.693E+03	-2.8344207	3.75534
10	4.254E+04	-2.7094820	4.62884

Figure 13. Referencing the start of the log (f) data for plotting.

Click with the right button of the mouse on each bar, select the option “Format Control” and configure each bar according to the information in Fig. 14.

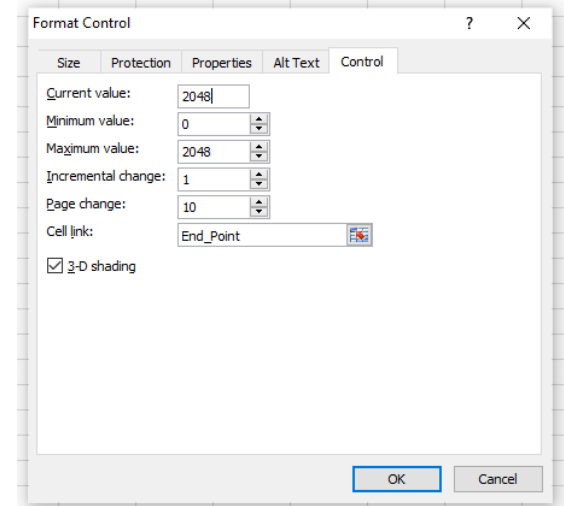
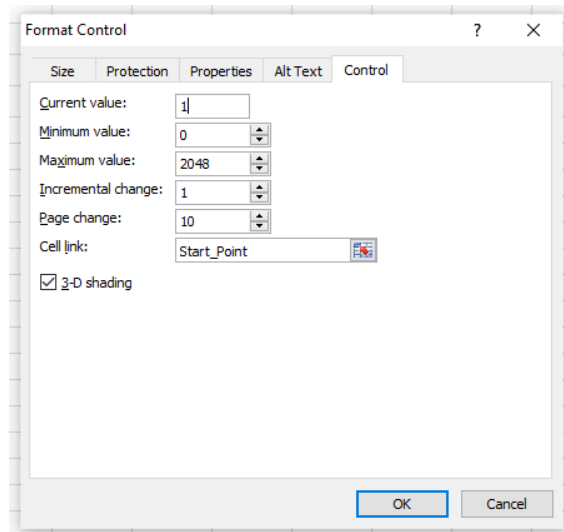


Figure 14. Configuration for formatting the sliders in this example.

It is then necessary to declare the variables not linked to cells, in order to store the data range to be plotted. For this, the OFFSET function is used, so that they have a dynamic behavior, following the commands: Formulas → Name Manager → New. A name is then typed for the first variable. In this example, Range_X is suggested. Then type the expression: =OFFSET(Ref_X_Plot; Start_Point; -10; End_Point-Start_Point; 1) in the option “Refers to” in the box → OK. Figure 15 shows this procedure.

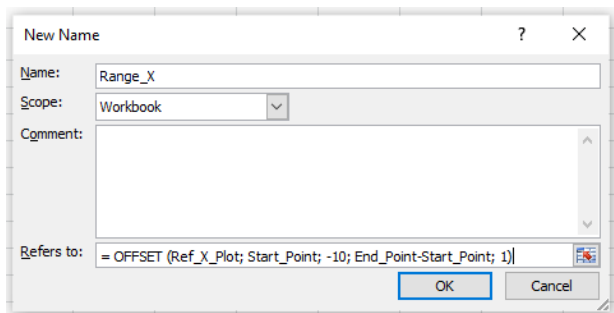


Figure 15. Declaring variables to store a range of data.

Repeat the procedure for the other variables, as shown below:

Name: Range_X_Lin → Refers to:
=OFFSET(Ref_X_Plot; Start_Point; 0;
End_Point-Start_Point; 1)

Name: Range_Y → Refers to:
=OFFSET(Ref_X_Plot; Start_Point; -1;
End_Point-Start_Point; 1)

Name: Range_Y_Lin → Refers to:
=OFFSET(Ref_X_Plot; Start_Point; 1;
End_Point-Start_Point: 1)

Now, clicking on “Name Manager”, a window similar to the one shown in Fig. 16 opens.

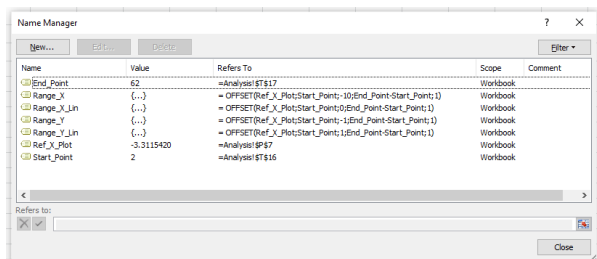


Figure 16. Window showing the variables declared in order to store a range of data.

It is now possible to make the graph. Place the cursor in an empty cell, click on “Insert” (in the ribbon) and, in the Charts group, choose preferentially the option “Scatter with Straight Lines” (Fig. 17).

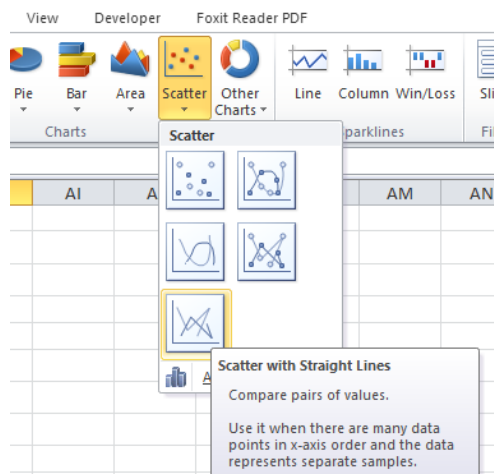


Figure 17. Steps to build the graph.

This command generates a clean graph area. Press the right mouse button on the area of that graph and select the option “Select Data”. In the dialog box that opens, select the option “Add” (Fig. 18) and a new dialog box (Edit Series) appears. In the “Series X values” option, select the frequency data (except $f = 0$), and in the “Series Y values” option, select the data for R_{sn} , except the value corresponding to $f = 0$. Click OK in both windows and the graph appears, with a linear scale. To change the scale of the graph to logarithmic, press the right mouse button on the scale of the axes → Format Axis → Logarithmic scale (Base 10). Do this for both axes.

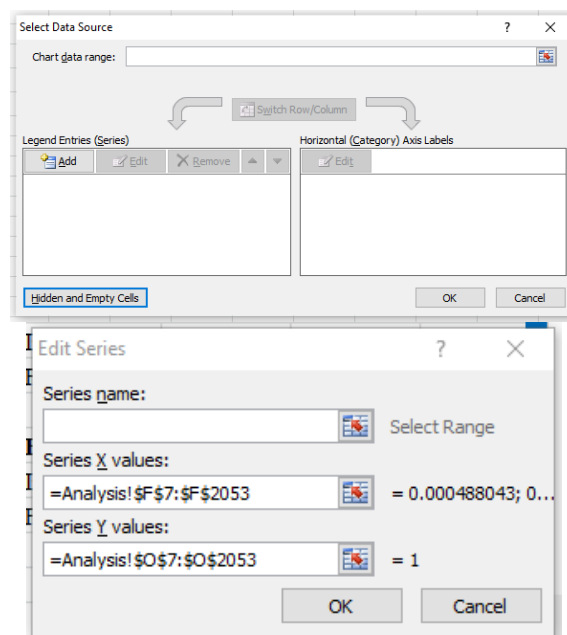


Figure 18. Windows to finish building the graph.

Change the color of the data to a light color, as it is overlaid by the region that is chosen for analysis. To do this, click on the graph with the right mouse button, select Format Data Series → Line Color → Solid Line, and choose a light color, as shown in Fig. 19. Also format the window type, line thickness, axis scale, font, etc., as desired by the user.

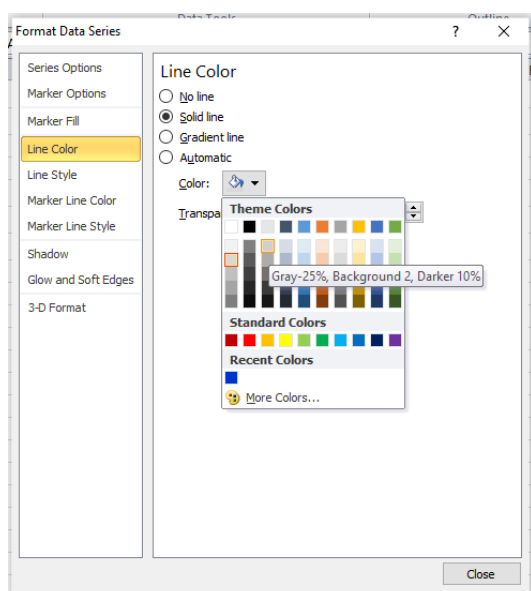


Figure 19. Choosing the color of the data string.

A new data string must be inserted in the graph to overlay the data selected by the scroll bars. To do this, click with the right mouse button on the graph area and select the options: Select Data → Add. Fill the fields “Series X values” and “Series Y values”, as shown in Fig. 20, and click on OK. A new box “Select Data Source” appears; click on OK.

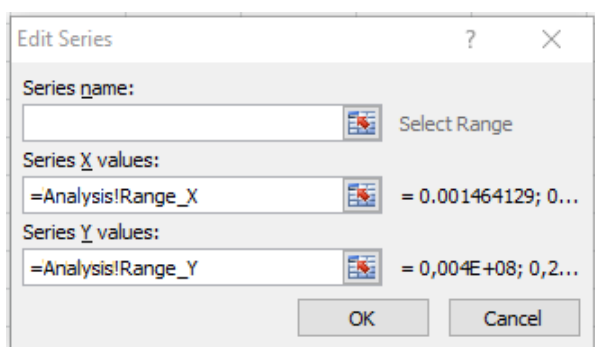


Figure 20. Dialog box to insert the part of the graph where the linear regression is to occur.

Following the procedure shown above, choose a dark color for this second data stream.

For the purposes of this work, it is necessary to add a trendline, which is used to perform the linear fit of the experimental data to a mathematical function (linear regression), using the least squares method. To do this linear regression, click with the right mouse button on the new data sequence (the darkest graph) and choose the option “Add Trendline”. Click on “Power”, as shown in Fig. 21, since the graph axes are on a logarithmic scale and the logarithm properties transform powers into products, so the result is a line. Change the properties “Line Color” and “Line Style”, as desired.

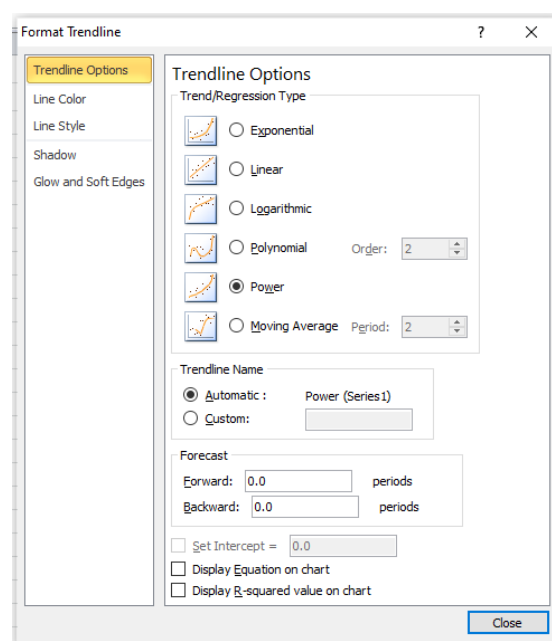


Figure 21. Window to choose and format the trendline.

Position the graph above the slider bars. If highlighting is desired, select the cells behind the graph, color them, and describe the function of the control, in order to facilitate its use. Figure 22 shows an example.

Note that the purpose of the slider bars (placed below the graph) is to delimit the region that will be fitted by the trendline, which can be done by clicking on the arrows (to move 1 point each click), or on the bar itself (to move 10 points for each click). It is also possible to click on the vertical mark and drag.

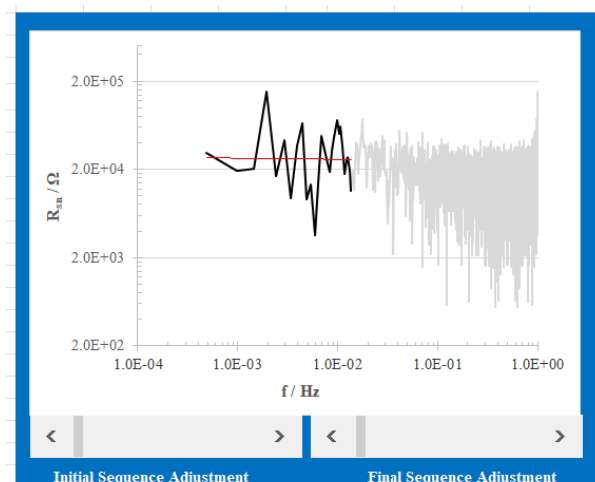


Figure 22. Example image of the graph generated.

The angular and linear coefficients of the fitted line must be inserted in a cell since they are used to calculate R_{sn}^0 . Hence, the cursor is placed in the cell where the slope is to be located (in this example, T8), typing: `=SLOPE(Range_Y_Lin; Range_X_Lin)`. In the cell where the intercept or linear coefficient is to be inserted (in this

example, T9), type: `=INTERCEPT(Range_Y_Lin; Range_X_Lin)`.

In the cell where it is desired to insert the calculation of y using the first value of x (lowest value of the experimental frequency), in this example named $\log(R_{sn}^0)$, type: `=(REF_X_Plot)*T8+T9`, since REF_X_Plot is the cell that indicates the first x value used in the plot, and T8 and T9 are the cells in which the slope and y -intercept values of the trendline were calculated, respectively. If different cells are used, then the same logic should be followed.

Once $\log(R_{sn}^0)$ has been obtained, calculate

R_{sn}^0 by doing $10^{\log(R_{sn}^0)}$ (in this example: `=10^T10`).

To facilitate visualization of the initial and final values of the fitted region, the following formulae can be inserted in cells next to the graph: `=INDEX(F7:F2053; Start_Point + 1)`, for the initial value of the frequency range, and `=INDEX(F7:F2053; End_Point)`, for the end value of the frequency range. Figure 23 illustrates the example being used in this work.

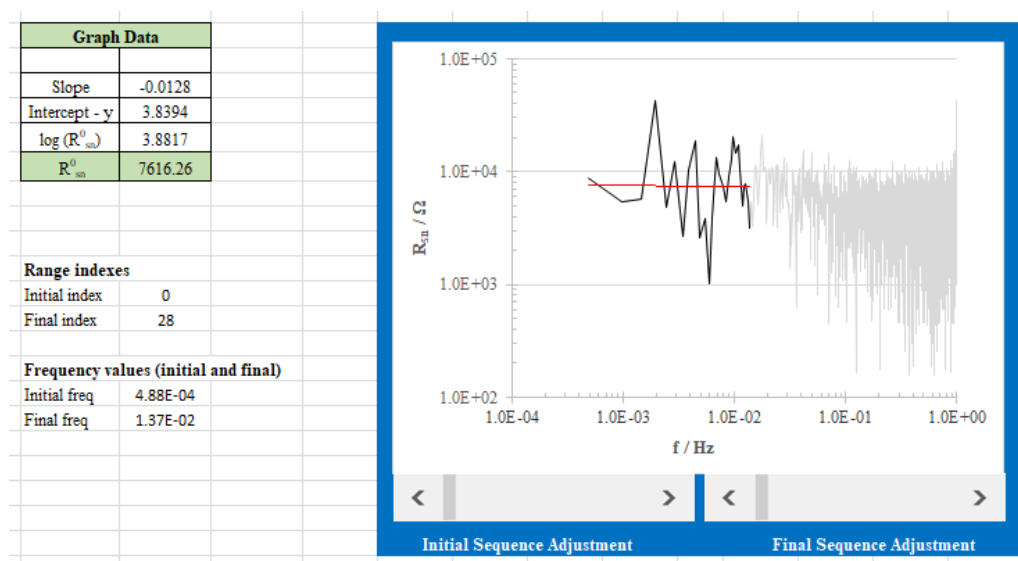


Figure 23. Chart with calculated values of interest.

Once the spreadsheet is built, the goal is to use it to automate the work, performing the analysis of the quantity of data sets it is desired to study, simply by replacing the input data. However, the FFT function does not update automatically with the replacement of the input data. Hence, it is necessary to either manually delete and redo the values calculated by the FFT, every time a new set of input data is used, or implement a macro,

which is an Excel feature for automatically performing programmed tasks. This can be done as follows:

On the ribbon, click Developer → Visual Basic. In the window that appears in the left part of the screen, right-click on Microsoft Excel Objects → Insert → Module, as shown in Fig. 24.

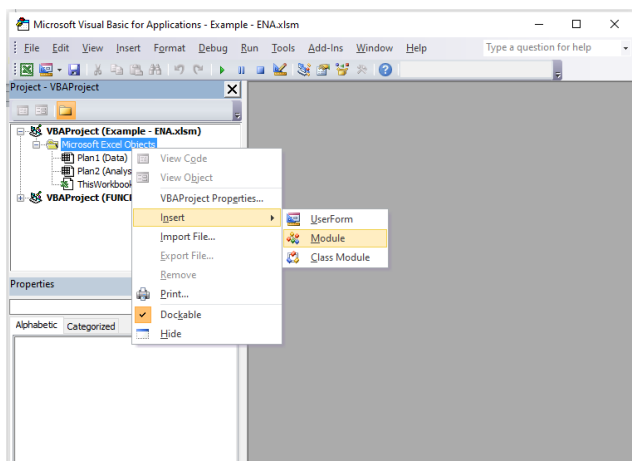


Figure 24. Visual Basic window for creating a macro in Excel.

This creates a workspace. Place the cursor in it and enter the codes described below (note that the cells indicated in the codes refer to the current example). Thus, G6 is the cell where the initial value of FFT_E is positioned, while cells B6 to B2053 contain the range of potential data, E . Analogously, H6 is the cell where the FFT_i values start, while cells D6 to D2053 contain the current data, i . It should be noted that multiplication by the scale factor, mentioned previously, is already included in this macro.

```
Sub Button1 ()
'FFT of Potential
Range("G6").Select
Range(Selection, Selection.End(xlDown)).Select
Selection.ClearContents
Application.Run "Fourier",
ActiveSheet.Range("$B$6:$B$2053"),
ActiveSheet.Range("$G$6"), False, False
'Copy of the current multiplied by the scale factor
Range("$D$6:$D$2053").Copy
Range("$AH$6:$AH$2053").PasteSpecial
xlPasteValues
Range("D2").Copy
Range("$AH$6:$AH$2053").PasteSpecial
xlPasteAll, xlMultiply
'FFT of the current
Range("H6").Select
Range(Selection, Selection.End(xlDown)).Select
Selection.ClearContents
Application.Run "Fourier",
ActiveSheet.Range("$AH$6:$AH$2053"),
ActiveSheet.Range("$H$6"), False, False
'Erases the current multiplied by the scale factor
Range("$AH$6:$AH$2053").Select
```

```
Selection.ClearContents
'Reposition the worksheet focus
Range("$A$1").Select
End Sub
```

Return to the Analysis spreadsheet and choose the location where it is desired to place a button that is to be clicked to update the FFT calculations when a new data set is introduced. In the Developer tab, click on Insert and then click on the image of a button, as shown in Fig. 25.

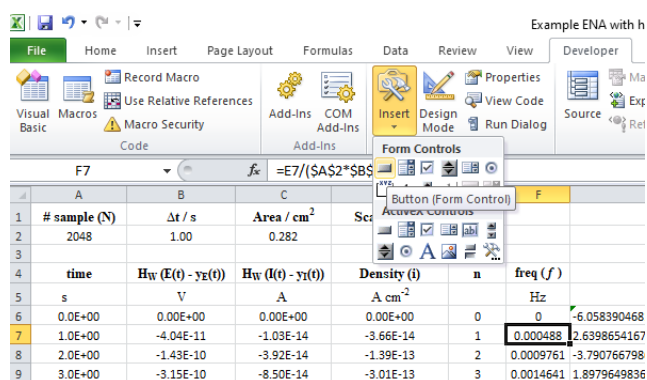


Figure 25. Procedure for insertion of a button in an Excel macro.

Next, click where it is desired to create the button, dragging the cursor to form a rectangle. Release the mouse when the desired size is reached. At this point, a window called Assign Macro opens. Click on Button 1 and then OK (Fig. 26).

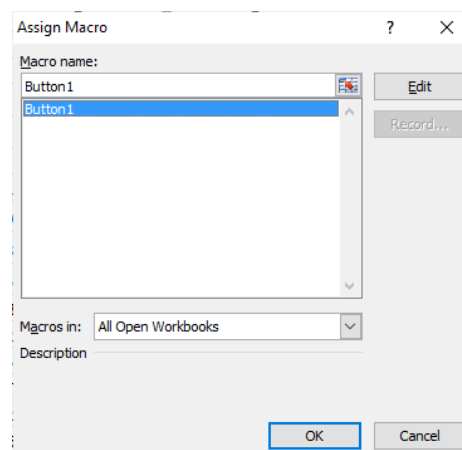


Figure 26. Procedure in Excel for assigning a macro to a button.

In order to change the text on the button, right-click on it, and select Edit Text. To change the font, select the Format option. The result looks like Fig. 27.

#	A	B	C	D	E	F	G	H
1	# sample (N)	$\Delta t / s$	Area / cm^2	Scale Factor				
2	2048	1.00	0.282	1000				
3								
4	time	$H_W(E(t) - y_E(t))$	$H_W(I(t) - y_I(t))$	Density (i)	n	freq (f)	FFT_E	FFT_I
5	s	V	A	A cm^{-2}		Hz		
6	0.0E+00	0.00E+00	0.00E+00	0.00E+00	0	0	-6.05839046814944E-004	2.93378056156407E-005
7	1.0E+00	-4.04E-11	-1.03E-14	-3.66E-14	1	0.000488	2.63986541670193E-003-3.81111834018308E-004i	-2.92324284934354E-004-9.25323676985686E-005i
8	2.0E+00	-1.43E-10	-3.92E-14	-1.39E-13	2	0.0009761	-3.79076679865553E-003+1.10001315796228E-003i	6.2331839349104E-004+3.66734930991556E-004i
9	3.0E+00	-3.15E-10	-8.50E-14	-3.01E-13	3	0.0014641	1.89796498360598E-003-1.3827831045382E-003i	-2.27822331071836E-004-3.43855342316282E-004i
10	4.0E+00	-5.97E-10	-1.45E-13	-5.15E-13	4	0.0019522	-1.61014786377268E-003+1.11852227920365E-003i	-4.0672458279581E-005+2.16639286709312E-005i

Figure 27. Image of a worksheet containing the FFT update button.

Every time the input data is changed, click on the FFT button to remake the FFT_E and FFT_I calculations. All other calculations are automatically updated.

The procedure presented above was also performed without Hann window. The results

obtained with Excel were compared with those obtained with Origin[®] (see the [Supplementary Information 1](#)), a software package widely used by chemists, using the same experimental data and the same linear regression frequency region. The results are presented in [Tab. 1](#).

Table 1. Values of R_{sn}^0 obtained with Excel and Origin[®] routines using the same experimental data for a carbon paste electrode (CPE) modified with chalcopyrite obtained in solution A (T&K) + 0.02 mol L⁻¹ Cu(II)[♦].

Without Hann window				With Hann window			
	Slope	y-intercept	R_{sn}^0 (Ω)		Slope	y-intercept	R_{sn}^0 (Ω)
Excel [®]	0.0716	3.8204	3,830	Excel [®]	-0.0128	3.8394	7,616
Origin [®]	0.0716	3.8204	3,823	Origin [®]	-0.0129	3.8393	7,621

[♦]See [Supplementary material 1](#) and [2](#).

4. Conclusions

The routine developed in Excel, an inexpensive program available to all students and professionals from different areas, was effective for calculation of the spectral electrochemical noise resistance value, R_{sn}^0 , according to the FFT method. It was possible to obtain the values rapidly, saving time when performing repetitive calculations for analysis of the results from a large number of experiments.

Acknowledgments

The author Riberto N. Peres thanks the Brazilian funding CAPES (proc. no. 88882.330063/2019) for a scholarship. The authors also thank Fundunesp (2557/2016) Vale S.A for financial support.

References

[1] Cottis, R. A., Interpretation of electrochemical noise data, *Corrosion* 57 (3) (2001) 265-285. <https://doi.org/10.5006/1.3290350>.

[2] Bertocci, U., Gabrielli, C., Huet, F., Keddari, M., Rousseau, P., Noise resistance applied to corrosion measurements, *Journal of The Electrochemical Society* 144 (1) (1997) 37-43. <https://doi.org/10.1149/1.1837362>.

[3] Mansfeld, F., Su, Z., Hsu, C. H., Electrochemical noise analysis (ENA) for active and passive systems in chloride media, *Electrochimica Acta* 46 (24-25) (2001) 3651-3664. [https://doi.org/10.1016/S0013-4686\(01\)00643-0](https://doi.org/10.1016/S0013-4686(01)00643-0).

[4] Excel for Windows training, 2016.

[5] Mansfeld, F., Lee, C. C., The frequency dependence of the noise resistance for polymer-coated metals, *Journal of The Electrochemical Society* 144 (6) (1997) 2068-2071. <https://doi.org/10.1149/1.1837743>.

[6] Ritter, S., Huet, F., Cottis, R. A., Guideline for an assessment of electrochemical noise measurement devices, *Materials and Corrosion* 63 (4) (2012) 297-302. <https://doi.org/10.1002/maco.201005839>.

[7] Bertocci, U., Huet, F., Nogueira, R. P., Rousseau, P., Drift removal procedures in the analysis of






electrochemical noise, *Corrosion* 58 (4) (2002) 337-347. <https://doi.org/10.5006/1.3287684>.

[8] Homborg, A. M., Tinga, T., Zhang, X., van Westing, E. P. M., Oonincx, P. J., de Wit, J. H. W., Mol, J. M. C., Time-frequency methods for trend removal in electrochemical noise data, *Electrochimica Acta* 70 (2012) 199-209. <https://doi.org/10.1016/j.electacta.2012.03.062>.

[9] Bertocci, U., Frydman, J., Gabrielli, C., Huet, F., Keddam, M., Analysis of Electrochemical Noise by Power Spectral Density Applied to Corrosion Studies: Maximum Entropy Method or Fast Fourier Transform? *Journal of The Electrochemical Society* 145 (8) (1998) 2780-2786. <https://doi.org/10.1149/1.1838714>.

Supplementary information 1

Electrochemical noise analysis to obtain the R_{sn} value via FFT using Excel

Sidinea Barrozo¹, Riberto Nunes Peres², Marcus José Witzler³, Assis Vicente Benedetti², Cecílio Sadao Fugivara²⁺

1. São Paulo State University (Unesp), Institute of Chemistry, Engineering, Physics and Mathematics Department, Araraquara, São Paulo, Brazil

2. São Paulo State University (Unesp), Institute of Chemistry, Department of Analytical Chemistry, Physical Chemistry, and Inorganic, Araraquara, São Paulo, Brazil

3. EMBRAER

*Corresponding author: Cecilio Sadao Fugivara, Phone: +55 16 33019654, Email address: sadao.fugivara@unesp.br

ARTICLE INFO

Article history:

Received: June 02, 2020

Accepted: August 06, 2020

Published: October 01, 2020

Keywords:

1. ENA
2. Excel
3. spectral electrochemical noise resistance
4. detrending
5. Hann window

The **Supplementary Information 1** describes the procedures to calculate R_{sn}^0 using Origin[®] software and to obtain electrochemical noise data, and a file .xlms with the experimental data used to applied the described routine.

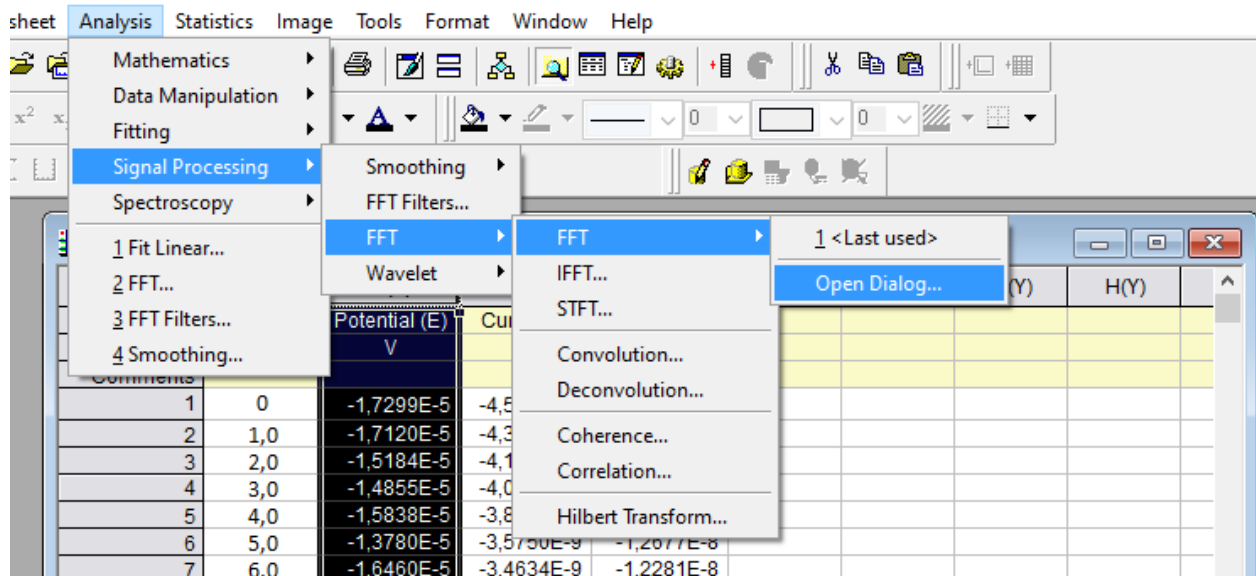
How can ENA data be analyzed using Origin[®] software?

To make the same analysis, described in the main text, using Origin[®] software follows the steps below:

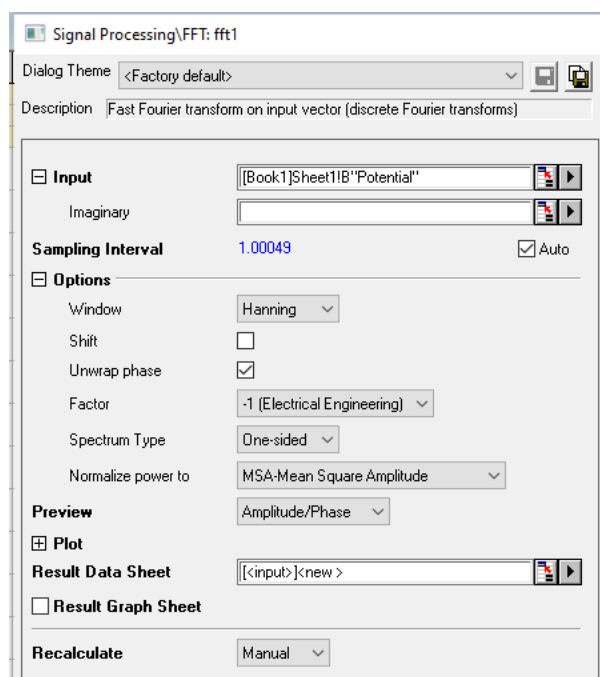
Copy the data of time (t), potential ($E(t) - y_E(t)$) and current ($I(t) - y_I(t)$) in the first three

columns (A, B and C). Divide the current values by the electrode area and put the results in column D (select the column D and follows the commands: Column → Set Columns Values → in the box, type Col(C)/area value → Ok).

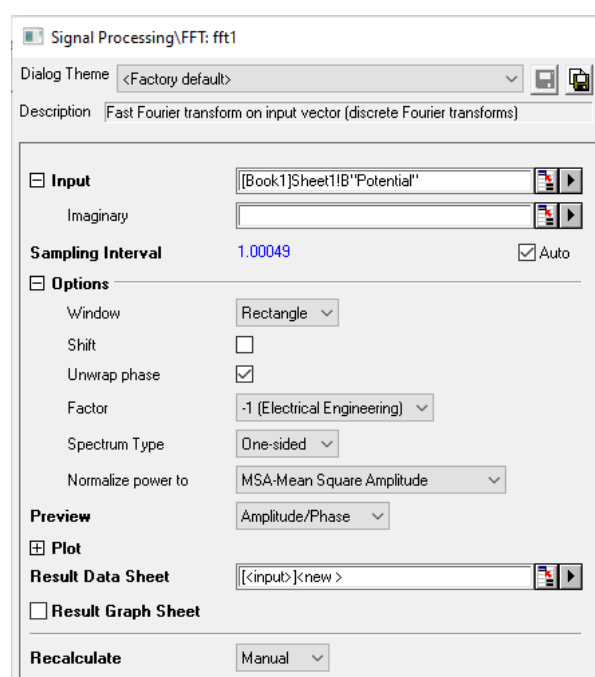
Select the potential column and follows the commands: Analysis → Signal Processing → FFT → FFT → Open Dialog (**Fig. S1a**). In the window that appears, choose the option Window Hanning → uncheck Shift → in Spectrum Type box, choose One-sided → uncheck Result Graph Sheet → Ok (**Fig. S1b**). If you do not use the Hann window, mark Window Rectangle, as in **Fig. S1c**:



a)



b)



c)

Figure S1. FFT Origin® command with (B) and without (C) Hann window.

A new tab is created (FFTResultData1) that has all necessary information to potential analysis, including frequency and PSD_E , which is in

column of “Power as MSA”. Repeat the proceeding for the column of the current. The Fig. S2 shows the tab FFTResultData1.

Long Name	Frequency	Complex	Real	Imaginary	Magnitude	Amplitude	Phase	Power as MSA	dB
1	0	-9.86848E-4	-9.86848E-4	0	9.86848E-4	4.8186E-7	180	2.32189E-13	-126.34159
2	4.88043E-4	0.00431 - 6.17038E-4i	0.00431	-6.17038E-4	0.00436	4.25509E-6	351.85882	9.05291E-12	-107.42182
3	9.76086E-4	-0.0062 + 0.0018i	-0.0062	0.0018	0.00645	6.30026E-6	523.80493	1.98466E-11	-104.01283
4	0.00146	0.0031 - 0.00226i	0.0031	-0.00226	0.00384	3.74519E-6	683.86978	7.01322E-12	-108.53052
5	0.00195	-0.00263 + 0.00183i	-0.00263	0.00183	0.0032	3.12707E-6	505.23902	4.88928E-12	-110.09725
6	0.00244	9.8727E-4 + 5.12694E-4i	9.8727E-4	5.12694E-4	0.00111	1.08638E-6	387.44305	5.90114E-13	-119.28034
7	0.00293	0.00124 - 0.00188i	0.00124	-0.00188	0.00225	2.19987E-6	303.48338	2.41971E-12	-113.15207
8	0.00342	5.61276E-4 - 2.89181E-5i	5.61276E-4	-2.89181E-5	5.6202E-4	5.48848E-7	357.05061	1.50617E-13	-125.21096
9	0.0039	-8.04048E-4 - 9.3031E-4i	-8.04048E-4	-9.3031E-4	0.00123	1.2008E-6	229.16381	7.20963E-13	-118.41057

Figure S2. Results of the FFT routine applied to Potential data using Origin®.

Copy the column “Power as MSA” of the tab FFTResultData1 (PSD_E) and paste it in column E of the Sheet1 and repeat the proceeding for Current density (i), pasting the PSD_I in column F of the Sheet1.

Select the column G in the Sheet1 and follow the commands: Column → Set Columns Values → in the box, type Sqrt(Col(E)/Col(F)) → Ok, to calculate R_{sn} . Figure S3 shows this proceeding.

Copy the frequency column (Freq(X)) of the tab FFTResultData1 and paste it in column H of the Sheet1. In the column I calculate $\log f^{10}$ making: select the column I → Column → Set Columns Values → in the box, type log(Col(H)) → Ok. Use the same proceeding to calculate $\log(R_{sn}^{10})$ in the column J. Your folder Sheet1 should look like Fig. S4.

Set Values - [Book1]Sheet1!Col(G)

Formula wcol(1) Col(A) F(x)

Row (i): From Auto To Auto

Col(G) =

Sqrt(Col(E)/Col(F))

Recalculate None Apply Cancel OK

Figure S3. Command to calculate $\sqrt{\frac{PSD_E}{PSD_I}}$

Long Name	Time (t)	Potential (E)	Current (I)	density (i)	Power as MSA	Rsn	Frequency	log(freq)	log(Rsn)	
Units	s	V	A	A cm ²	PSDE	PSDi				
1	0	-1.7299E-5	-4.5357E-9	-1.6084E-8	2,3219E-13	5,4470E-22	2,0646E4	0	--	4,3148E0
2	1,0	-1,7120E-5	-4,3817E-9	-1,5538E-8	9,0529E-12	1,1946E-19	8,7052E3	4,8804E-4	-3,3115E0	3,9398E0
3	2,0	-1,5184E-5	-4,1596E-9	-1,4750E-8	1,9847E-11	6,6572E-19	5,4601E3	9,7609E-4	-3,0105E0	3,7372E0
4	3,0	-1,4855E-5	-4,0066E-9	-1,4208E-8	7,0132E-12	2,1610E-19	5,6968E3	1,4641E-3	-2,8344E0	3,7556E0
5	4,0	-1,5838E-5	-3,8534E-9	-1,3664E-8	4,8893E-12	2,7131E-21	4,2451E4	1,9522E-3	-2,7095E0	4,6279E0
6	5,0	-1,3780E-5	-3,5750E-9	-1,2677E-8	5,9011E-13	2,6159E-20	4,7496E3	2,4402E-3	-2,6126E0	3,6767E0
7	6,0	-1,6460E-5	-3,4634E-9	-1,2281E-8	2,4197E-12	1,6253E-20	1,2202E4	2,9283E-3	-2,5334E0	4,0864E0
8	7,0	-1,6486E-5	-3,3493E-9	-1,1877E-8	1,5062E-13	2,1267E-20	2,6612E3	3,4163E-3	-2,4664E0	3,4251E0
9	8,0	-1,4873E-5	-3,2256E-9	-1,1438E-8	7,2096E-13	6,7114E-21	1,0365E4	3,9043E-3	-2,4085E0	4,0156E0

Figure S4. Table of sheet1 with necessary values to calculate R_{sn}^0 .

To make the graph select the column I → Column → Set as \underline{X} ; select the column J → Column → Set as \underline{Y} . How the study is made in low frequency, select only the values of interesting to make the fit. In this case, the interval between row 2 and 29 was chosen to compare with Excel results (using Hann window). Make the graph using the commands: Plot → Line → Line (see Fig. S5).

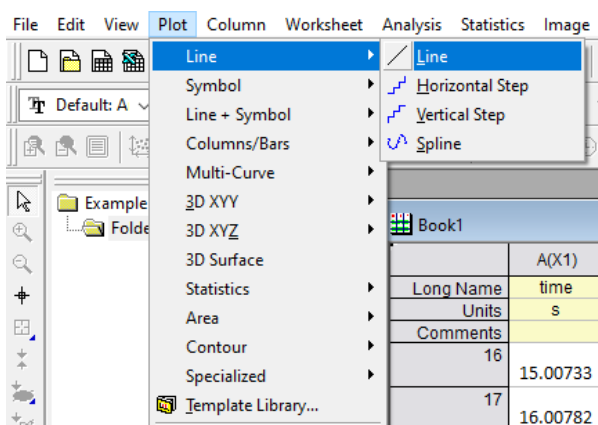


Figure S5. Commands to make a graph using line.

Fit the straight line to graph (linear regression) by commands: Analysis → Fitting → Linear Fit → Ok. A new tab will be open, and the values of slope and intercept are presented in Parameters, like in the Fig. S6. Use these parameters to calculate R_{sn}^0 , as described in the paper.

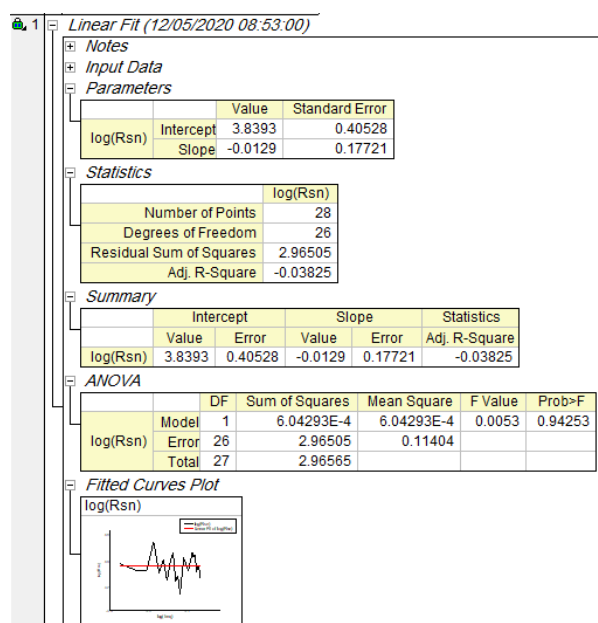


Figure S6. Results of the linear regression.

Obtention of electrochemical noise data

Current and potential noise data were obtained in a Potentiostat / Galvanostat Reference 600 using the ESA410 software, from GAMRY Instruments®. The data contained in the spreadsheets were treated with the Excel software and compared with the treatment made with the Origin® software, with and without the Hann window option.

Electrochemical noise measurements were carried out using carbon paste electrodes modified with chalcopirite powder. The powdered chalcopirite ($\phi_{\text{average}} = 38 \mu\text{m}$) stored in argon atmosphere was mixed with graphite powder (Alfa Aesar, $\phi_{\text{average}} = 42 \mu\text{m}$) in the proportion of 50 wt.% plus a drop of binder (mineral oil) and 0.6 mL of chloroform, according to the literature¹. The resulting paste was placed on a cavity electrode, constituting the carbon paste electrode (CPE), expounding an area of 0.282 cm^2 to the solution.

The solution A of the T&K medium² containing 0.5 g L^{-1} of each of Mg^{2+} and NH_4^+ sulfate and potassium phosphate salts, 0.08 mol L^{-1} ionic strength, pH 1.8 (adjusted with diluted H_2SO_4) plus 0.020 mol L^{-1} CuSO_4 was used as electrolyte.

The electrochemical cell (Fig. S7) consisted of a glass cylinder placed horizontally, having two similar CPE electrodes fixed to the opposite sides of the cylinder and a reference electrode of $\text{Ag/AgCl/KCl} 3 \text{ mol L}^{-1}$ in a Lugging capillary positioned close to one of the CPE electrodes. Once the electrochemical cell was connected to the potentiostat, all current and potential filters were activated for automatic scaling. The electrochemical cell was switched on and the potential and current noise were expected to stabilize before starting to record the 2048 points at the frequencies of 1 Hz. The experiments last 34 min and 8 s (1 Hz). Experimental data are in Excel in Supplementary information 2.

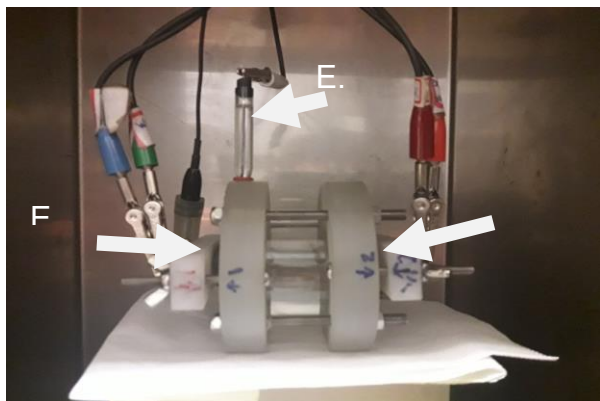


Figure S7. Electrochemical cell for obtaining the ENA data.

References

- [1] Horta, D. G., Bevilaqua, D., Acciari, H. A., Garcia Júnior, O., Benedetti, A. V., Optimization of the use of carbon paste electrodes (CPE) for electrochemical study of the chalcopyrite, *Química Nova* 32 (7) (2009) 1734-1738. <https://doi.org/10.1590/S0100-40422009000700010>.
- [2] Tuovinen, O. H., Kelly, D. P., 1973. Studies on the growth of *Thiobacillus ferrooxidans*, *Archiv für Mikrobiologie* 88 (4) (1973) 285-298. <https://doi.org/10.1007/BF00409941>.